TU Delft

Delft University of Technology

Document Version
Final published version

Citation (APA)
Mahadevan, G. (2026). *Liquid Metal Embrittlement of Automotive Steels: Characterizing failure mechanisms during Resistance Spot Welding*. [Dissertation (TU Delft), Delft University of Technology].
https://doi.org/10.4233/uuid:ef5d2ed5-424f-407a-97f2-803f2a919368

Important note
To cite this publication, please use the final published version (if applicable).
Please check the document version above.

Copyright
In case the licence states “Dutch Copyright Act (Article 25fa)”, this publication was made available Green Open Access via the TU Delft Institutional Repository pursuant to Dutch Copyright Act (Article 25fa, the Taverne amendment). This provision does not affect copyright ownership.
Unless copyright is transferred by contract or statute, it remains with the copyright holder.

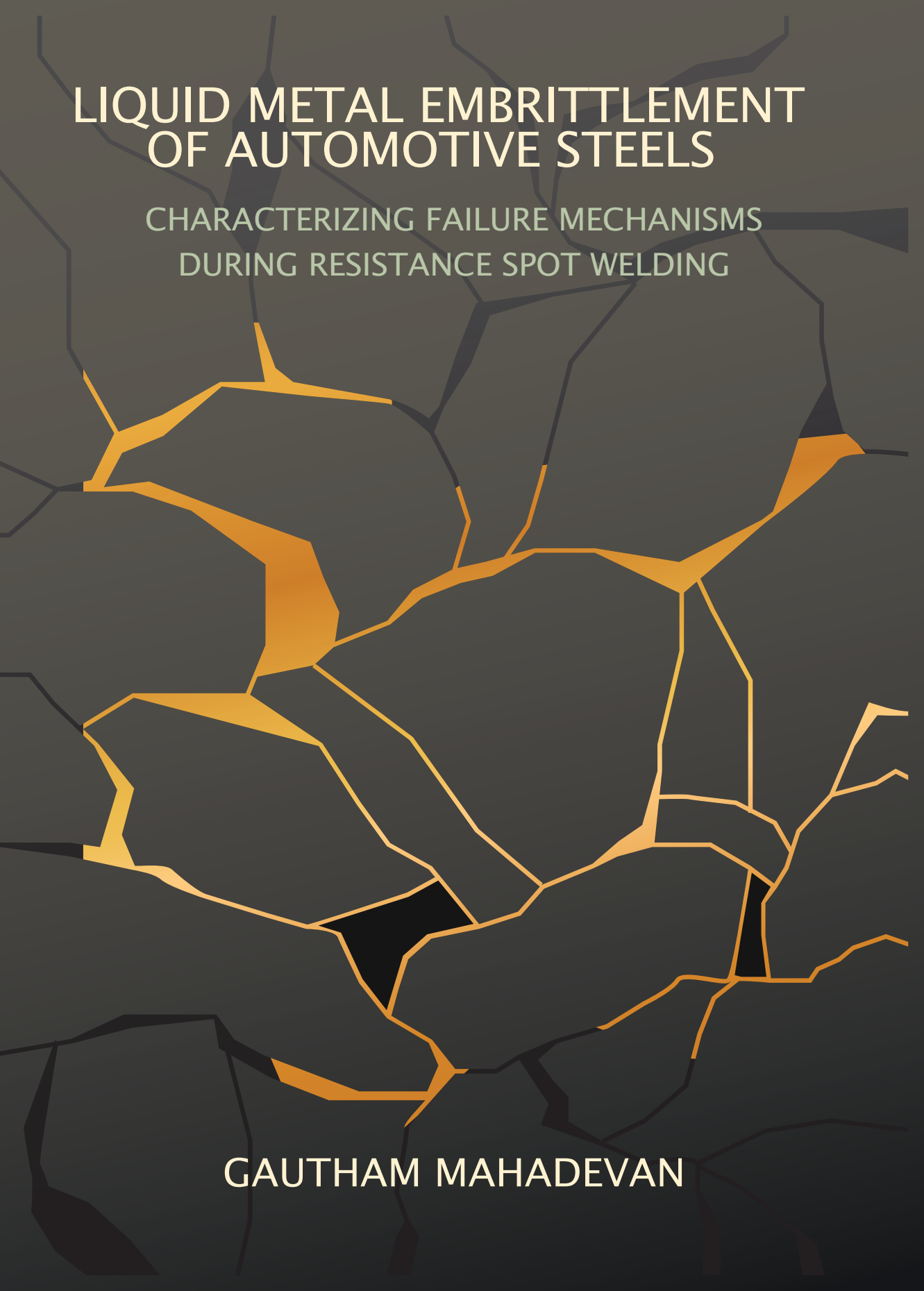
Sharing and reuse
Other than for strictly personal use, it is not permitted to download, forward or distribute the text or part of it, without the consent of the author(s) and/or copyright holder(s), unless the work is under an open content license such as Creative Commons.

Takedown policy
Please contact us and provide details if you believe this document breaches copyrights.
We will remove access to the work immediately and investigate your claim.

This work is downloaded from Delft University of Technology.

LIQUID METAL EMBRITTLEMENT OF AUTOMOTIVE STEELS

CHARACTERIZING FAILURE MECHANISMS DURING RESISTANCE SPOT WELDING



GAUTHAM MAHADEVAN

Liquid Metal Embrittlement of Automotive Steels

Characterizing failure mechanisms during Resistance Spot Welding

Liquid Metal Embrittlement of Automotive Steels

Characterizing failure mechanisms during Resistance Spot Welding

Dissertation

for the purpose of obtaining the degree of doctor
at Delft University of Technology
by the authority of the Rector Magnificus, prof. dr. ir. H. Bijl,
chair of the Board for Doctorates
to be defended publicly on
Thursday 22 October 2026 at 12:30 p.m

by

Gautham MAHADEVAN

This dissertation has been approved by the promotors.

Composition of the doctoral committee:

Rector Magnificus,	chairperson
Dr. ir. M.J.M. Hermans,	Delft University of Technology, *promotor*
Prof. dr. ir. L.A.I. Kestens,	Delft University of Technology/Ghent University, *promotor*

Independent members:

Univ. Prof. Dr. -Ing M. Rethmeier	Technische Universitat Berlin
Dr. ir. E.M. van der Aa	Tata Steel Europe
Prof. dr. A.A. Zadpoor	Delft University of Technology
Dr. ir. S.E. Offerman	Delft University of Technology
Prof. dr. V.A. Popovich	Delft University of Technology

This publication is part of the project N19010 in the Partnership Program of the Materials Innovation Institute M2i framework, which is partly financed by the Dutch Research Council (NWO) and the partners Tata Steel and AutomotiveNL

Keywords: TWIP steels, liquid metal embrittlement, microstructure characterization, Zn diffusion, FEA

Printed by: Ridderprint

Cover by: Ambika G. A Schematic representation of liquid metal embrittlement of zinc in a steel microstructure.

Copyright © 2026 by G. Mahadevan

ISBN 978-94-6518-457-9

An electronic copy of this dissertation is available at https://repository.tudelft.nl.

எப்பொருள் யார்யார்வாய்க் கேட்பினும் அப்பொருள்
மெய்ப்பொருள் காண்ப தறிவு

The mark of true wisdom is to discern the truth from whatever source it is heard.

– திருக்குறள் / Thirukural

Contents

Summary xi

Samenvatting xiii

1 Introduction 1
1.1 Steels for automotive manufacturing . . . 1
1.2 RSW of Zn coated steel . . . 2
1.3 LME - a critical challenge . . . 3
1.4 Knowledge gaps . . . 4
1.5 Research aims and scope . . . 5
1.6 Scientific approach . . . 6
1.7 Thesis outline . . . 6
References . . . 7

2 Literature review 11
2.1 Introduction . . . 11
2.2 Zn coating of AHSS . . . 13
2.3 Resistance Spot Welding . . . 14
2.4 Liquid Metal Embrittlement (LME) . . . 15
2.4.1 LME mechanisms . . . 16
2.5 Effect of steel microstructure on LME . . . 20
2.6 Effect of temperature on LME . . . 24
2.7 Effect of Stress on LME . . . 25
2.8 Effect of welding on LME . . . 26
2.8.1 Location of LME cracks in RSW . . . 27
2.8.2 Effect of welding process parameters on LME . . . 27
2.9 Modelling of LME . . . 30
2.9.1 Atomic scale modelling . . . 30
2.10 Research gaps and Conclusion . . . 32
References . . . 33

3 Materials and Methods 41
3.1 Introduction . . . 41
3.2 Materials . . . 41
3.2.1 Welding Setup . . . 42
3.3 Characterization . . . 43
3.3.1 Optical Microscopy . . . 43
3.3.2 Scanning Electron Microscopy . . . 44
3.3.3 X-Ray Diffraction . . . 45

3.3.4 Scanning Tunnelling Electron Microscopy . . . 45
3.4 Finite Element Analysis . . . 47
3.4.1 Input variables . . . 47
3.4.2 Model outputs . . . 48

4 LME crack initiation 49
4.1 Introduction . . . 49
4.2 Materials and methods . . . 51
4.3 Results . . . 51
4.3.1 Microstructure characterisation of LME cracks . . . 51
4.3.2 Fe-Zn interface characterization . . . 51
4.3.3 Comparing FEA and experimental observations . . . 59
4.4 Discussion . . . 63
4.5 Conclusions . . . 65
References . . . 65

5 Effect of steel microstructure on LME crack path 71
5.1 Introduction . . . 71
5.2 Materials and Methods . . . 73
5.3 Results . . . 73
5.3.1 Microstructure characterization of LME cracks . . . 73
5.3.2 Analysis framework . . . 74
5.3.3 GB misorientation and loading axis orientation . . . 77
5.4 Discussion . . . 83
5.4.1 Effect of GB type on LME crack path . . . 84
5.4.2 Misorientation angle vs Stress Normalisation factor . . . 86
5.4.3 Proposed framework for LME GB susceptibility index . . . 87
5.4.4 GB engineering for LME mitigation . . . 88
5.5 Conclusions . . . 88
References . . . 89

6 Quantifying Zinc Diffusion Ahead of LME Cracks 93
6.1 Introduction . . . 93
6.2 Materials and methods . . . 95
6.2.1 Characterization . . . 95
6.2.2 Numerical modelling framework . . . 96
6.2.3 Effect of stress . . . 99
6.3 Results . . . 99
6.3.1 EDS Analysis . . . 101
6.3.2 Comparison of EDS measurements with diffusion simulations . . . 102
6.4 Discussion . . . 107
6.4.1 Comparison between EDS and diffusion modelling . . . 107
6.4.2 Bulk and GB diffusion of Zn . . . 108
6.5 Conclusions . . . 110
References . . . 111

7 Effect of RSW hold time on LME **115**
7.1 Introduction . . . 115
7.2 Materials and Methods . . . 117
7.3 Results . . . 117
7.3.1 Optical microscopy of RSW cross-sections . . . 117
7.3.2 Comparing hold times . . . 123
7.3.3 FEA of RSW . . . 124
7.3.4 Temperature evolution in electrode region . . . 127
7.3.5 Temperature evolution in weld shoulder region . . . 128
7.3.6 Temperature evolution in weld periphery region . . . 129
7.4 Discussion . . . 130
7.4.1 Electrode region . . . 130
7.4.2 Weld shoulder region . . . 131
7.4.3 Weld periphery region . . . 131
7.5 Conclusions . . . 132
References . . . 133

8 General discussion, limitations and recommendations **135**
8.1 General discussion . . . 135
8.1.1 Evolution of LME in RSW . . . 135
8.2 Limitations . . . 137
8.3 Future work and recommendations . . . 138
References . . . 139

Acknowledgements **141**

Curriculum Vitæ **143**

List of Publications **145**

Summary

Advanced high-strength steels (AHSS), including twinning-induced plasticity (TWIP) steel, are widely used in the automotive industry to reduce weight and improve crash safety. However, resistance spot welding (RSW) of galvanised AHSS often leads to liquid metal embrittlement (LME) - a failure mechanism caused by liquid zinc penetrating grain boundaries at elevated temperatures. This thesis investigates LME during RSW of galvanised TWIP steel using a combined experimental and modelling approach. A heterogeneous triple-stack weld geometry (TWIP over two DX54 sheets) was used to promote LME crack formation. Samples were welded across eight weld times (300 ms to 1700 ms) and eight hold times (5 ms to 355 ms), and characterised using scanning electron microscopy with energy-dispersive spectroscopy (SEM-EDS), electron backscatter diffraction (EBSD), X-ray diffraction (XRD), and scanning transmission electron microscopy (STEM-EDS). Finite element analysis (SORPAS) provided temperature and stress distributions during welding. This thesis takes a deeper look into all parts of the LME crack and the RSW process to study their effect on embrittlement. First, crack initiation is investigated: the results show that Fe-Zn intermetallic phases form continuously at weld shoulder temperatures and suppress LME by preventing direct liquid zinc contact with grain boundaries. As weld time increases, these phases become thermodynamically unstable and break down, allowing liquid zinc to penetrate austenitic grain boundaries. Crack propagation is then studied through the effects of grain boundary misorientation and stress on the LME crack path as well as the effect of zinc diffusion at the crack tip with changing welding parameters. Finally, the effect of another RSW parameter, the hold time, on LME and crack formation is studied across the different regions of the weld cross-section.

Samenvatting

Advanced high-strength steels (AHSS), waaronder twinning-induced plasticity (TWIP) steel, worden veel gebruikt in de auto-industrie om gewicht te verminderen en de botsveiligheid te verbeteren. Het resistance spot welding (RSW) van gegalvaniseerd AHSS leidt echter vaak tot liquid metal embrittlement (LME) – een faalmechanisme dat wordt veroorzaakt doordat liquid zinc bij verhoogde temperaturen in de grain boundaries dringt. Dit proefschrift onderzoekt LME tijdens het RSW van gegalvaniseerd TWIP steel met behulp van een gecombineerde experimentele en modelleringsaanpak. Een heterogene triple-stack lasconfiguratie (TWIP op twee DX54-platen) werd gebruikt om de vorming van LME-scheuren te bevorderen. De monsters werden gelast over acht weld times (300 ms tot 1700 ms) en acht hold times (5 ms tot 355 ms), en gekarakteriseerd met behulp van scanning electron microscopy with energy-dispersive spectroscopy (SEM-EDS), electron backscatter diffraction (EBSD), X-ray diffraction (XRD) en scanning transmission electron microscopy (STEM-EDS). Finite element analysis (SORPAS) leverde de temperatuur- en spanningsverdelingen tijdens het lassen. De resultaten tonen aan dat Fe-Zn intermetallic phases zich continu vormen bij de temperaturen van de weld shoulder en LME onderdrukken door direct contact tussen liquid zinc en de grain boundaries te voorkomen. Naarmate de weld time toeneemt, worden deze fasen thermodynamisch instabiel en breken ze af, waardoor liquid zinc in de austenitische grain boundaries kan dringen. De diffusie van zink langs de grain boundaries is ongeveer 30 keer groter dan de bulk diffusion en neemt toe met de weld time. Ten slotte onderdrukt de hold time LME in het electrode-gebied effectief doordat de water-cooled electrodes het verplaatste liquid zinc laten stollen voordat ze loskomen. Deze bevindingen bieden een dieper inzicht in de mechanismen die LME beheersen en bevelen strategieën aan voor procesbeheersing en grain boundary engineering om scheurvorming tijdens het lassen te beperken.

1 Introduction

1.1. Steels for automotive manufacturing

The global automotive industry faces a key challenge: reducing vehicle weight to lower fuel consumption and emissions while maintaining safety and performance. Since steel makes up about 60-70% of a modern vehicle's weight, its properties play a major role in meeting these goals. Conventional low-strength steels are easy to form but need thicker sheets to achieve the required stiffness and crash resistance, which increases weight. This trade-off has driven ongoing development of new alloys that offer higher strength without losing ductility [1, 2]. Advanced High-Strength Steels (AHSS) are a key solution to this challenge. They use microstructural mechanisms such as transformation-induced plasticity, dual-phase strengthening, and martensitic hardening to achieve yield strengths above 300 MPa and tensile strengths over 600 MPa, while still allowing sufficient elongation for forming. Compared to conventional steels, AHSS makes it possible to use thinner sheets without reducing crash performance, leading to lower fuel consumption and reduced lifecycle emissions [2, 3]. Twinning-Induced Plasticity (TWIP) steel is an example of second-generation AHSS. With a relatively high manganese composition (15-30 wt.%), they maintain a fully austenitic structure at room temperature. During deformation, their low stacking fault energy promotes mechanical twinning instead of dislocation slip or martensitic transformation. As twins form, they progressively divide the grains into finer structures, limiting dislocation movement and maintaining a high work-hardening rate. This results in a unique combination of high strength (typically 800-1000 MPa) and elongation (over 50-60%), making TWIP steels especially suitable for energy-absorbing components such as B-pillars, side-impact beams, and crash boxes in automobiles [4, 5]. An overview of the spot welding process during automotive manufacturing is shown in Figure 1.1

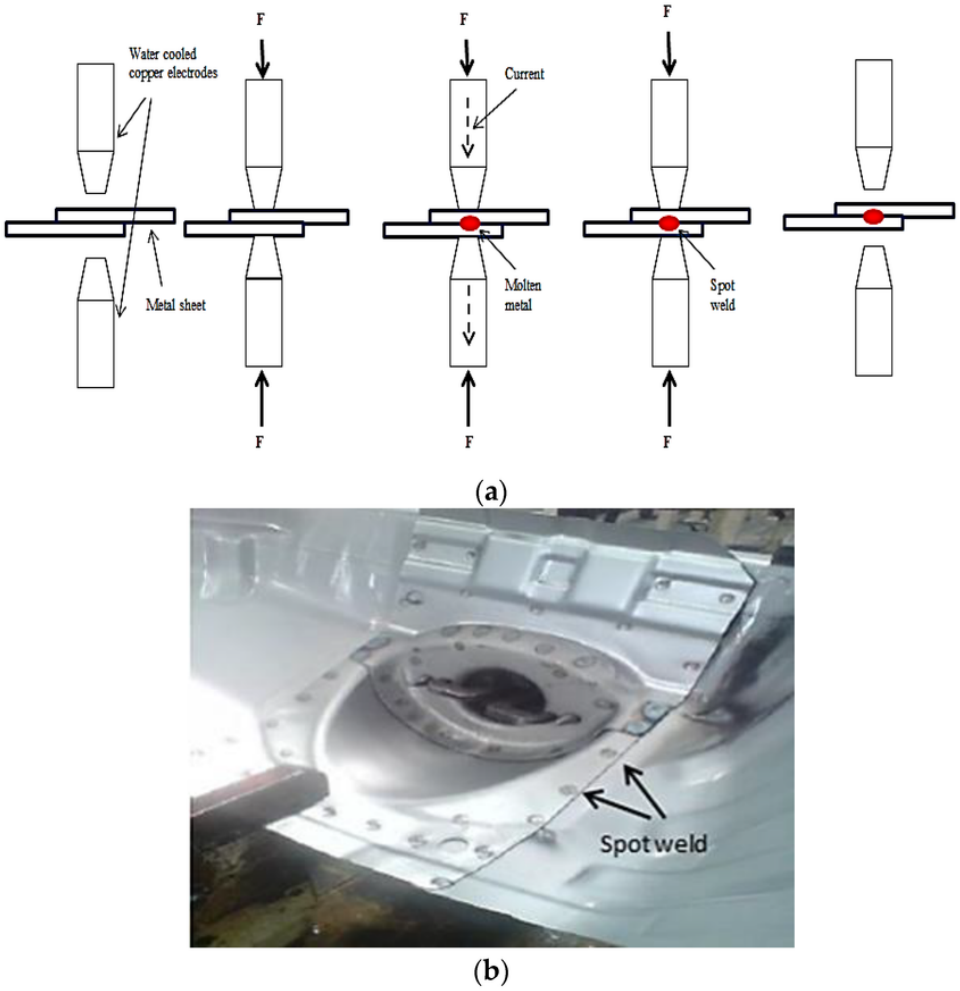


Figure 1.1: Resistance Spot Welding process of automotive steels showing (a) Schematic of RSW process (b) RSW during automotive manufacturing [6]

1.2. RSW OF ZN COATED STEEL

Using TWIP steel in automotive body-in-white structures requires a corrosion-protection coating and a joining method suitable for thin sheets and high production rates. Corrosion protection is achieved using a Zn coating applied by hot-dip galvanising, where the steel is immersed in molten Zn. A small aluminium addition (0.1-0.2 wt.%) is typically used to control reactions at the interface and improve coating adhesion [7]. The Zn layer provides sacrificial protection by corroding instead of the underlying steel over the vehicle's lifetime [7, 8]. During galvanising, interaction between molten Zn

and iron leads to the formation of Fe-Zn intermetallic phases (Γ, Γ_1, δ, and ζ) at the interface [8–10]. Their morphology, thickness, and stability depend on temperature and local composition. The behaviour of these intermetallic phases during later processing, especially welding, is central to this work.

Resistance spot welding (RSW) is the primary joining method in automotive manufacturing, with each vehicle containing 3000 to 5000 spot welds. In this process, overlapping steel sheets are clamped between water-cooled copper electrodes, and a current is applied for a period of time. This generates heat at the interface, causing local melting and forming a weld nugget that solidifies under pressure [11]. RSW is controlled by process parameters like welding current, welding force, weld time and hold time. The welding current determines how much electrical energy is supplied, and therefore how much heat is generated at the interface. Weld time is the duration for which this current is applied, controlling how long heating and melting occur. Electrode force is the pressure applied by the electrodes to hold the sheets together, which affects electrical contact, heat generation, and the shape of the weld nugget. Hold time is the period for which this force is maintained after the current stops, allowing the molten region to solidify under pressure and helping to reduce defects [11–13]. The temperature at the weld centre exceeds 1400 °C, dropping to near room temperature within 2-4 mm from the fusion zone, which leads to temperature gradients across the weld. During cooling, the solidified nugget is restrained by the surrounding colder material and the clamping electrodes, which prevents free contraction and leads to the development of high residual tensile and compressive stresses in different regions of the weld [11, 13].

1.3. LME - A CRITICAL CHALLENGE

The combination of Zn availability, high temperature, and mechanical stress during RSW creates conditions for a failure mode known as liquid metal embrittlement (LME). LME is the sudden loss of ductility that occurs when a solid metal is in contact with a liquid metal under an applied stress above a certain threshold. In automotive welding, it appears as intergranular cracks in the heat-affected zone (HAZ) of Zn-coated AHSS spot welds. Molten Zn penetrates susceptible grain boundaries, leading to intergranular decohesion and crack formation. These cracks can grow hundreds of micrometres into the steel, reducing mechanical strength, fatigue resistance, and overall joint reliability [14–17]. A schematic representation of the LME process is shown in Figure 1.2.

LME has been known and studied for decades, but it has become a renewed concern in automotive welding with the introduction of AHSS, particularly TWIP steels. TWIP steels are fully austenitic and are prone to Zn-induced LME [18–21]. This increased susceptibility is linked to the high grain boundary (GB) energy and excess free volume of random high-angle grain boundaries (HAGBs) in recrystallised austenite. These features make it easier to satisfy the thermodynamic condition for grain boundary wetting ($\gamma_{GB} \geq 2\gamma_{SL}$), where γ_{GB} is the GB energy and γ_{SL} is the solid-liquid interfacial energy [22, 23]. In addition, the microstructure contains a high fraction of such boundaries, further increasing the number of potential penetration paths. The micromechanism by which Zn penetrates GBs and causes intergranular cracking in the Fe-Zn system is linked to stress-assisted GB diffusion and called the Rehbinder effect [23–25]. According

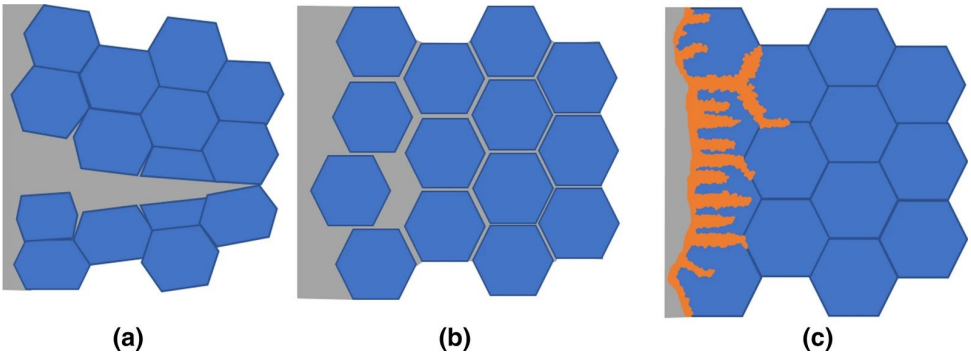


Figure 1.2: Schematic representation of the LME process to show (a) interfacial cracking assisted by liquid metal, (b) decohesion of grain boundary and (c) embrittlement of liquid metal in solid matrix [15]

to this theory, liquid Zn infiltrates grain boundaries, lowers the interfacial energy of the steel surface, and promotes decohesion once a critical tensile stress is reached. However, no single mechanism is universally accepted. Proposed models include ductile fracture mechanisms based on dislocation pile-ups, brittle fracture models involving chemisorption-induced weakening of atomic bonds, and grain boundary diffusion models describing stress-assisted transport of the liquid metal [14, 26–28].

The challenge is further complicated by the strong dependence of LME on temperature, stress, strain rate, and microstructure, as well as the rapidly changing thermo-mechanical conditions present during RSW. Since the governing micromechanisms are not yet fully resolved, further experimental and modelling work is required to better understand crack initiation and growth and to develop reliable mitigation strategies.

1.4. Knowledge Gaps

Despite extensive research on LME in Zn-coated AHSS, several fundamental questions remain unresolved, limiting the ability to predict, model, and mitigate LME in RSW.

Firstly, the evolution of the Fe-Zn interface microstructure during RSW - in particular the formation, transformation, and breakdown of intermetallic (IM) phases has not been systematically characterised as a function of welding parameters. While Fe-Zn intermetallic behaviour during galvanising is well described using equilibrium phase diagrams, RSW involves dynamic, non-equilibrium temperature and stress conditions that lead to a different sequence of interfacial reactions. The relationship between IM phase stability, the presence of liquid Zn, and the onset of LME cracking is still largely qualitative.

Second, although stress-assisted GB diffusion of Zn is widely accepted as the governing mechanism in the Fe-Zn system, there is still no direct experimental quantification of Zn diffusion ahead of crack tips under realistic welding conditions. Most studies rely on high-resolution microscopy at isolated locations, which cannot capture how diffusion distance varies with weld time or crystallographic orientation. As a result,

the relationship between welding parameters, temperature history, and Zn diffusion has not been established. In addition, the relative roles of GB versus bulk diffusion during welding remain unclear, meaning that current theoretical models of LME lack experimental validation.

Third, although it is established that LME cracks propagate intergranularly along HAGBs, the quantitative effects of grain boundary misorientation and boundary orientation relative to the loading axis on the LME crack path have not been studied under actual RSW conditions. Most existing studies rely on simplified mechanical tests, limited datasets of GBs, or a narrow range of welding parameters. As a result, it remains unclear how the competition between boundary susceptibility and mechanical alignment evolves with increasing weld heat input. No predictive model currently exists that combines these factors to describe LME crack path selection.

Finally, among the primary RSW parameters, hold time is comparatively understudied in relation to LME. Prior studies have typically varied hold time across discrete values with large intervals. In addition, existing work has focused on a single region of the weld cross-section, neglecting the distinct thermo-mechanical conditions at the electrode contact region, weld shoulder, and weld periphery. As a result, the mechanism by which hold time influences LME differently across these regions remains unclear, and the critical threshold beyond which further increases in HT suppress cracking has not been established.

1.5. Research aims and scope

This thesis addresses the gaps outlined above through an experimental study of Zn-coated TWIP steel subjected to RSW under controlled process conditions, supported by Finite Element Analysis (FEA) of the thermomechanical conditions during welding. The overall aim is to develop a quantitative understanding of LME and its micro-mechanisms during RSW. The specific research objectives are:

- To characterise the evolution of the Fe-Zn interfacial microstructure as a function of weld time, and to link the formation and breakdown of IM phases to the onset of LME crack initiation.
- To analyse how GB misorientation and GB orientation relative to the electrode loading axis govern LME crack path selection, and how their relative influence changes with increasing RSW weld time.
- To quantify Zn diffusion ahead of LME crack tips as a function of weld time and crystallographic direction, and to estimate GB diffusion distances relative to bulk diffusion.
- To quantify how RSW hold time influences LME at different locations and correlate these changes with the local thermomechanical conditions predicted by FEA

1.6. Scientific approach

The experimental methodology combines multi-scale microstructural characterisation with FEA, to compare measured microstructures and the thermomechanical conditions predicted by simulation. OM (optical microscopy) is used to identify LME crack locations and measure weld nugget geometry. SEM-EDS (scanning electron microscopy with energy-dispersive X-ray spectroscopy) provides elemental mapping and compositional profiles of the Fe-Zn interface, including Zn penetration ahead of crack tips. EBSD (electron backscatter diffraction) is used to determine phase distribution and GB crystallography, and XRD (X-ray diffraction) provides complementary phase identification at the weld interface. At the highest resolution, STEM-EDS (scanning transmission electron microscopy with energy-dispersive X-ray spectroscopy) on FIB (focused ion beam)-prepared lamellae to analyze of interfacial phases. FEA of the RSW process is carried out using the FEA modelling software SORPAS [29]. Zn diffusion is modelled using a 2D finite-difference solution of Fick's second law to predict bulk diffusion profiles based on FEA-derived temperature profiles. The models are validated against experimental weld nugget geometries and used to extract temperature and stress histories at key locations within the weld cross-section. Combining simulation and experiments enables mechanistic interpretation of LME behaviour that cannot be obtained from either method alone.

1.7. Thesis outline

This thesis is structured as follows: **Chapter 2** reviews the existing literature on TWIP steel, Zn coatings, RSW, and LME, covering proposed LME mechanisms, the effects of steel microstructure and temperature, and the influence of welding parameters on LME severity. It concludes by identifying the key knowledge gaps addressed in this work.

Chapter 3 describes the materials, RSW setup, and characterisation methods used throughout the thesis, and defines the experimental and modelling framework for the subsequent chapters.

Chapter 4 investigates the evolution of the Fe-Zn interface during RSW as a function of weld time. Using SEM-EDS, EBSD, STEM, and XRD, it describes the formation and breakdown of Fe-Zn IM phases at the weld shoulder and correlates these changes with FEA-predicted temperature fields. The chapter links IM phase stability and temperature profiles to the onset of LME crack initiation.

Chapter 5 examines how GB misorientation and GB orientation relative to the electrode loading axis influence LME crack path selection. A comparative analysis of triple junctions along LME cracks is used to quantify the relative roles of GB structure and mechanical alignment, and how this balance changes with increasing heat input. A GB susceptibility index is introduced to support future predictive modelling and GB engineering.

Chapter 6 presents a quantification of Zn diffusion ahead of LME crack tips in TWIP steel during RSW, based on EDS line scans in the rolling and normal directions for different weld times. The results are compared with a 2D analytical diffusion model, and the ratio of GB to bulk diffusion distance is estimated, providing an indirect measure of the dominant diffusion mechanism under welding conditions.

Chapter 7 investigates the effect of hold time on LME across three weld regions. FEA is used to interpret region-specific trends in crack number and depth, and to identify the mechanisms for dependent LME behaviour and its potential for mitigation.

The thesis concludes with a synthesis of the main findings, their implications for the understanding of LME in the Fe-Zn system, and recommendations for future work in simulation, characterisation, and process optimisation in **Chapter 8**.

References

[1] A. Candela, G. Sandrini, M. Gadola, D. Chindamo and P. Magri. 'Lightweighting in the automotive industry as a measure for energy efficiency: Review of the main materials and methods'. In: *Heliyon* 10.8 (30th Apr. 2024), e29728. ISSN: 2405-8440. DOI: 10.1016/j.heliyon.2024.e29728.

[2] M. Demeri. *Advanced High-Strength Steels: Science, Technology, and Applications - ASM International*.

[3] R. Kuziak, R. Kawalla and S. Waengler. 'Advanced high strength steels for automotive industry'. In: *Archives of Civil and Mechanical Engineering* 8.2 (1st Jan. 2008), pp. 103–117. ISSN: 1644-9665. DOI: 10.1016/S1644-9665(12)60197-6.

[4] D. Cooman. 'High Mn TWIP steel and medium Mn steel'. In: *Automotive Steels*. Woodhead Publishing, 1st Jan. 2017, pp. 317–385. DOI: 10.1016/B978-0-08-100638-2.00011-0.

[5] L. Chen, Y. Zhao and X. Qin. 'Some aspects of high manganese twinning-induced plasticity (TWIP) steel, a review'. In: *Acta Metallurgica Sinica (English Letters)* 26.1 (1st Feb. 2013), pp. 1–15. ISSN: 2194-1289. DOI: 10.1007/s40195-012-0501-x.

[6] A. A. 'A Review on the Recent Trends in Forming Composite Joints Using Spot Welding Variants'. In: *Journal of Composites Science 8:155* (2024).

[7] J. Mackowiak and N. R. Short. 'Metallurgy of galvanized coatings'. In: *International Metals Reviews* (18th July 2013). DOI: 10.1179/imtr.1979.24.1.1.

[8] H. Inui, N. L. Okamoto and S. Yamaguchi. 'Crystal Structures and Mechanical Properties of Fe–Zn Intermetallic Compounds Formed in the Coating Layer of Galvannealed Steels'. In: *ISIJ International* 58.9 (2018), pp. 1550–1561. DOI: 10.2355/isijinternational.ISIJINT-2018-066.

[9] S. P. Murugan, J. Kim, J. Kim, Y. Wan, C. Lee, J. B. Jeon and Y.-D. Park. 'Role of liquid Zn and α-Fe(Zn) on liquid metal embrittlement of medium Mn steel: An ex-situ microstructural analysis of galvannealed coating during high temperature tensile test'. In: *Surface and Coatings Technology* 398 (25th Sept. 2020), p. 126069. ISSN: 0257-8972. DOI: 10.1016/j.surfcoat.2020.126069.

[10] M. Krenn. *Characterization of Fe-Zn Intermetallic Compounds via Advanced Electron Microscopy / Author Martin Krenn*. 2025.

[11] H. Zhang and J. Senkara. *Resistance Welding: Fundamentals and Applications*. Boca Raton: CRC Press, 20th Dec. 2005. 444 pp. ISBN: 978-0-429-10159-5. DOI: 10.1201/b12507.

[12] G. Weber and S. Göklü. 'Resistance Spot Welding of Uncoated and Zinc Coated Advanced High-Strength Steels (AHSS) — Weldability and Process Reliability-Influence of Welding Parameters'. In: *Welding in the World* 50.3 (1st Mar. 2006), pp. 3–12. ISSN: 1878-6669. DOI: 10.1007/BF03263428.

[13] H. Mallaradhya, V. Kumar M, R. Ranganatha, S. Darshan and Lochan. 'Resistance Spot Welding, A Review'. In: *International Journal of Mechanical and Production Engineering Research and Development* 8 (30th Apr. 2018), pp. 403–418. DOI: 10.24247/ijmperdapr201846.

[14] D. Bhattacharya. 'Liquid metal embrittlement during resistance spot welding of Zn-coated high-strength steels'. In: *Materials Science and Technology* 34.15 (13th Oct. 2018). _eprint: https://doi.org/10.1080/02670836.2018.1461595, pp. 1809–1829. ISSN: 0267-0836. DOI: 10.1080/02670836.2018.1461595.

[15] J. E. Norkett, M. D. Dickey and V. M. Miller. 'A Review of Liquid Metal Embrittlement: Cracking Open the Disparate Mechanisms'. In: *Metallurgical and Materials Transactions A* 52.6 (1st June 2021), pp. 2158–2172. ISSN: 1543-1940. DOI: 10.1007/s11661-021-06256-y.

[16] J.-U. Kim, S. P. Murugan, J.-S. Kim, W. Yook, C.-Y. Lee, C. Ji, J. B. Jeon and Y.-D. Park. 'Liquid metal embrittlement during the resistance spot welding of galvannealed steels: synergy of liquid Zn, α-Fe(Zn) and tensile stress'. In: *Science and Technology of Welding and Joining* 26.3 (1st Apr. 2021), pp. 196–204. ISSN: 1362-1718. DOI: 10.1080/13621718.2021.1880816.

[17] H. Ueda, S. Furusako, T. Okada and S. Kikuchi. 'Liquid Metal Embrittlement in Resistance Spot Welding (Fourth Report)'. In: *International Journal of Automotive Engineering* 11.3 (2020), pp. 129–135. DOI: 10.20485/jsaeijae.11.3_129.

[18] H. Kang, L. Cho, C. Lee and B. C. De Cooman. 'Zn Penetration in Liquid Metal Embrittled TWIP Steel'. In: *Metallurgical and Materials Transactions A* 47.6 (1st June 2016), pp. 2885–2905. ISSN: 1543-1940. DOI: 10.1007/s11661-016-3475-x.

[19] C. Beal, X. Kleber, D. Fabregue and M. Bouzekri. 'Embrittlement of a zinc coated high manganese TWIP steel'. In: *Materials Science and Engineering: A* 543 (1st May 2012), pp. 76–83. ISSN: 0921-5093. DOI: 10.1016/j.msea.2012.02.049.

[20] G. Mahadevan, V. Bertolo, S. Sabooni, V. Popovich, L. A. I. Kestens and M. Hermans. 'Characterizing zinc diffusion during liquid metal embrittlement of resistance spot welded TWIP steel'. In: *Welding in the World* (10th Feb. 2026). ISSN: 1878-6669. DOI: 10.1007/s40194-026-02384-4.

[21] V. Bertolo, G. Mahadevan, R. de Kloe, R. H. Petrov and V. Popovich. 'Decoupling early-stage cracking and propagation mechanisms in liquid metal embrittlement of Zn-galvanised TWIP steel'. In: *Journal of Materials Research and Technology* 38 (1st Sept. 2025), pp. 1617–1632. ISSN: 2238-7854. DOI: 10.1016/j.jmrt.2025.08.055.

[22] L. Klinger and E. Rabkin. 'The effect of stress on grain boundary interdiffusion in a semi-infinite bicrystal'. In: *Acta Materialia* 55.14 (1st Aug. 2007), pp. 4689–4698. ISSN: 1359-6454. DOI: 10.1016/j.actamat.2007.04.039.

[23] E. E. Glickman. 'Dissolution Condensation Mechanism of Stress Corrosion Cracking in Liquid Metals: Driving Force and Crack Kinetics'. In: *Metallurgical and Materials Transactions A* 42.2 (1st Feb. 2011), pp. 250–266. ISSN: 1543-1940. DOI: 10.1007/s11661-010-0429-6.

[24] E. Glickman. 'Grain Boundary Grooving Accelerated by Local Plasticity as a Possible Mechanism of Liquid Metal Embrittlement'. In: *Interface Science* 11.4 (1st Oct. 2003), pp. 451–459. ISSN: 1573-2746. DOI: 10.1023/A:1026100112248.

[25] V. V. Popovich and I. G. Dmukhovskaya. 'Rebinder effect in the fracture of Armco iron in liquid metals'. In: *Soviet materials science : a transl. of Fiziko-khimicheskaya mekhanika materialov / Academy of Sciences of the Ukrainian SSR* 14.4 (1st July 1978), pp. 365–370. ISSN: 1573-885X. DOI: 10.1007/BF01154711.

[26] P. Gordon and H. H. An. 'The mechanisms of crack initiation and crack propagation in metal-induced embrittlement of metals'. In: *Metallurgical Transactions A* 13.3 (1st Mar. 1982), pp. 457–472. ISSN: 1543-1940. DOI: 10.1007/BF02643354.

[27] P. J. L. Fernandes and D. R. H. Jones. 'Mechanisms of liquid metal induced embrittlement'. In: *International Materials Reviews* 42.6 (1st Nov. 1997). _eprint: https://doi.org/10.1179/imr.1997.42.6.251, pp. 251–261. ISSN: 0950-6608. DOI: 10.1179/imr.1997.42.6.251.

[28] C. DiGiovanni, A. Ghatei Kalashami, E. Biro and N. Y. Zhou. 'Liquid metal embrittlement transport mechanism in the Fe/Zn system: Stress-assisted diffusion'. In: *Materialia* 18 (1st Aug. 2021), p. 101153. ISSN: 2589-1529. DOI: 10.1016/j.mtla.2021.101153.

[29] W. Zhang. 'SORPAS – The Professional Software for Simulation of Resistance Welding'. English. In: *2nd International Seminar on Advances in Resistance Welding*. 2nd International Seminar on Advances in Resistance Welding ; Conference date: 06-11-2002 Through 07-11-2002. 2002, pp. 114–129.

2 Literature review

2.1. Introduction

In recent decades, the automotive industry has placed more emphasis on passenger safety and fuel efficiency. Thus, weight reduction and improved mechanical properties are important objectives in improving vehicle performance. Steel accounts for 60-70% of the weight of a vehicle, thus improvements in steel properties of steel would offer significant benefit to the automotive industry. Advanced High Strength Steels (AHSS) were developed to address some of these requirements and the development of AHSS steel grades enable vehicle manufacturers to use thinner sheets without compromising on the vehicle's crash-worthiness and structural integrity. The reduction in weight reduces the fuel consumption and greenhouse gas emissions over its lifetime [1, 2].

The trade-off between the tensile strength and elongation is a long standing dilemma in the development of steels. This relationship dictates the mechanical performance and crash-worthiness of automotive alloys. An overview of the relationship between the tensile strength and elongation for different grades of steel is presented in the banana plot in Figure 2.1. AHSS grades show a yield strength greater than 300 MPa and tensile strength higher than 600 MPa [2]. AHSS grades are conventionally classified by their composition, heat treatment and microstructural properties. They are classified as first, second and third generation AHSS based on their application and alloying elements.

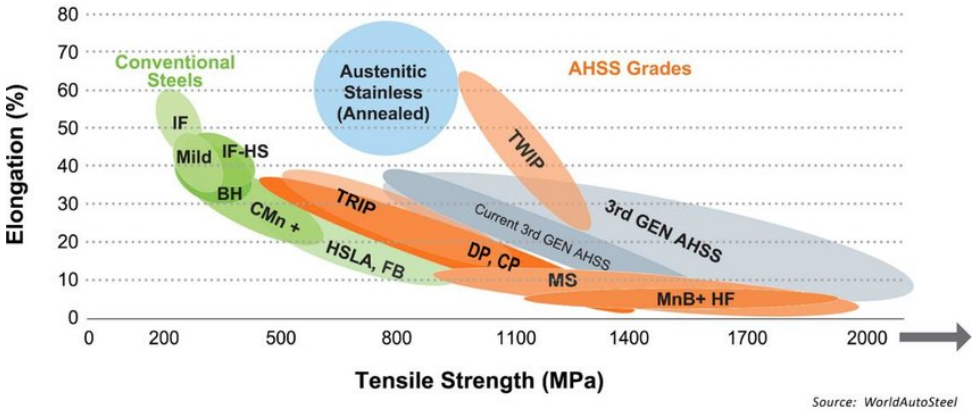


Figure 2.1: Relationship between tensile strength and elongation for various steel grades [3]

Twinning Induced Plasticity (TWIP) steels belong to the second generation of Advanced High Strength Steels (AHSS) and are characterized by high manganese contents (typically 15-30 wt.% Mn), which stabilize a fully austenitic microstructure at room temperature [4]. Their superior mechanical performance arises from deformation twinning, which continuously refines the microstructure during plastic deformation and results in a high strain-hardening rate. Consequently, TWIP steels exhibit a favourable combination of tensile strength (often exceeding 800-1000 MPa) and total elongation greater than 50-60%, placing them in the upper-right region of the banana plot in Figure 2.1. This balance makes TWIP steels attractive for automotive structural and safety-critical components, such as B-pillars, side impact beams, crash boxes, and reinforcement parts, where high energy absorption during impact is essential [5].

The superior mechanical properties of TWIP steels is governed by their metastable austenitic microstructure and low stacking fault energy (SFE), typically in the range of 15-30 mJ/m² [4]. The SFE is primarily controlled by alloying elements, particularly manganese, which stabilizes the γ-austenite phase and suppresses martensitic transformation during deformation. This ensures that plasticity is dominated by mechanical twinning rather than strain-induced phase transformation. The formation of deformation twins subdivides grains into progressively finer twin-matrix lamellae, effectively reducing the mean free path of dislocations and sustaining a high work-hardening rate [4]. Aluminum is commonly added to adjust the stacking fault energy, reduce density, and suppress carbide formation, while also improving oxidation resistance during processing. Additional elements such as silicon and carbon further contribute to solid solution strengthening and microstructural stability [6]. The resulting microstructure consists of equiaxed austenitic grains with high-angle grain boundaries and a strong propensity for twin boundary formation during deformation. These high-angle boundaries provide efficient pathways for diffusion and are energetically favorable sites for segregation. The combination of a fully austenitic structure, high grain boundary density, and chemically complex alloy composition contributes to the

distinct interfacial and diffusion characteristics observed in TWIP steels under thermal and mechanical loading conditions [6].

For automotive applications, TWIP steels are typically coated with Zn to ensure corrosion resistance throughout the vehicle lifetime. Understanding the characteristics of Zn coatings and their interaction with the steel substrate under thermal cycles such as resistance spot welding is essential for the reliable implementation of TWIP steels in automotive body structures. Although TWIP steel has many advantages, their high susceptibility to liquid metal embrittlement during RSW prevents the use of these steel grades for automotive manufacturing.

2.2. Zn coating of AHSS

In automotive sheet steels, Zn is deposited on the sheet through the hot-dip galvanizing process. In this process, the steel strip is immersed in a molten Zn bath, typically containing a small addition of Al (≈0.1-0.2 wt.%), which controls interfacial reactions and improves coating adhesion. The primary purpose of the Zn coating is to provide sacrificial cathodic protection, where Zn preferentially corrodes to protect the underlying steel substrate, and act as a physical barrier against environmental exposure. Upon contact between molten Zn and Fe during galvanizing, interdiffusion occurs at the steel-coating interface, resulting in the formation of a series of Fe-Zn intermetallic (IM) phases. These phases are described by the Fe-Zn binary phase diagram shown in Figure 2.2. The IM phases that are formed at the interface are Γ (Fe_3Zn_{10}), Γ_1 Fe_5Zn_{21}), δ ($FeZn_{10}$), ζ ($FeZn_{13}$) and the outer η phase which is essentially Zn-rich solid solution. In industrial galvanizing of automotive steels, the dominant intermetallics at the interface are usually Γ, Γ_1 and δ phases, depending on bath composition and thermal history [7, 8].

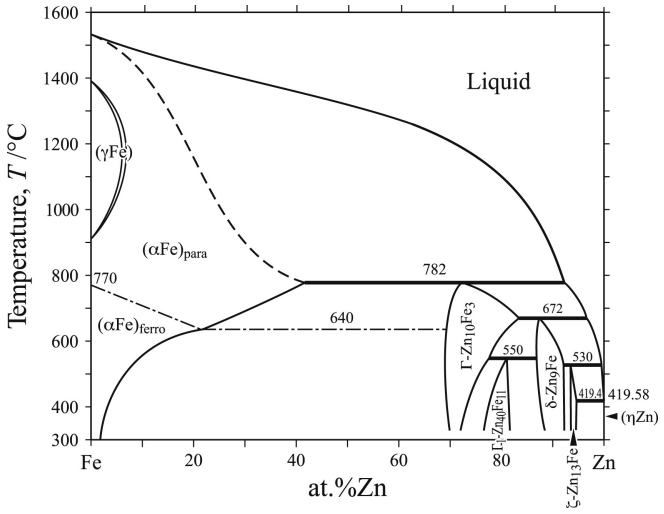


Figure 2.2: Fe-Zn binary phase diagram [9]

Zn has a melting point of approximately 427 °C and a boiling point of about 907 °C. The Fe-Zn intermetallic compounds possess higher melting temperatures than pure Zn due to their ordered crystal structures and higher Fe content [7]. The Fe-Zn phase diagram indicates that these intermetallics are stable over specific composition and temperature ranges below the peritectic and eutectic reaction temperatures. The presence, continuity, and morphology of these intermetallic layers depend on diffusion kinetics and temperature evolution during processing [8].

2.3. Resistance Spot Welding

Resistance Spot Welding (RSW) is the primary joining method used in automotive body-in-white assembly due to its high speed, repeatability, and suitability for thin sheet steels. In RSW, two or more overlapping steel sheets are joined by passing electric current through the sheets via water-cooled copper electrodes. The resistive heating at the sheet interface causes localized melting and the formation of a weld nugget, which solidifies upon cooling to form a joint [10]. The RSW electrodes conduct the welding current, clamp the sheets together, and apply the mechanical force necessary for nugget formation. It is usually made of copper due to its electrical and thermal conductivity, which ensures efficient heat generation and dissipation. Several parameters govern the RSW process. These include:

- **Weld current**: the magnitude of electrical current applied, which determines the rate of resistive heating at the interface. It is measured in kA.
- **Electrode force**: the mechanical pressure applied by the electrodes, influencing contact resistance, heat generation, and nugget consolidation.
- **Squeeze time**: the duration for which the electrode force is applied before current flow begins, ensuring sufficient contact between sheets
- **Weld time (WT)**: the duration over which the current and force is applied; longer weld times increase heat input and melt volume
- **Hold time (HT)**: the period during which electrode force is maintained after current cessation, allowing solidification and preventing expulsion of molten material.

During RSW, the temperature and stress within the weld cross-section evolve over time. As current passes through the steel sheets, resistive heating causes temperature rise at the interface, forming a molten weld nugget while surrounding material remains solid. The highest temperatures are concentrated in the weld center, with a thermal gradient toward the edges. The peak temperature and spatial distribution are primarily controlled by weld current, weld time, electrode geometry, and sheet thickness [11].

Simultaneously, mechanical stresses develop due to electrode force and thermal expansion mismatch between the heated weld zone and the cooler surrounding material. The combination of high local temperatures and applied or residual tensile stresses is particularly critical in coated steels, where molten Zn is present. These conditions create a driving force for grain boundary penetration by the liquid metal, enabling crack

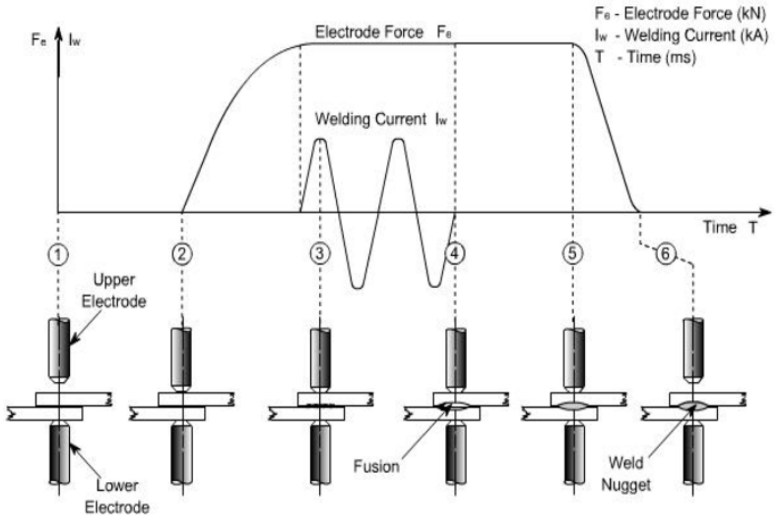


Figure 2.3: Stages of RSW process [12]

initiation and propagation along susceptible boundaries [13, 14]. Many 3rd generation AHSS grades require multi-phase weld schedules to optimize weld strength, which leads to increased embrittlement susceptibility [1]. Finite element simulations of temperature and stress evolution in spot welds show that short weld times produce smaller nuggets with steep thermal gradients, while longer weld times increase both nugget size and the duration of elevated temperatures [15, 16].

2.4. Liquid Metal Embrittlement (LME)

The abrupt rupture of a solid metal in direct contact with a liquid metal under stress and elevated temperature conditions is known as liquid metal embrittlement. These conditions of elevated temperature and stress can be observed during RSW. Despite their superior strength and elongation properties, Zn coated AHSS face a unique challenge in surface cracking due to LME. LME has been studied for several decades and has been known since the 1870s. LME can be observed in many solid/liquid couples including Al_{solid}/Ga_{liquid}, Ni_{solid}/Bi_{liquid}, and Cu_{solid}/Bi_{liquid} [17]. LME occurs in automotive manufacturing during the welding of galvanised steel sheets. Contact between a poly-crystalline steel grade and liquid Zn under specific temperature, stress, strain rate, and microstructural conditions can result in rapid penetration of the liquid Zn into the steel substrate and result in crack formation due to grain boundary decohesion. The formation of these cracks has a negative impact on the mechanical performance of the welds and should thus be avoided. The observation of LME is dependent on the interface energy between grain boundaries γ_{GB} and the solid-liquid interface energy γ_{SL} and is energetically favourable when $\gamma_{GB} \geq 2\gamma_{SL}$ [18]. A schematic representationof the LME process is shown in Figure 2.4.

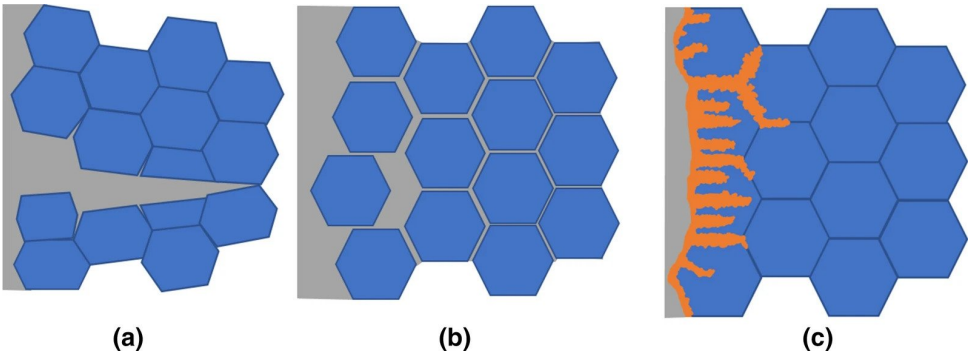


Figure 2.4: Schematic representation of the LME process to show (a) interfacial cracking assisted by liquid metal, (b) decohesion of grain boundary and (c) embrittlement of liquid metal in solid matrix [1]

2.4.1. LME MECHANISMS

Although it has been known and observed for several decades, the exact mechanism of LME has not been fully understood due to the general complexity of the phenomenon, a lack of *in-situ* experimental evidence, and potential differences in the mechanism for the various LME couples. LME mechanisms are classified based on their fracture mode as well as the embrittler metal transport mechanism. LME models can be classified based on their controlling mechanism in the following ways:

- Ductile fracture models
- Brittle fracture propagation models
- Grain boundary diffusion models

A summary of the various LME mechanisms discussed is presented in Figure 2.5

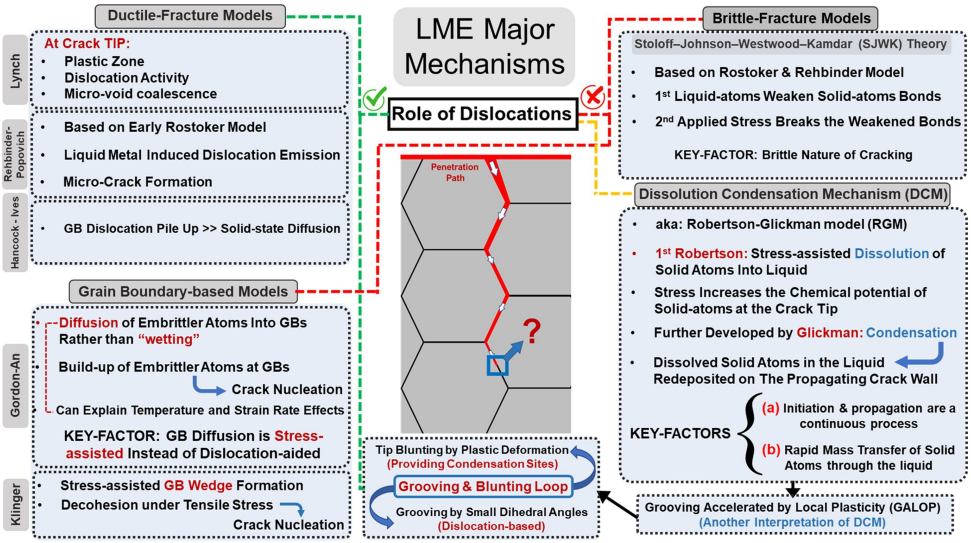


Figure 2.5: Summary of the various proposed mechanisms to explain LME behaviour [13]

Ductile fracture models

Early experiments observed that plastic deformation was a necessary criterion for LME. Hancock and Ives proposed an early model suggesting that dislocation pile-ups are formed at grain boundaries as a result of plastic deformation ahead of the crack tip. These pile-ups interact with atoms diffusing in front of the crack tip from the liquid metal, triggering embrittlement [19]. Rebinder and Popovich expanded on the ductile fracture mechanism by hypothesising that the interface between solid and liquid metals was a site of enhanced dislocation density. The increase in dislocation emission hardens the surface locally. This hardened area then develops micro-cracks, which move quickly through the work-hardened material until slowing down when they reach the ductile base material [20]. Lynch later expanded on this idea, predicting that liquid metal atoms are adsorbed at the crack tip promoting localised slip. These dislocations propagate the crack just ahead of the tip in the plastic zone [21]. Despite potentially being a dominant mechanism in LME findings, Fe-Zn systems exhibit little indication of ductile fracture in experimental tests, as demonstrated by Kang et al., who investigated the concentration of dislocations near the crack tip using high resolution microscopy [22]. Thus, this model will not be discussed further pertaining to the embrittlement of Zn in steels.

Brittle fracture and Dislocation Condensation Models

According to Rostoker et al., the embrittling liquid metal is adsorbed in the solid metal surface, lowering the surface energy of the substrate. The study hypothesised the decrease in surface energy weakens the atomic bonding in the substrate, causing brittle fracture by lowering fracture strength. The model assumes that subsurface slip causes

dislocation pile-ups, which leads to crack propagation at the crack tip where the bonds are broken [23]. The Stolof-Johnson-Westwood-Kamdar (SJWK) model developed and expanded on the Rostoker model. According to the SJWK model, the liquid metal weakens the base metal's bonding through chemisorption. These weakened bonds then break, causing the crack to spread. It is important to note that this model does not predict plastically deformed fracture surfaces [24, 25]. Robertson proposed a stress-assisted dissolution model in which solid atoms dissolve in the embrittler medium and then re-deposit on the crack surface. It works by increasing the chemical potential of the solid near the crack tip, which promotes local dissolution. The dissolved atoms generated at the crack tip are carried away by the liquid embrittler and further condensed on the crack surfaces as the crack propagates. Glickman proposed a similar mechanism that builds on Roberstson's model and is based on the concept of grain boundary grooving. This mechanism, known as Grooving Accelerated by LOcal Plasticity (GALOP), states that local plasticity causes the blunting of grain boundary grooves under tension. According to the model, which is schematically shown in Figure 2.6, 'shelves' are formed at the crack, reducing the distance for the embrittler atoms to diffuse. The short distance for diffusion and rapid liquid diffusion cause the groove to deepen.

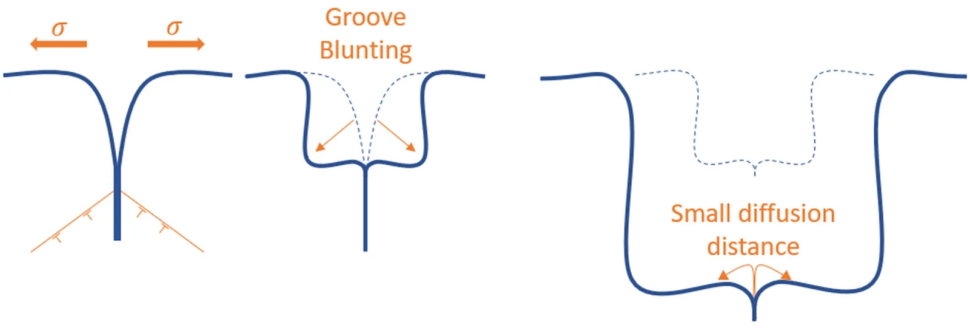


Figure 2.6: Changing geometry of grain boundary groove due to blunting in GALOP LME mechanism [26]

Grain boundary diffusion models

According to grain boundary-based models, stress-assisted grain boundary diffusion occurs before liquid metal penetration. Importantly, these models assume that embrittler atoms penetrate the solid via high diffusion paths rather than by wetting the grain boundary [13]. Krishtal and Gordon-An proposed LME models that predicted crack initiation and propagation are distinct stages in crack formation, each thermally activated with very different activation energies. The models describe the brittle fracture that occurs at the grain boundaries in a defined temperature range of ductile to brittle transition. The lower limit of this temperature range is controlled by the activation energy necessary for diffusion. The higher limit is governed by the temperature required for the liquid metal to diffuse into the grain, reducing the concentration of the embrittler at the grain boundaries required for decohesion, as shown in Figure 2.7. The model also describes the factors affecting this ductile to brittle transition like strain rate - higher

strain rates increase the transition temperature. According to the study's findings, there is a "critical" stress level for the embrittlement phenomenon to occur. Furthermore, the magnitude of the critical stress was shown to decrease with increasing temperature, which would affect the kinetics of the proposed diffusion mechanism [27]. Klinger and Rabkin expanded on the Gordon-An model and proposed that diffusing atoms in the GB relax the elastic stress field surrounding the GB, changing the driving force for GB diffusion. The study determined a qualitative expression for the time-dependent stress field and concentration distribution in the region surrounding the GB. The study proposed a 'diffusion wedge' would form at the GB vicinity where the diffusing atoms would plate out in a time-independent shape as the size of the wedge proportional to $t^{1/3}$ where t is time. The stress gradient induces a chemical potential gradient, resulting in an additional diffusion flux that increases the embrittler atom's penetration of the grain boundary [28].

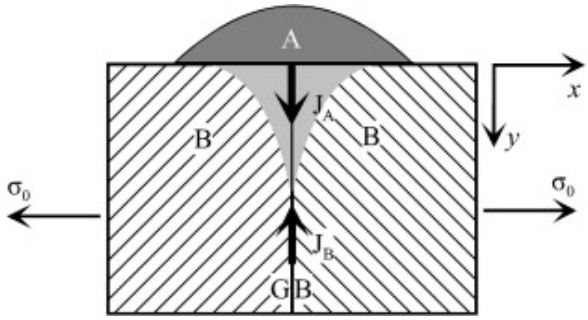


Figure 2.7: Diffusion of embrittler atoms (A) in the grain boundary of solid metal (B) under external stress and elevated temperature [28]

Fe-Zn intermetallics (IM) play an important role at controlling LME at the interface of the steel substrate and Zn coating during RSW. When the Zn coating is subjected to temperatures above 427 □ under electrode force, it reacts with Fe to form IM compounds. The presence, thickness, and stability of these compounds determine how Zn is transported and how it remains available at the interface [29–33]. According to Murugan *et al.*, at 700 °C the δ phase in the interface coating transforms into liquid Zn and Γ. Under these conditions, Γ is not stable with Fe, leading to the formation of a thin Zn-rich ferritic (α-Fe(Zn)) layer as Zn diffuses into Fe. Zn redistribution between α-Fe(Zn), Γ, and liquid Zn continuously re-establishes equilibrium, with Zn ultimately moving from the liquid phase through Γ into the steel [34]. Lee et al. reported that an Al-rich diffusion-inhibiting layer suppresses the formation of Fe-Zn IM at the Zn/steel interface, but this layer is destroyed during RSW due to heat and electrode stress. In cracked regions, fine α-Fe(Zn) particles appear on the steel surface and cracks propagate along austenite grain boundaries beneath this layer [35]. The crack area consists of Γ and α-Fe(Zn), showing that Zn infiltrates grain boundaries. The α-Fe(Zn) particles increase interfacial area and act as brittle phases, providing pathways for Zn infiltration and thereby accelerating LME, which becomes more severe with higher welding current [36]. Additionally, Al oxide zones at the Fe-Zn interface have been

observed in previous studies. These oxide zones have a grain size that is independent of the relative concentrations of Al in the coating or the steel [37–39]. When these Al oxides and Fe-Zn IMs break down, Zn from the coating is available to diffuse into the GBs of the substrate. Ikeda et al. reported that in grain boundaries infiltrated with Zn but not yet cracked, a nanoscale Γ phase could be characterized. The observation of this phase indicates that strain heterogeneities are locally enhanced within the grain boundary network, and IM formation does not occur only after cracks develop and liquid Zn penetrates, but instead weakens grain boundaries and promotes crack initiation [40]. Although GB diffusion models provide a thermodynamic and kinetic framework for understanding LME crack initiation and propagation, several limitations remain. First, most models are qualitative and rely on simplified assumptions regarding uniform grain boundary structure, steady-state diffusion conditions, and idealized stress fields, which do not fully represent the highly transient thermo-mechanical conditions present during RSW. Second, experimental validation of stress-assisted grain boundary diffusion remains challenging due to spatial resolution limits in detecting early-stage embrittler penetration ahead of cracks. As a result, the quantitative relationship between the RSW process, diffusion distance, and crack initiation remains insufficiently established. Furthermore, the interaction between grain boundary diffusion and bulk diffusion under these welding conditions is not fully resolved, particularly in systems such as Fe-Zn where interfacial reactions and phase transformations simultaneously occur. These limitations highlight the need for direct experimental quantification of embrittler diffusion under controlled welding parameters and for coupling diffusion analysis with realistic thermal profiles - issues that are addressed in the subsequent chapters of this thesis.

2.5. Effect of steel microstructure on LME

Lee et al. studied the microstructural evolution of LME in TWIP steel sheets and observed that LME cracks have randomly oriented α-Fe(Zn) particles along austenitic grain boundaries, as shown schematically in Figure 2.8. The study postulated that the α-Fe(Zn) particles increased the area of the interface and played an important role in accelerating LME by providing a path for the infiltration of liquid Zn [41]. Cho et al. investigated LME behaviour in Zn coated press-hardened steel. They concluded that LME crack formation is caused by a thin layer of α-Fe(Zn) at austenitic grain boundaries formed by Zn diffusion [42]. Kang et al. investigated LME in TWIP steels and found that Zn penetrates into the steel matrix along the grain boundaries. The observations proposed two models of LME - percolation of liquid Zn and grain boundary diffusion. Figure 2.10 shows a cross-sectional SEM micrograph of a Zn penetration in a Zn-coated TWIP steel [22]. The failure was ultimately caused by intergranular brittle fracture. Murugan et al. investigated the effect of liquid and α-Fe(Zn) on the LME of medium Mn steel and discovered that the thermodynamic stability and isothermal solidification of liquid Zn governed the sensitivity to LME. The diffusivity of Zn in Fe and the partitioning of liquid Zn governed the thermodynamic stability. According to the findings of the study, LME is controlled by the breaking of the α-Fe(Zn) layer, which directs liquid Zn to the grain boundaries of the Fe matrix [36]. Bhattacharya et al. conducted the most comprehensive study on the influence of starting microstructure on

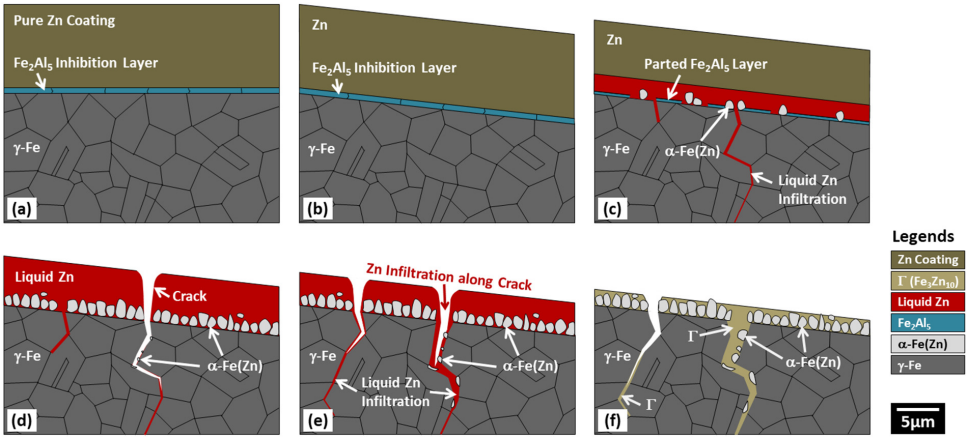


Figure 2.8: Schematic diagram of microstructural evolution during LME (a) microstructure before RSW (b) formation of pressed zone due to RSW (c) melting of Zn and formation of α-Fe(Zn) particles (d) crack formation in the Zn penetration area (e) Zn penetration along austenite GBs (f) transformation of liquid Zn to Γ phase inside the crack [41]

the severity of embrittlement in Zn coated AHSS. In the study, hot tensile tests were performed on steel grades with QP, martensitic, TBF and DP microstructures at various temperatures between 500 °C and 700 °C on a thermo-mechanical cycle that generated stresses known to cause LME. The results of the study showed that the severity of LME was considerably lower in DP steel at lower temperatures between 500 and 700 °C compared to the other steel grades that were tested which showed similar susceptibility to LME. The study concluded that the pre-austenitic grain boundaries of the TBF, martensite and QP microstructures were low energy paths for crack propagation and hence preferred for embrittlement. The DP steel's lower area fraction of the same kind of GB due to its generation via inter-critical annealing reduces the availability of low energy paths for crack propagation and is shown in Figure 2.9.

Ling et al. attempted to quantitatively measure Zn content in LME-affected regions; however, limitations in characterization resolution prevented reliable quantification of Zn diffusion along GBs [43]. RSW process parameters also have an effect on LME, with studies showing that LME is more severe when the welding heat input is higher, resulting in more severe LME when the welding current or weld time is increased [30, 44–46]. While studying LME severity by analysing the number of cracks and crack dimensions is useful, it offers an incomplete picture because it does not account for the underlying Zn diffusion mechanisms that drive crack formation and propagation [28]. Understanding the overall Zn diffusion, particularly its interaction with stress and temperature gradients, is crucial for a more comprehensive understanding of LME.

Numerous studies have investigated the effect of microstructure on the observation of LME in AHSS grades. Hot tensile tests were performed to study the severity of LME and it was found that TWIP steels showed a higher susceptibility to observe LME cracks compared to TRIP assisted bainitic ferrite steel or dual phase (DP) steel with ferritic and

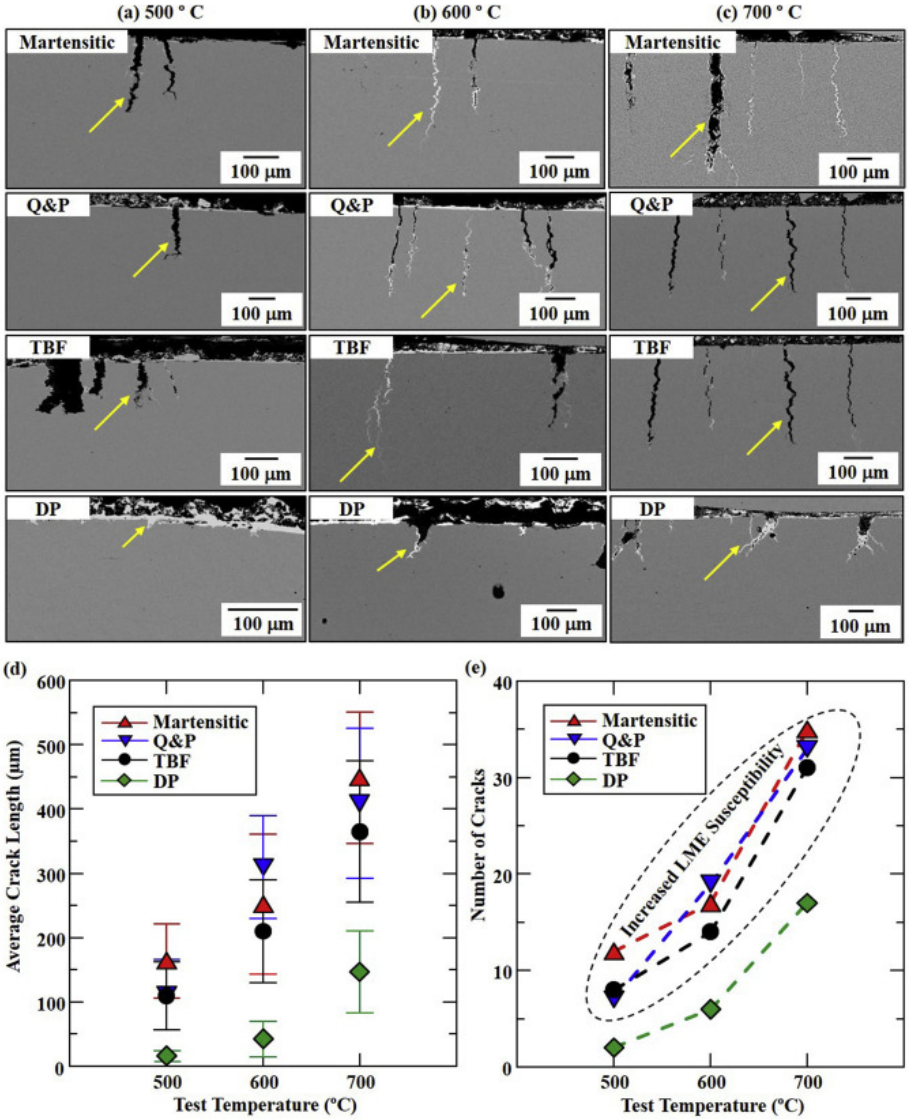


Figure 2.9: SEM micrographs of LME crack profile at (a) 500 °C (b) 600 °C (c) 700 °C (d) Average length of LME crack (e) Average number of LME cracks in hot tensile tests [47]

martensitic phases. These studies also revealed that among the various generations of AHSS grades, fully austenitic microstructures have a higher likelihood of showing LME behaviour [33, 44, 48]. The severity of embrittlement is also heavily influenced by the presence of alloying elements. Kahkonen et al. showed that silicon composition in AHSS grades was closely related to the UTS of material and a higher percentage of silicon would reduce the UTS. The reduction of the UTS results a lower critical stress for embrittlement to occur, thus demonstrating that increasing the alloying composition of Si also increases LME susceptibility [49]. Chen et al. investigated the effect of alloy segregation at the α/γ-Fe interface on LME behaviour. Using first principles methods, the influence of alloying elements (Nb, Mn, Al, Cr, Mo, Ti) in steel segregation on LME was studied and it was observed that the alloying elements enable segregation of atoms from the γ to the α side of the phase interface. The Zn coating causes the bonds between the Fe atoms to weaken at the Fe-Zn interface, while the segregation of alloying elements increases the Zn induced cohesion at the interface. The study found that after Zn enrichment, the cohesion of phase boundaries improves due to the strengthening of the Fe bonds by the solute. When Zn atoms and alloying atoms are on the same interface, the strengthening effect is visible [50]. [47].

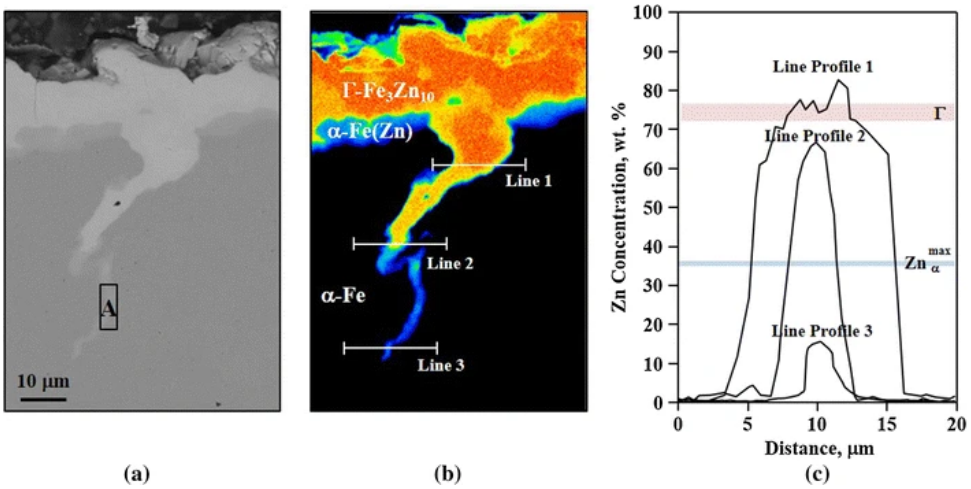


Figure 2.10: (a) SEM micrograph of Zn penetration in IF steel where Á represents the EPMA site (b) FE-EPMA elemental distribution of Zn (c) Zn concentration line profiles along the lines indicated in (b) [22]

Razmpoosh et al. studied LME in laser beam welding of 22MnB5 steel and proposed that partial melting of the Fe-Zn δ and Γ/Γ_1 phases in the Zn coating resulted in Zn penetration along the high angle grain boundaries of austenite, which led to intergranular decohesion and eventual failure. The study postulated that the accumulation of Zn along the HABs over the maximum solubility in the austenite, promotes α-Fe(Zn) formation. The formation of α-Fe(Zn) along Zn-penetration area assist the loss of ductility due to the higher Zn diffusivity in α-Fe [51]. Razmpoosh et al. investigated the effect of

grain boundary chemistry on crack propagation in LME in another study. The study concluded, using atom probe tomography, that stress-assisted diffusion in front of the LME cracks allowed for the transport of embrittler atoms, eventually leading to grain boundary decohesion. The study also found that increasing stress caused Cr atoms to segregate to high angle grain boundaries, which accelerated GB decohesion [52].

2.6. Effect of temperature on LME

LME can be observed in a defined temperature range for each solid/liquid metal pair and is defined as the 'ductility trough' for that pair. LME severity increases with the brittle-to-ductile transition temperature. This observation can be explained by the opposing effects of plastic deformation and brittle fracture caused by liquid metal exposure. Other factors, such as strain rate, influence this transition temperature; a lower strain rate lowers the transition temperature due to less thermal activation of plasticity. Temperature also plays a role in accelerating the kinetics of the embrittlement [1]. It has also been observed that the ductility trough disappears beyond 907 °C, which is the boiling temperature of liquid Zn. Figure 2.11 compares the fracture energy between a bare sample and an electrogalvanised sample and shows the effect of temperature on reducing fracture energy in the ductility trough. Barthelmie et al. studied LME during RSW of Mn alloyed TWIP steels by performing hot tensile tests on samples with and without a Zn coating layer. The study observed that strength was lowered by 20% and elongation reduced by 50% in the samples with the Zn coating compared to the sample without the coating at 600 °C [53]. The temperature also affects the kinetics of grain boundary diffusion and accelerates the diffusion of Zn into the steel matrix which is an essential step in the observation of LME. The effect of temperature is prominently observed during joining processes like RSW discussed in Section 2.3. The temperature gradient in the base metal is also a source of thermo-mechanical stress that adds to the applied tensile stress contributing to embrittlement [33].

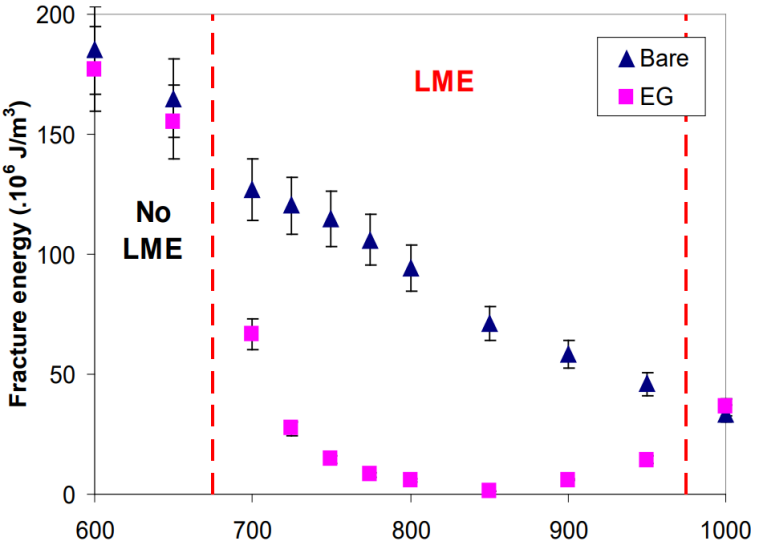


Figure 2.11: Comparison of fracture energy as a function of temperature illustrating the severity of LME in Zn coated steel sample [48]

2.7. Effect of Stress on LME

Early studies have observed that embrittlement does not occur in the absence of plastic deformation and purely elastic stress is insufficient to observe this phenomenon. Nicholas et al. suggested that there exists a critical stress below which the phenomenon is not observed [54]. The stress state also plays an important role in the mechanism of LME as discussed in Section 2.4.1. The stress field contributes Zn diffusion from the GBs near the crack tip towards the bulk metal matrix that causes the propagation of the crack and results in tensile stresses during the cooling cycle [27]. Figure 2.12 illustrates the ductility loss in a steel sample due to the penetration of Zn in the steel matrix.

Multiple other studies have validated this theory and observed a critical stress above which LME phenomena was observed. Beal et al. studied the correlation between stress state and LME severity in Zn coated TRIP steels and observed that a critical stress above the yield stress of the steel sample was necessary for embrittlement to occur. They observed a stress gradient in the weld sample around the RSW nugget and proposed that the LME sites would be found in locations where the local stress was above the observed critical stress [48]. Jung et al. studied the contributing factors affecting LME susceptibility and found the critical stress to be corresponding to a strain of 0.4% in the ductility trough at a temperature of 700 °C. The authors postulated the existence of a threshold concentration of Zn above which the sample being tested cannot accommodate any more stress. The authors found this observation to be valid for multiple grades of AHSS like TWIP and DP steels. The study also correlated the magnitude of applied stress to the severity of the LME phenomena - a higher applied stress corresponded to the observation of more severe LME [44]. In the context of RSW, the local stress state is determined by the position of the electrode, welding

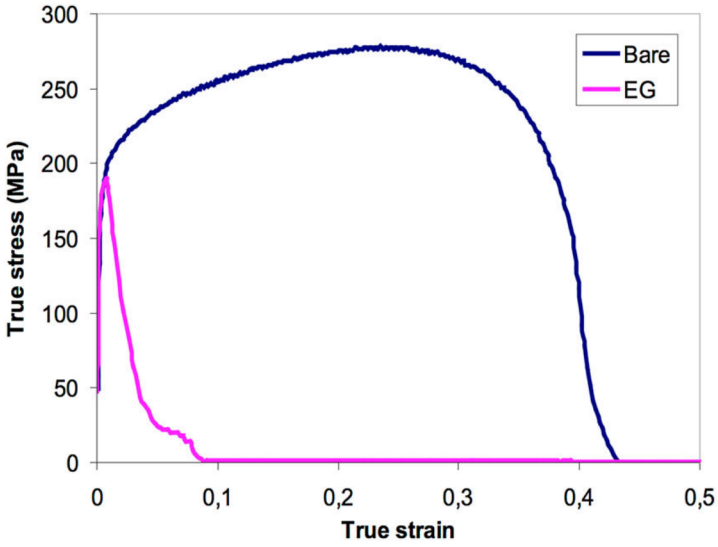


Figure 2.12: Comparison of true stress vs true strain in steel samples with and without an electro-galvanized Zn coating layer [48]

process parameters and the type of cracks that are formed. FEA simulations have proved to be a useful tool to model the stresses during RSW in order to predict the formation of welding cracks. Beal et al. simulated the stress cycle during RSW and found that compressive stresses prevail over tensile stresses in both x and y directions. This observation was the result of the competing effects of the force applied by the welding electrode and the thermo-mechanical forces due to thermal expansion [48]. It is also known from earlier studies that tensile stresses are required for LME to occur. FEA simulations by Jung et al. demonstrate that the holding time phase of RSW cycle causes the cooling of the solid metal in a constrained environment. The study theorised that the location of cracks formed due to LME would be observed where the local stress was higher than the critical stress within the temperature range of the ductility trough [44]. Several studies have been conducted in order to reduce the effect of stress on crack formation and propagation during LME. In the RSW process, a large number of such measures were investigated in order to reduce residual stresses in the weld zone below the critical stress and avoid LME. Sierlinger et al. discovered that lowering the heat input during RSW lowers tensile stresses during the cooling cycle, preventing crack formation. It was also discovered that increasing the electrode force or hold time would help to maintain a compressive stress state and thus suppress crack formation [55].

2.8. Effect of welding on LME

As discussed in Section 2.3, RSW is the main technique used for joining AHSS components. This section explores LME in the context of RSW and the correlation between the welding process and LME phenomena.

2.8.1. Location of LME cracks in RSW

Numerous studies and welding standards were developed to categorise the various types of welding cracks. AWS classification did not take into account the mechanism for crack formation and only used the effect of the crack on the mechanical properties of the solid matrix to differentiate the various crack types [56]. Choi et al. studied the crack formation during RSW and proposed 3 regions based on the stress and temperature conditions experienced during welding [46]. Murugan et al. conducted a comprehensive study on the metallurgical and thermo-mechanical origins of cracks in RSW and provided a classification of crack types that could be seen in the RSW process [34]. The study proposed 4 distinct categories of classifying LME cracks- of Type A, B, C and D. A brief description of each of the crack types is presented below:

- Type A: These cracks are comparatively large in size that can go up to 800 μm in the underneath the electrode extending to the weld nugget and is formed in the fusion zone. The fusion zone upon solidifying enabled the liquid metal to penetrate through the grain boundaries driven by tensile stress.
- Type B: This type of crack is formed in the weld shoulder and can have a maximum length of 100 μm. The temperature differential at the interface of the embrittler and solid metal results in the concentration of tensile stresses, which stops after the electrode's annular region touches the sheet during the dwell time making the stresses compressive in nature. The small amount of time this region experiences tensile stresses results in a comparatively shorter crack length.
- Type C: The stresses in this region are tensile in nature through the entire cycle of the RSW process, which results in the formation of large cracks with lengths up to 1200 μm. The microstructure in this region comprises of fully austenitic grains. This location is not in direct contact with the RSW electrode thus providing the embrittler atoms sufficient time to penetrate through the crack.
- Type D: This type of crack is formed at the solid interface outside the weld nugget. These are formed due to the tensile stresses formed during the cooling cycle experienced by the region during the hold time of the electrode. The number of these cracks are comparatively lower in number and they have a length of less than 100 μm

The morphologies of the various crack types are shown in Figure 2.13.

2.8.2. Effect of welding process parameters on LME

As discussed previously in Section 2.3, the welding current, welding time, and electrode force are the three most important parameters in RSW. The welding current and weld time contribute towards the heat input and has an effect on the temperature gradient of the weld and fusion zone. The heat input also results in the development of thermo-mechanical stresses that contribute towards the tensile stresses required to initiate crack formation in LME. The electrode geometry and electrode force have a large contributing effect on the tensile and compressive stresses that develop in the process.

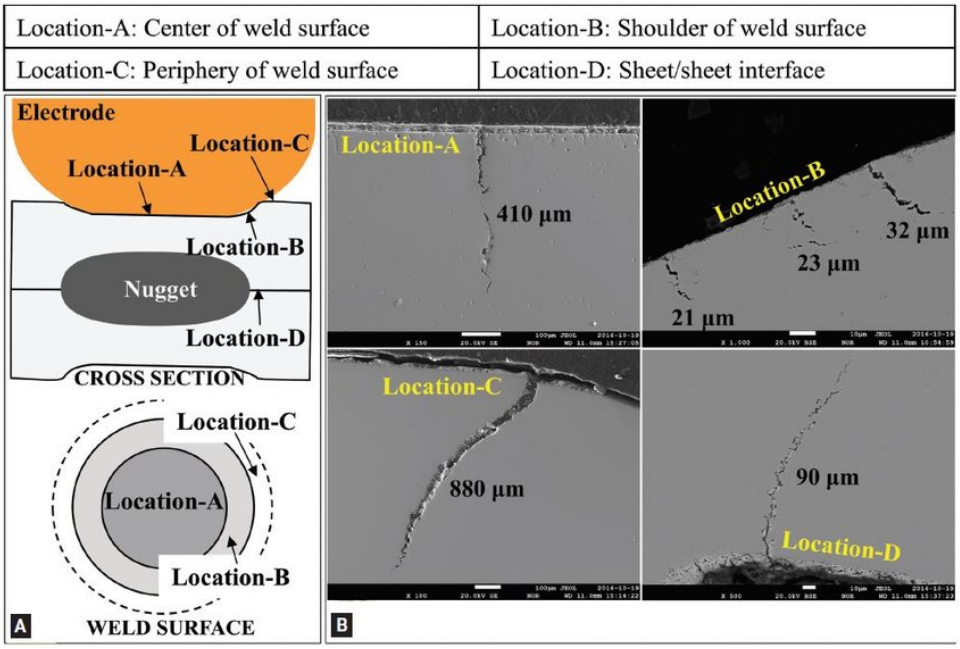


Figure 2.13: (a) Schematic representation of LME crack location (b) SEM micrographs of various types of LME cracks [34]

Kim et al. conducted a study to evaluate the correlation between welding process parameters on fatigue properties and surface cracks of Zn coated AHSS. The study concluded that the susceptibility for LME increased with increasing heat input above the critical stress. The study found that the LME cracks did not have a significant impact on the fatigue life, but using a 'pre-current' method of modifying the RSW current waveform would reduce the occurrence of cracks [45]. Dong et al. studied the effect of RSW current on Zn coated Q&P steel. The study investigated the correlation between the ejection current, defined as the current needed to eject the molten metal from the weld due to the stresses in the nugget, and the initiation of LME. It found that crack initiation was observed above the ejection current and contributed to the heat input which increases the rate of Zn diffusion into the steel matrix and expansion of GBs. The potential for suppressing crack formation in LME by controlling the welding current was deemed feasible in this study [29]. Wintjes et al. proposed a pulsed RSW schedule to reduce the susceptibility of LME severity. The study proposed that pre-pulse and pulse welding enabled the stabilisation of the Zn coating by forming intermetallics with the Fe and thus resist crack propagation. Two successive weld pulses proved to be the optimum schedule to enable LME resistance as the supply of embrittler atoms is limited while simultaneously avoiding the build up of tensile stresses in the shoulder of the weld [57]. Ling et al. showed that the length of the deepest crack was directly correlated with the increasing weld current and the other welding parameters like hold time and

force had a lesser effect on LME [30]. DiGiovanni et al. also performed experimental studies on the effect of a ramping welding current on the susceptibility of LME. The study concluded that the downward ramped current reduced LME behaviour leading to lower number of cracks and reduced crack depth per sample. In comparison to the standard RSW process, the ramped current was designed such that the liquid Zn phase was under tension for a lower amount of time and experienced lesser tensile stress after the application of force by the electrodes [58]. A schematic plot of the ramped RSW current schedule is shown in Figure 2.14.

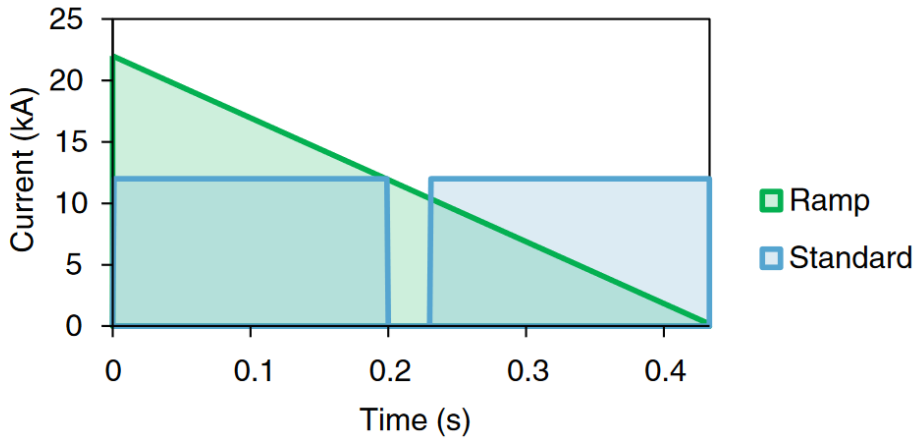


Figure 2.14: RSW welding current schedule for standard and ramped conditions to prevent LME [58]

In the RSW process, the electrode plays a crucial role in the stress state of the weld and the fusion zone. Numerous studies have investigated the effect of the electrode material and geometry on the onset of LME. Murugan et al. studied the influence of the electrode design on LME susceptibility of Zn coated AHSS alloys during RSW both experimentally and through numeric modelling. The study investigated two distinct electrode designs: a dome (B) type electrode with a graded tip diameter and a radius type with a different radius of curvature, as shown below in Figure 2.15. The study concluded that the dome type electrode displayed a higher susceptibility to LME compared to the radius type due to the lower contact area at the interface between the electrode and metal sheet. A general relationship between the geometric parameters of the electrode and LME susceptibility was established by experimental study which showed that an increasing electrode radius R reduced the tendency for LME. The nature of surface to surface contact between the electrode and sheet surface was found to be the most important parameter that governed the temperature and stress state of the weld. The study proposed the formulation of a new parameter called the 'geometric factor' to quantify the effect the electrode geometry had on the temperature and stresses of the weld [59].

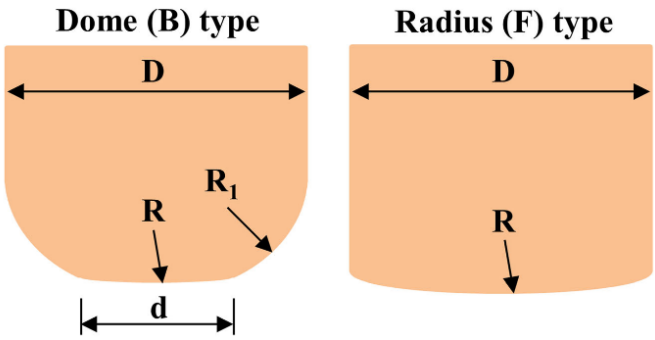


Figure 2.15: Schematic geometry of dome and radius type electrode design in RSW process [59]

Based on the findings of these studies, it can be concluded that there are several methods for reducing the susceptibility of LME during RSW of Zn coated AHSS grades. This can be accomplished by adjusting the welding process parameters to adjust the heat input and thermo-mechanical stresses that develop during the cooling cycle, adjusting the current schedule, or even changing the geometry of the electrode to adjust the contact area between the electrode and sheet. However, the welding process has only a second-order effect on the penetration of Zn into the grain boundaries of the AHSS alloy. Controlling the microstructure of the alloy and reducing the availability of pre-austenitic grain boundaries for liquid Zn to penetrate has a more direct effect on combating LME.

2.9. Modelling of LME

Numerical simulations have been a useful tool in understanding the mechanisms that govern material behaviour. Different approaches to numeric modelling have been used to better understand the LME process. Ab-initio calculations of interatomic forces between embrittler atoms and solid metal have been applied to understand the origin of the driving forces behind LME. Finite element modelling has also been used to simulate the stresses and temperature fields during RSW. This section provides an overview into the modelling techniques in multi-scale LME simulations.

2.9.1. Atomic scale modelling

Various theories explaining the origin of the driving force behind LME were discussed in detail in previous sections. The origin of 'LME specificity,' defined as the observation that LME occurs only in specific solid-liquid metal couples, was discovered to be particularly contentious, with no agreement on a quantitative model explaining this behaviour. Early theories proposed models governed by atomistic parameters such as grain boundary interface energy, atom bonding energy, and dislocation density, among others. Despite compelling arguments about the relationship between these atomic parameters and LME, they did not completely predict the embrittling behaviour [23, 27]. A number of studies used first principle calculations like Density Functional

Theory (DFT) to investigate grain boundary behaviour during embrittlement and the mechanisms that underpin the process. Bauer et al. used ab-initio thermodynamic techniques in conjunction with DFT calculations to investigate LME in alloyed steel samples with symmetrically tilted GBs. According to the findings, the embrittler atoms had low cohesion, which reduced the interfacial energy of the grain boundary as well as the surface energy of Fe. The rapid decrease in surface energy as Zn concentration increased in the metal bulk was attributed as the driving force of embrittlement. However, this approach was dependent on the assumption underlying the embrittler transport model, which determines the chemical potential choice. With this approach, it is difficult to pinpoint the cause of grain boundary weakening because different models necessitate different chemical potentials [60]. Hu et al. used DFT first-principles calculations to model solute atom segregation and its impact on GB cohesion and thermodynamic stability. The study discovered that the energy required for solute segregation is generated by a combination of strain and chemical contributions. The segregation of alloying elements near the grain boundaries reduces cohesion strength and induces bond cleavage above a threshold value of strain, resulting in the breakdown of the GB structure [61]. Shweinfest et al. proposed that the size effect of solute atoms induces the presence of localised tensile stresses in the system which aid in the decohesion of grain boundaries in their investigation of LME in Cu/Bi alloys. The study showed that the segregation of solute atoms pushed the solid metal (Cu) closer to ductile-brittle transition and the observation could be extended as a general result in any binary alloy system which can show a size effect [62]. Gibson et al. published a study surveying 81 separate studies of 400 DFT based calculations investigating the effect of solute atoms on the decohesion of GBs and its effect on the changing mechanical properties of the polycrystal. This study summarised the effect of different alloying solute atoms to accelerate embrittlement and its potential to limit the cohesion between GBs. Figure 2.16 shows the embrittling potential of different alloying elements as a function of the difference in elemental cohesive energy for Fe [63]. Scheiber et al. investigated the influence of the segregation of alloying elements like Al and Si on the embrittlement of Zn coated steels. The effect of these alloying elements is evaluated by computing the energy required for binding and segregation at the free surfaces as well as grain boundaries. It was also found that the Si atoms did not compete with Zn and Al atoms at the GB sites and that the interaction was repulsive between Zn and Al. Si was found to marginally improve the cohesion between GBs but Zn and Al were found to significantly embrittle the grain boundaries. The study also observed that GB cohesion improved marginally with increasing temperature. While quantitative observations could be made about the grain boundary, the study could not predict the role of alloying elements in the segregation of Zn near the surface of the weld [64].

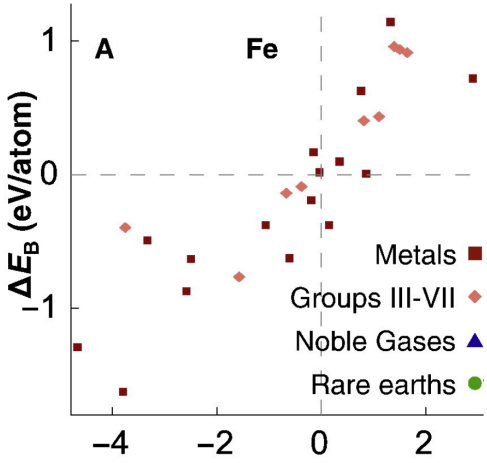


Figure 2.16: Embrittling potential of different alloying elements as a function of the difference in elemental cohesive energy for Fe [63]

The limitations of simulating LME using DFT based calculations is the high computational cost and limited scope of the atomic scale simulations. The difficulty in accurately measuring atomic parameters like interface and grain boundary energies also limits the possibility of experimentally validating these simulations. There is an evident lack of research that connects first-principles calculations on the origin of the driving force behind LME to experimental results at larger length scales. Despite efforts to link theoretical simulations with experimental results, the Fe-Zn system has received little attention in this regard. Different binary metal combinations, as discussed in Section 2.4.1, can have different embrittlement mechanisms. As a result, there is an urgent need to conduct a multi-scale investigation of LME in the Fe-Zn system that can effectively identify the atomistic mechanisms based on first-principles calculations and validate these observations with experimental studies and high resolution imaging.

2.10. Research gaps and Conclusion

Despite previous literature on LME in Zn-coated advanced high strength steels, several critical gaps remain in the understanding of the Fe-Zn system under RSW conditions. Existing grain boundary diffusion models are largely qualitative and lack direct experimental quantification of Zn diffusion ahead of cracks under realistic welding conditions. The relationship between weld time and the extent of Zn diffusion, particularly the distinction between bulk and grain boundary diffusion, has not been systematically studied. In addition, although Fe-Zn intermetallic phase formation during galvanizing is well described thermodynamically, its behaviour during RSW is not well established. The influence of welding parameters on crack initiation and crack propagation is also not clearly distinguished, particularly with respect to the role of hold time and subsequent cooling under applied electrode force. Finally, while LME cracks are known to propagate along grain boundaries, the crystallographic characteristics of

the boundaries that facilitate crack propagation, like grain misorientation across cracked interfaces, have not been quantitatively evaluated in Zn-coated TWIP steels under controlled welding conditions.

This thesis addresses these gaps through an experimental investigation of Zn-coated TWIP steel subjected to RSW, and validated by FEA simulations that predict thermo-mechanical behaviour during welding. First, Zn diffusion ahead of LME cracks is quantitatively measured as a function of weld time and crystallographic orientation, and compared with finite element simulations based on theoretical diffusion laws to provide a quantitative relationship between weld time and diffusion distance. Second, the evolution of Fe-Zn intermetallic phases at the steel-coating interface is characterized across a wide range of weld times and correlated with simulated temperature profiles to link FEA predictions with IM phase stability and their role in crack initiation. Third, the effect of hold time is studied, linking the weld temperature simulations with experimental observations of LME cracks in different regions of the weld. Finally, the crystallographic misorientation of grains adjacent to LME cracks is systematically analyzed to determine whether specific grain boundary character influences the LME crack path. Through the combined use of high-resolution microscopy and finite element modeling, this work establishes a quantitative framework linking welding parameters, diffusion behavior, interfacial phase stability, and microstructural characteristics to LME susceptibility in TWIP steels.

References

[1] J. E. Norkett, M. D. Dickey and V. M. Miller. 'A Review of Liquid Metal Embrittlement: Cracking Open the Disparate Mechanisms'. In: *Metallurgical and Materials Transactions A* 52.6 (1st June 2021), pp. 2158–2172. ISSN: 1543-1940. DOI: 10.1007/s11661-021-06256-y.

[2] R. Kuziak, R. Kawalla and S. Waengler. 'Advanced high strength steels for automotive industry'. In: *Archives of Civil and Mechanical Engineering* 8.2 (1st Jan. 2008), pp. 103–117. ISSN: 1644-9665. DOI: 10.1016/S1644-9665(12)60197-6.

[3] *Advanced High Strength Steels (AHSS) application guidelines*. International Iron & Steel Institute, 2005.

[4] D. Cooman. 'High Mn TWIP steel and medium Mn steel'. In: *Automotive Steels*. Woodhead Publishing, 1st Jan. 2017, pp. 317–385. DOI: 10.1016/B978-0-08-100638-2.00011-0.

[5] M. Tisza. *Development of Lightweight Steels for Automotive Applications*. Publication Title: Engineering Steels and High Entropy-Alloys. IntechOpen, 14th Feb. 2020. ISBN: 978-1-78985-948-5. DOI: 10.5772/intechopen.91024.

[6] T. B. Hilditch, T. de Souza and P. D. Hodgson. '2 - Properties and automotive applications of advanced high-strength steels (AHSS)'. In: *Welding and Joining of Advanced High Strength Steels (AHSS)*. Ed. by M. Shome and M. Tumuluru. Woodhead Publishing, 1st Jan. 2015, pp. 9–28. ISBN: 978-0-85709-436-0. DOI: 10.1016/B978-0-85709-436-0.00002-3.

[7] O. K. von Goldbeck. 'Fe—Zn Iron—Zinc'. In: *IRON—Binary Phase Diagrams*. Ed. by O. K. von Goldbeck. Berlin, Heidelberg: Springer, 1982, pp. 172–175. ISBN: 978-3-662-08024-5. DOI: 10.1007/978-3-662-08024-5_79.

[8] M. Krenn. *Characterization of Fe-Zn Intermetallic Compounds via Advanced Electron Microscopy / Author Martin Krenn*. 2025.

[9] K. Han, I. Ohnuma, K. Okuda and R. Kainuma. 'Experimental determination of phase diagram in the Zn-Fe binary system'. In: *Journal of Alloys and Compounds* 737 (15th Mar. 2018), pp. 490–504. ISSN: 0925-8388. DOI: 10.1016/j.jallcom.2017.11.320.

[10] H. Ertek Emre and R. Kaçar. 'Resistance Spot Weldability of Galvanize Coated and Uncoated TRIP Steels'. In: *Metals* 6.12 (Dec. 2016). Number: 12, p. 299. ISSN: 2075-4701. DOI: 10.3390/met6120299.

[11] H. Zhang and J. Senkara. *Resistance Welding: Fundamentals and Applications*. Boca Raton: CRC Press, 20th Dec. 2005. 444 pp. ISBN: 978-0-429-10159-5. DOI: 10.1201/b12507.

[12] M. Brijesh, M. Desai, M. P. Parmar and P. Student. *Optimization of process parameters for Resistance Spot Welding process of Austenitic SS 304 using Response Surface Method – A Review*. 2014.

[13] M. H. Razmpoosh, C. DiGiovanni, Y. N. Zhou and E. Biro. 'Pathway to understand liquid metal embrittlement (LME) in Fe-Zn couple: From fundamentals toward application'. In: *Progress in Materials Science* 121 (1st Aug. 2021), p. 100798. ISSN: 0079-6425. DOI: 10.1016/j.pmatsci.2021.100798.

[14] W. Jin, A. Lalachan, S. P. Murugan, C. Ji and Y.-d. Park. 'Effect of Process Parameters and Nugget Growth Rate on Liquid Metal Embrittlement (LME) Cracking in the Resistance Spot Welding of Zinc-Coated Steels'. In: *Journal of Welding and Joining* 40.6 (30th Dec. 2022), pp. 464–477. ISSN: 2466-2232, 2466-2100. DOI: 10.5781/JWJ.2022.40.6.2.

[15] H. Ueda, H. Fujimoto, S. Kikuchi, T. Okada, M. Fukumoto, K. Okamura, E. Nakayama and M. Yasuyama. 'Finite Element Simulation of Resistance Spot Welding Process for Automotive Steel'. In: 119 (2018).

[16] C. V. Nielsen, W. Zhang, L. M. Alves, N. Bay and P. A. F. Martins. *Modeling of Thermo-Electro-Mechanical Manufacturing Processes: Applications in Metal Forming and Resistance Welding*. SpringerBriefs in Applied Sciences and Technology. London: Springer, 2013. ISBN: 978-1-4471-4642-1 978-1-4471-4643-8. DOI: 10.1007/978-1-4471-4643-8.

[17] D. Bhattacharya. ‘Liquid metal embrittlement during resistance spot welding of Zn-coated high-strength steels’. In: *Materials Science and Technology* 34.15 (13th Oct. 2018). _eprint: https://doi.org/10.1080/02670836.2018.1461595, pp. 1809–1829. ISSN: 0267-0836. DOI: 10.1080/02670836.2018.1461595.

[18] R. Ashiri, M. Shamanian, H. R. Salimijazi, M. A. Haque, J.-H. Bae, C.-W. Ji, K.-G. Chin and Y.-D. Park. ‘Liquid metal embrittlement-free welds of Zn-coated twinning induced plasticity steels’. In: *Scripta Materialia* 114 (15th Mar. 2016), pp. 41–47. ISSN: 1359-6462. DOI: 10.1016/j.scriptamat.2015.11.027.

[19] P. Hancock and M. Ives. ‘The role of plastic deformation in liquid metal embrittlement’. In: *Canadian Metallurgical Quarterly* 10.3 (1st July 1971). _eprint: https://doi.org/10.1179/cmq.1971.10.3.207, pp. 207–211. ISSN: 0008-4433. DOI: 10.1179/cmq.1971.10.3.207.

[20] V. V. Popovich and I. G. Dmukhovskaya. ‘Rebinder effect in the fracture of Armco iron in liquid metals’. In: *Soviet materials science : a transl. of Fiziko-khimicheskaya mekhanika materialov / Academy of Sciences of the Ukrainian SSR* 14.4 (1st July 1978), pp. 365–370. ISSN: 1573-885X. DOI: 10.1007/BF01154711.

[21] S. P. Lynch. ‘Environmentally assisted cracking: Overview of evidence for an adsorption-induced localised-slip process’. In: *Acta Metallurgica* 36.10 (1st Oct. 1988), pp. 2639–2661. ISSN: 0001-6160. DOI: 10.1016/0001-6160(88)90113-7.

[22] H. Kang, L. Cho, C. Lee and B. C. De Cooman. ‘Zn Penetration in Liquid Metal Embrittled TWIP Steel’. In: *Metallurgical and Materials Transactions A* 47.6 (1st June 2016), pp. 2885–2905. ISSN: 1543-1940. DOI: 10.1007/s11661-016-3475-x.

[23] W. Rostoker, J. McCaughey and H. Markus. *Embrittlement by Liquid Metals*. Reinhold Publishing Corporation, 1960.

[24] N. S. Stoloff and T. L. Johnston. ‘Crack propagation in a liquid metal environment’. In: *Acta Metallurgica* 11.4 (1st Apr. 1963), pp. 251–256. ISSN: 0001-6160. DOI: 10.1016/0001-6160(63)90180-9.

[25] A. R. C. Westwood and M. H. Kamdar. ‘Concerning liquid metal embrittlement, particularly of zinc monocrystals by mercury’. In: *The Philosophical Magazine: A Journal of Theoretical Experimental and Applied Physics* 8.89 (1st May 1963). _eprint: https://doi.org/10.1080/14786436308213836, pp. 787–804. ISSN: 0031-8086. DOI: 10.1080/14786436308213836.

[26] E. Glickman. ‘Grain Boundary Grooving Accelerated by Local Plasticity as a Possible Mechanism of Liquid Metal Embrittlement’. In: *Interface Science* 11.4 (1st Oct. 2003), pp. 451–459. ISSN: 1573-2746. DOI: 10.1023/A:1026100112248.

[27] P. Gordon and H. H. An. ‘The mechanisms of crack initiation and crack propagation in metal-induced embrittlement of metals’. In: *Metallurgical Transactions A* 13.3 (1st Mar. 1982), pp. 457–472. ISSN: 1543-1940. DOI: 10.1007/BF02643354.

[28] L. Klinger and E. Rabkin. 'The effect of stress on grain boundary interdiffusion in a semi-infinite bicrystal'. In: *Acta Materialia* 55.14 (1st Aug. 2007), pp. 4689–4698. ISSN: 1359-6454. DOI: 10.1016/j.actamat.2007.04.039.

[29] W. Dong, K. Ding, H. Pan, M. Lei and Y. Gao. 'Effect of Welding Current on Liquid Metal Embrittlement of the Resistance Spot Welded Galvanized QP980 Advanced High-Strength Steel'. In: *TMS 2022 151st Annual Meeting & Exhibition Supplemental Proceedings*. The Minerals, Metals & Materials Series. Cham: Springer International Publishing, 2022, pp. 1254–1261. ISBN: 978-3-030-92381-5. DOI: 10.1007/978-3-030-92381-5_119.

[30] Z. Ling, T. Chen, L. Kong, M. Wang, H. Pan and M. Lei. 'Liquid Metal Embrittlement Cracking During Resistance Spot Welding of Galvanized Q&P980 Steel'. In: *Metallurgical and Materials Transactions A* 50.11 (1st Nov. 2019), pp. 5128–5142. ISSN: 1543-1940. DOI: 10.1007/s11661-019-05388-6.

[31] J. S. Dohie, J. Cahoon and W. Caley. 'The Grain-Boundary Diffusion of Zn in α-Fe'. In: *Journal of Phase Equilibria and Diffusion* 28.4 (1st Aug. 2007), pp. 322–327. ISSN: 1863-7345. DOI: 10.1007/s11669-007-9093-y.

[32] Y. Ikeda, H. C. Ni, A. Chakraborty, H. Ghassemi-Armaki, J. M. Zuo, R. D. Kamachali and R. Maaß. 'Segregation-induced grain-boundary precipitation during early stages of liquid-metal embrittlement of an advanced high-strength steel'. In: *Acta Materialia* 259 (15th Oct. 2023), p. 119243. ISSN: 1359-6454. DOI: 10.1016/j.actamat.2023.119243.

[33] M. H. Razmpoosh. 'Investigation of Liquid-Metal-Embrittlement Crack-path: Role of Grain Boundaries and Responsible Mechanism'. Accepted: 2020-07-24T17:23:26Z. PhD thesis. University of Waterloo, 24th July 2020.

[34] S. P. Murugan, V. Vijayan, C. Ji and Y. D. Park. 'Four types of LME cracks in RSW of Zn-coated AHSS'. In: *Weld J* 99.3 (2020), 75s–92s.

[35] A. Ghatei-Kalashami, M. S. Khan, F. Goodwin and Y. N. Zhou. 'Investigating the mechanism of zinc-induced liquid metal embrittlement crack initiation in austenitic microstructure'. In: *Journal of Materials Science* (17th Oct. 2023). ISSN: 1573-4803. DOI: 10.1007/s10853-023-08963-w.

[36] S. P. Murugan, J. Kim, J. Kim, Y. Wan, C. Lee, J. B. Jeon and Y.-D. Park. 'Role of liquid Zn and α-Fe(Zn) on liquid metal embrittlement of medium Mn steel: An ex-situ microstructural analysis of galvannealed coating during high temperature tensile test'. In: *Surface and Coatings Technology* 398 (25th Sept. 2020), p. 126069. ISSN: 0257-8972. DOI: 10.1016/j.surfcoat.2020.126069.

[37] S. Feliu Jr. and V. Barranco. 'XPS study of the surface chemistry of conventional hot-dip galvanised pure Zn, galvanneal and Zn-Al alloy coatings on steel'. In: *Acta Materialia* 51.18 (2003), pp. 5413–5424. DOI: 10.1016/S1359-6454(03)00408-7.

[38] H. Biber. 'Scanning auger microprobe study of hot-dipped regular-spangle galvanized steel: Part I. surface composition of As-produced sheet'. In: *Metallurgical Transactions A* 19.6 (1988), pp. 1603–1608. DOI: 10.1007/BF02674035.

[39] A. Rodnyansky, Y. Warburton and L. Hanke. ‘Segregation in hot-dipped galvanized steel’. In: *Surface and Interface Analysis* 29.3 (2000), pp. 215–220. DOI: 10.1002/(SICI)1096-9918(200003)29:3<215::AID-SIA703>3.0.CO;2-X.

[40] Y. Ikeda, R. Yuan, A. Chakraborty, H. Ghassemi-Armaki, J. M. Zuo and R. Maaß. ‘Early stages of liquid-metal embrittlement in an advanced high-strength steel’. In: *Materials Today Advances* 13 (1st Mar. 2022), p. 100196. ISSN: 2590-0498. DOI: 10.1016/j.mtadv.2021.100196.

[41] H. Lee, M. C. Jo, S. S. Sohn, S.-H. Kim, T. Song, S.-K. Kim, H. S. Kim, N. J. Kim and S. Lee. ‘Microstructural evolution of liquid metal embrittlement in resistance-spot-welded galvanized TWinning-Induced Plasticity (TWIP) steel sheets’. In: *Materials Characterization* 147 (1st Jan. 2019), pp. 233–241. ISSN: 1044-5803. DOI: 10.1016/j.matchar.2018.11.008.

[42] L. Cho, H. Kang, C. Lee and B. C. De Cooman. ‘Microstructure of liquid metal embrittlement cracks on Zn-coated 22MnB5 press-hardened steel’. In: *Scripta Materialia* 90-91 (1st Nov. 2014), pp. 25–28. ISSN: 1359-6462. DOI: 10.1016/j.scriptamat.2014.07.008.

[43] Z. Ling, M. Wang, L. Kong and K. Chen. ‘Towards an explanation of liquid metal embrittlement cracking in resistance spot welding of dissimilar steels’. In: *Materials & Design* 195 (1st Oct. 2020), p. 109055. ISSN: 0264-1275. DOI: 10.1016/j.matdes.2020.109055.

[44] G. Jung, I. S. Woo, D. W. Suh and S.-J. Kim. ‘Liquid Zn assisted embrittlement of advanced high strength steels with different microstructures’. In: *Metals and Materials International* 22.2 (1st Mar. 2016), pp. 187–195. ISSN: 2005-4149. DOI: 10.1007/s12540-016-5579-7.

[45] Y. G. Kim, I. J. Kim, J. S. Kim, Y. I. Chung and D. Y. Choi. ‘Evaluation of Surface Crack in Resistance Spot Welds of Zn-Coated Steel’. In: *MATERIALS TRANSACTIONS* 55.1 (2014), pp. 171–175. DOI: 10.2320/matertrans.M2013244.

[46] D.-Y. Choi, A. Sharma, S.-H. Uhm and J. P. Jung. ‘Liquid Metal Embrittlement of Resistance Spot Welded 1180 TRIP Steel: Effect of Electrode Force on Cracking Behavior’. In: *Metals and Materials International* 25.1 (1st Jan. 2019), pp. 219–228. ISSN: 2005-4149. DOI: 10.1007/s12540-018-0180-x.

[47] D. Bhattacharya, L. Cho, E. van der Aa, A. Pichler, N. Pottore, H. Ghassemi-Armaki, K. O. Findley and J. G. Speer. ‘Influence of the starting microstructure of an advanced high strength steel on the characteristics of Zn-Assisted liquid metal embrittlement’. In: *Materials Science and Engineering: A* 804 (15th Feb. 2021), p. 140391. ISSN: 0921-5093. DOI: 10.1016/j.msea.2020.140391.

[48] C. Béal. ‘Mechanical behaviour of a new automotive high manganese TWIP steel in the presence of liquid zinc’. Issue: 2011ISAL0029. Theses. INSA de Lyon, Mar. 2011.

[49] J. Kähkönen, D. T. Pierce, J. G. Speer, E. De Moor, G. A. Thomas, D. Coughlin, K. Clarke and A. Clarke. 'Quenched and Partitioned CMnSi Steels Containing 0.3 wt.% and 0.4 wt.% Carbon'. In: *JOM* 68.1 (1st Jan. 2016), pp. 210–214. ISSN: 1543-1851. DOI: 10.1007/s11837-015-1620-4.

[50] L. Chen, Y. Zhao and X. Qin. 'Some aspects of high manganese twinning-induced plasticity (TWIP) steel, a review'. In: *Acta Metallurgica Sinica (English Letters)* 26.1 (1st Feb. 2013), pp. 1–15. ISSN: 2194-1289. DOI: 10.1007/s40195-012-0501-x.

[51] M. H. Razmpoosh, A. Macwan, E. Biro, D. L. Chen, Y. Peng, F. Goodwin and Y. Zhou. 'Liquid metal embrittlement in laser beam welding of Zn-coated 22MnB5 steel'. In: *Materials & Design* 155 (5th Oct. 2018), pp. 375–383. ISSN: 0264-1275. DOI: 10.1016/j.matdes.2018.05.065.

[52] M. H. Razmpoosh, B. Langelier, E. Marzbanrad, H. S. Zurob, N. Zhou and E. Biro. 'Atomic-scale Investigation of Liquid-Metal-Embrittlement Crack-path: Revealing Mechanism and Role of Grain Boundary Chemistry'. In: *Acta Materialia* 204 (1st Feb. 2021), p. 116519. ISSN: 1359-6454. DOI: 10.1016/j.actamat.2020.116519.

[53] J. Barthelmie, A. Schram and V. Wesling. 'Liquid Metal Embrittlement in Resistance Spot Welding and Hot Tensile Tests of Surface-refined TWIP Steels'. In: *IOP Conference Series: Materials Science and Engineering* 118 (Mar. 2016), p. 012002. ISSN: 1757-899X. DOI: 10.1088/1757-899X/118/1/012002.

[54] M. G. Nicholas and C. F. Old. 'Liquid metal embrittlement'. In: *Journal of Materials Science* 14.1 (1st Jan. 1979), pp. 1–18. ISSN: 1573-4803. DOI: 10.1007/BF01028323.

[55] R. Sierlinger and M. Gruber. *A cracking food story about liquid metal embrittlement during spot welding of advanced high strength steels*. Voelstalpine GmBH, 2016.

[56] *AWS D8.9M:2012 Test Methods for Evaluating the Resistance Spot Welding Behavior of Automotive SheetSteel Materials*. American Welding Society, 2012.

[57] E. Wintjes, C. DiGiovanni, L. He, S. Bag, F. Goodwin, E. Biro and Y. Zhou. 'Effect of Multiple Pulse Resistance Spot Welding Schedules on Liquid Metal Embrittlement Severity'. In: *Journal of Manufacturing Science and Engineering* 141.10 (31st July 2019). ISSN: 1087-1357. DOI: 10.1115/1.4044099.

[58] C. DiGiovanni, S. Bag, C. Mehling, K. W. Choi, A. Macwan, E. Biro and N. Y. Zhou. 'Reduction in liquid metal embrittlement cracking using weld current ramping'. In: *Welding in the World* 63.6 (1st Nov. 2019), pp. 1583–1591. ISSN: 1878-6669. DOI: 10.1007/s40194-019-00790-5.

[59] S. P. Murugan, K. Mahmud, C. Ji, I. Jo and Y.-D. Park. 'Critical design parameters of the electrode for liquid metal embrittlement cracking in resistance spot welding'. In: *Welding in the World* 63.6 (1st Nov. 2019), pp. 1613–1632. ISSN: 1878-6669. DOI: 10.1007/s40194-019-00797-y.

[60] K.-D. Bauer, M. Todorova, K. Hingerl and J. Neugebauer. ‘A first principles investigation of zinc induced embrittlement at grain boundaries in bcc iron’. In: *Acta Materialia* 90 (15th May 2015), pp. 69–76. ISSN: 1359-6454. DOI: 10.1016/j.actamat.2015.02.018.

[61] Y.-J. Hu, Y. Wang, W. Y. Wang, K. A. Darling, L. J. Kecskes and Z.-K. Liu. ‘Solute effects on the Σ3 111[11-0] tilt grain boundary in BCC Fe: Grain boundary segregation, stability, and embrittlement’. In: *Computational Materials Science* 171 (1st Jan. 2020), p. 109271. ISSN: 0927-0256. DOI: 10.1016/j.commatsci.2019.109271.

[62] R. Schweinfest, A. T. Paxton and M. W. Finnis. ‘Bismuth embrittlement of copper is an atomic size effect’. In: *Nature* 432.7020 (Dec. 2004). Number: 7020, pp. 1008–1011. ISSN: 1476-4687. DOI: 10.1038/nature03198.

[63] M. A. Gibson and C. A. Schuh. ‘A survey of ab-initio calculations shows that segregation-induced grain boundary embrittlement is predicted by bond-breaking arguments’. In: *Scripta Materialia* 113 (1st Mar. 2016), pp. 55–58. ISSN: 1359-6462. DOI: 10.1016/j.scriptamat.2015.09.041.

[64] D. Scheiber, K. Prabitz, L. Romaner and W. Ecker. ‘The influence of alloying on Zn liquid metal embrittlement in steels’. In: *Acta Materialia* 195 (15th Aug. 2020), pp. 750–760. ISSN: 1359-6454. DOI: 10.1016/j.actamat.2020.06.001.

3

Materials and Methods

3.1. Introduction

This chapter describes the materials used in this study, the resistance spot welding procedure and the characterization techniques applied to investigate the microstructural and mechanical behavior of the material. First, the chemical composition and grade of the TWIP steel are presented. Next, the welding setup and procedures are detailed, including the equipment used, process parameters, and sample preparation. The characterization techniques used throughout this study are described. These include optical microscopy, scanning electron microscopy (SEM), electron backscatter diffraction (EBSD), X-ray diffraction (XRD), and scanning transmission electron microscopy (STEM). Finally, the finite element modelling framework for calculated temperature and stress distribution during RSW is described.

3.2. Materials

The investigated material was a sheet of LME susceptible galvanized, cold-rolled austenitic TWIP steel with a thickness of 1.23 mm and Zn coating thickness of approximately 12 µm. The TWIP steel was welded over two sheets of DX54 steel of thickness 1.5 mm and average Zn thickness of approximately 15 µm to form a heterogeneous triple stack weld, as shown in Figure 3.1. DX54 steel was used as backing sheets in a triple-layer weld configuration to increase heat input and promote LME crack formation [1]. The composition of the main alloying elements in the TWIP steel is presented below in Table 3.1. The composition of the main alloying elements in the DX54 sheet is given in Table 3.2.

Table 3.1: Composition of alloying elements in TWIP steel in wt%

Mn	Al	C	Ni
17.3	1.49	0.61	0.36

Table 3.2: Composition of alloying elements in DX54 steel in wt%

C	Mn	Al	P	Si
0.002	0.143	0.055	0.012	0.005

3.2.1. Welding Setup

Spot welds were produced on a 1000 MHz MFDC spot welding machine, using a constant current regulation. ISO5821 F1-16-20-6 CuCr1Zr electrodes were tip-dressed before use. The welding current, electrode force, squeeze time and hold time were kept constant, using the process parameters presented in Table 3.4, and were selected after internal optimization. The welding current was optimized to be the highest value that did not result in expulsion at a weld time of 1700 ms. In the weld time tests, all welding parameters were kept constant except for the weld time, which was varied from 300 ms to 1700 ms in increments of 200 ms. The samples obtained from these experiments were used to investigate several aspects of LME behavior. The study of crack initiation, including the analysis of the Fe-Zn interface and its evolution with increasing weld time, is presented in Chapter 4. The analysis of crack propagation, with emphasis on the influence of weld time, grain boundary misorientation, and grain boundary plane orientation on the crack path, is discussed in Chapter 5. Finally, the investigation of the crack tip region, focusing on Zn diffusion ahead of the crack tip and its correlation with diffusion-based models, is presented in Chapter 6.

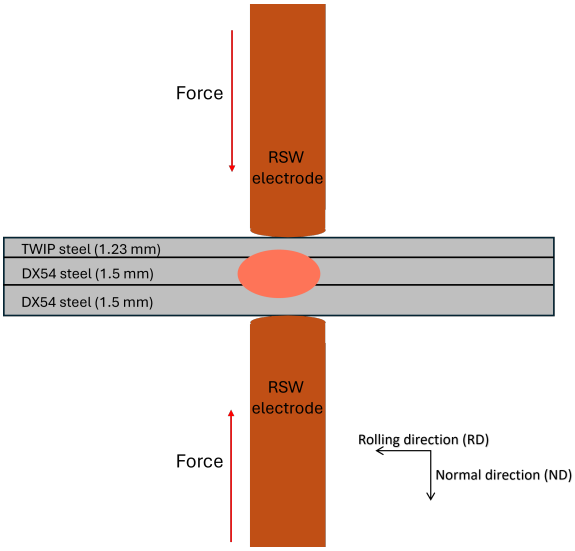


Figure 3.1: Schematic representation of the RSW setup showing the sample coordinate system

In the hold time tests, all welding parameters were kept constant except for the hold time, which was varied from 5 ms to 355 ms in increments of 50 ms. The purpose of these experiments was to evaluate the influence of welding parameters, other than weld

Table 3.3: RSW parameters for weld time study

Welding current (kA)	Welding force (kN)	Squeeze time (ms)	Hold time (ms)	Weld time (ms)
7.4	4.5	150	150	300, 500, 700, 900, 1100, 1300, 1500, 1700

time, on LME crack severity and crack location.

Table 3.4: RSW parameters for hold time study

Welding current (kA)	Welding force (kN)	Squeeze time (ms)	Weld time (ms)	Hold time (ms)
7.4	4.5	150	900	5, 55, 105, 155, 205, 255, 305, 355

3.3. Characterization

This section describes the characterisation techniques used throughout the thesis: optical microscopy (OM), scanning electron microscopy (SEM) with energy-dispersive spectroscopy (EDS) and electron backscatter diffraction (EBSD), X-ray diffraction (XRD), and scanning transmission electron microscopy with energy-dispersive spectroscopy (STEM). For each technique, the instrument, operating parameters, sample preparation procedure, and the specific microstructural information obtained are described.

3.3.1. Optical Microscopy

Identifying the location of LME cracks prior to cross-sectioning was not straightforward, as cracks were not always visible on the welded surface. Existing literature recommends removing the Zn coating with dilute HCl to expose surface cracks [2]; however, this also dissolves the Fe-Zn intermetallic phases that are of central interest in this thesis. A technique was therefore required that could reveal LME crack locations while leaving the Zn coating and underlying intermetallic layers intact. Liquid penetrant testing was used for this purpose, as shown in Figure 3.2. The procedure consisted of two steps. First, the weld surface was cleaned with isopropanol, after which a red penetrant dye was sprayed onto the weld and allowed to seep into any surface-breaking cracks. Excess dye was then removed from the surface using isopropanol, and the weld was dried with paper tissue, leaving dye retained only within the LME cracks. Second, a white developer layer was sprayed over the cleaned surface; this drew the retained dye back out of the cracks by capillary action, producing a clear red line against the white background at each crack location. Once the cracks were identified, the penetrant was

cleaned off using isopropanol and the weld was sectioned such that the cross-section plane passed through both the centre of the crack and the centre of the weld.

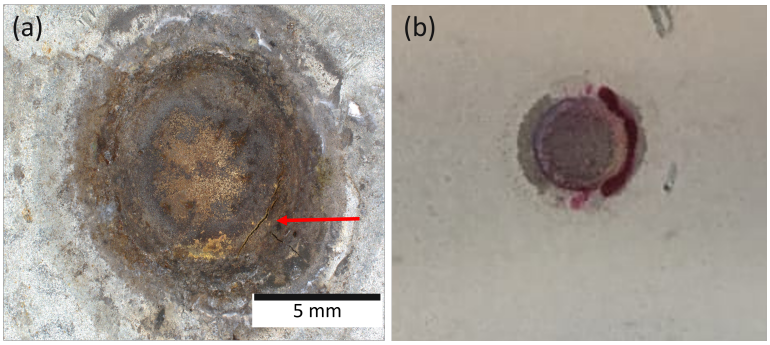


Figure 3.2: (a) Top view of RSW with the red arrow indicating LME cracks at the surface (b) Liquid penetrant testing to identify surface cracks

A VHX7000N optical microscope was used for cross-sectional analysis. Cross-sections were sectioned through the crack location, mounted, and ground with progressively finer grit sandpapers, followed by sequential polishing using 3 µm silica paste, 1 µm diamond paste, and OP-S liquid to obtain a smooth surface suitable for imaging. Optical microscopy was used to measure weld nugget geometry and to perform an initial assessment of LME crack location, number, depth, and width prior to higher-resolution characterisation.

3.3.2. Scanning Electron Microscopy

Scanning electron microscopy (SEM) was carried out using a JEOL IT800SHL equipped with a field emission gun, operating at 10 kV and a beam current of 3.2 nA. The system was also equipped with an Oxford Instruments® Maxim 100™ detector to perform Energy Dispersive Spectroscopy (EDS) and Electron Backscatter Diffraction (EBSD) for microstructural analysis. EBSD was used to determine phase distribution, grain orientation, and grain boundary character (including misorientation angle and coincidence site lattice character) at the Fe-Zn interface and across LME cracks. EDS elemental mapping and point/line scan analysis were used to determine the elemental distribution of Fe, Zn, Al, and Mn at the Fe-Zn interface and ahead of LME crack tips.

Phase identification by EBSD is reliable for determining the crystal structure, but is not always capable of distinguishing between different phases that share the same crystal structure, which is relevant to the Fe-Zn intermetallic system, where several phases can exhibit similar crystallographic behaviour [3]. To address this, SEM-EDS and STEM-EDS measurements were used along with EBSD for phase identification. The elemental ratios (Fe:Zn) measured at a given location by EDS were compared against the expected compositions of Fe-Zn intermetallic phases, determined from the base material composition and ThermoCalc equilibrium calculations [4]. The resulting phases was then input as the candidate phase list for EBSD indexing at that location.

3.3.3. X-Ray Diffraction

X-ray diffraction (XRD) was used to identify the phases present at the Fe-Zn interface, including Fe-Zn intermetallic compounds that could not be reliably distinguished from one another by EBSD alone due to their similar crystal structures. The specific phases identified and their significance to LME crack initiation are discussed in detail in Chapter 4. Measurements were performed on a Bruker D8 Discover diffractometer equipped with an Incoatec Microfocus Source (IμS) operated at 50 kV and 1000 μA, using Cu $K\alpha$ radiation. The beam was conditioned using Montel optics (ELM32) to produce a parallel beam, with a UBC collimator of 0.5 mm. Samples were mounted on a UMC 1516 sample stage, and diffracted intensity was recorded using an Eiger 500k detector with default detector settings. Measurement position and sample height were aligned for each scan using laser-video positioning. Scans were performed in continuous $\theta - 2\theta$ mode with a step size of 0.04° and a dwell time of 2 s per step. Resulting diffraction patterns were evaluated using Bruker DiffracSuite (version 7.3). Default detector settings were used in place of the Fe-specific filter settings normally recommended to suppress Fe Kα fluorescence. This choice was made so that any increase in background intensity with increasing 2θ could be interpreted: such an increase is consistent with either greater penetration depth at higher diffraction angles (exposing Fe/Mn fluorescence from the base metal beneath the Zn coating) or a genuinely higher Fe/Mn content within the surface layer itself. Measurements were taken at two characteristic locations on each weld cross-section: the weld centre, located directly beneath the electrode during RSW, and the weld shoulder, the region where Fe-Zn intermetallic phases predominantly form and where LME cracking is most commonly observed. The XRD patterns from these weld locations is shown in Figure 3.3 and discussed further in Chapter 4.

3.3.4. Scanning Tunnelling Electron Microscopy

Scanning transmission electron microscopy (STEM) was performed using a JEOL JEM-2200FS Cs-corrected microscope operated at 200 kV, equipped with a Schottky field-emission gun (FEG) and a JEOL JED-2300D EDX system. Electron transparent lamellae were prepared by the conventional lift-out method using a Helios G4 PFIB UXe xenon plasma focused ion beam (FIB). To protect the interface features from ion milling damage, a thin layer of platinum was deposited by beam-induced deposition prior to thinning. The parameters to extract STEM lamellae using FIB were obtained from Krenn et al [5]. Preparing FIB lamellae at the Fe-Zn interface was not straightforward, as the interface was not structurally stable enough to be thinned uniformly to electron transparency; initial attempts at uniform thinning resulted in lamella fracture and the formation of holes at the interface. To overcome this, an alternating thin/thick sectioning approach was adopted, in which the lamella was milled to electron transparent thickness only in narrow strips, leaving thicker, structurally supporting sections between them. Figure 3.4(a) illustrates how this lamella geometry was achieved on the sample holder. Figure 3.4(b) shows a top-down view of the cross-section, in which the lighter-contrast regions correspond to the thinner, more electron-transparent strips. This alternating thickness profile allowed accurate phase identification and reliable STEM-EDS elemental maps and line scans to be obtained across the Fe–Zn interface,

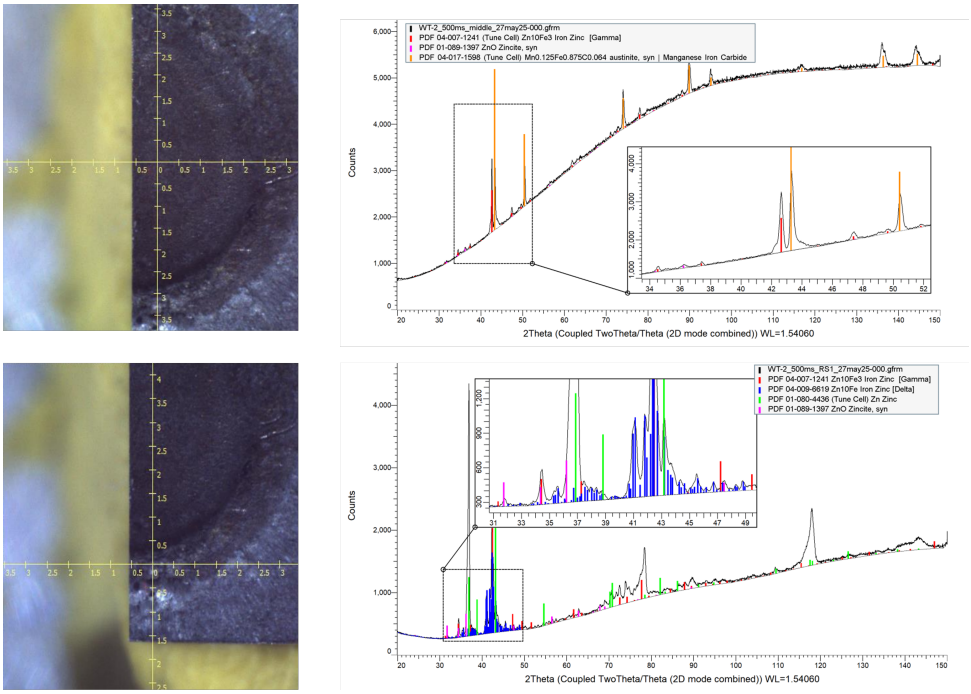


Figure 3.3: XRD analysis of weld cross section at the weld electrode region and weld shoulder region

while maintaining a lamella that remained structurally stable throughout analysis.

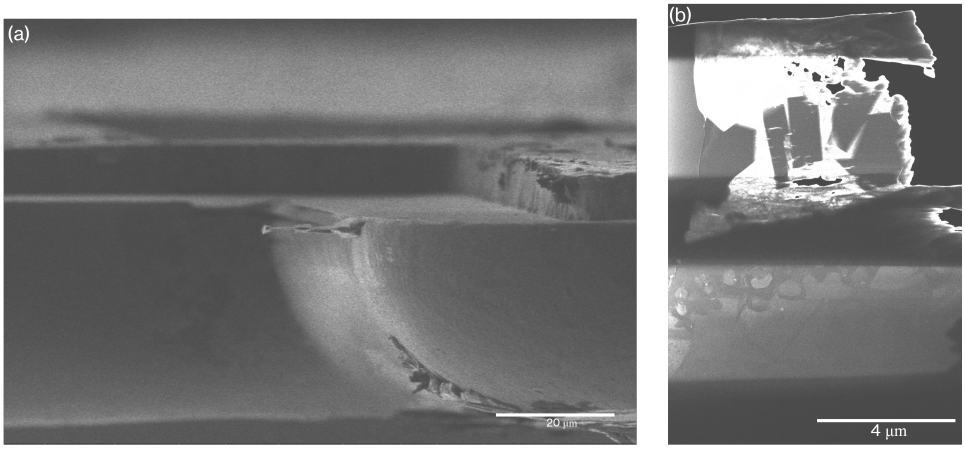


Figure 3.4: (a) Side view of FIB lamella of RSW cross-section with alternate thick and thin sections (b) Top view of STEM sample, where higher contrast regions are more electron transparent

3.4. Finite Element Analysis

FInite Element Analysis of the temperature and stress distributions in the RSW process was carried out using SORPAS [6]. At each time step, the input welding parameters is used to calculate the current density distribution through the stack, which in turn determines the resistive Joule heating generated at each interface and within the bulk material, based on the local electrical resistivity and contact resistance. This heat generation is used to solve for the resulting temperature distribution, accounting for heat conduction and temperature dependent material properties. The temperature then drives thermal expansion and softening of the sheets, which is solved together with the applied electrode force to determine how the contact area between the electrodes and sheets evolves and how the weld nugget forms.

3.4.1. Input variables

The simulation setup replicated the experimental RSW configuration, using the same material properties of the sheets, electrode geometry, coating conditions, and sheet thicknesses as the actual spot welds. The thermo-mechanical and electrical properties of the steel sheets were obtained from JMatPro [7]. The model used a dome-type electrode geometry matching the ISO5821 F1-16-20-6 CuCr1Zr electrodes used experimentally. The welding setup was defined in the same order as the triple-stack configuration, with the Zn coating included on each sheet surface as a discrete thin layer. Welding current, electrode force, squeeze time, weld time, and hold time were input to match the experimental parameters in Table 3.4, with constant current and force applied for the duration of each respective stage. A constant electrode coolant temperature of 25 °C was applied to simulate water cooling of the electrodes, and convective heat loss to ambient air was applied at all exposed sheet surfaces. Axisymmetry about the

electrode centreline was assumed, reducing the 3D weld geometry to 2D. Figure 3.5 shows the mesh used for the FEA model.

3.4.2. Model outputs

The primary outputs from the SORPAS simulations was the evolution of temperature and stress across the weld cross-section as a function of time. Temperature-vs-time plots were generated at fixed coordinates corresponding to the electrode region, weld shoulder region, and weld periphery region, matching the locations used for experimental characterisation in Chapter 7. Temperature at each location was used to assess Fe-Zn intermetallic phase stability (Chapter 4) and Zn availability (Chapter 6). The simulated weld nugget area was extracted to compare with the experimentally measured nugget area from optical microscopy cross-sections.

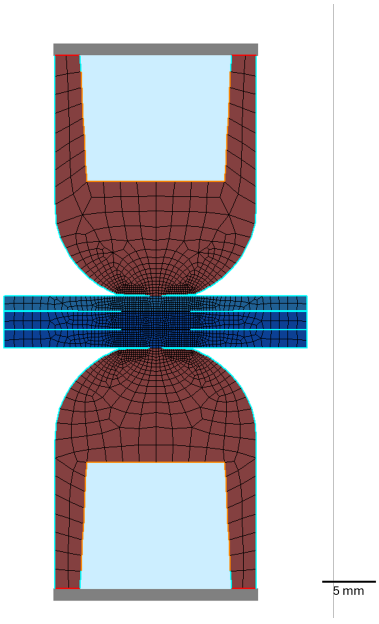


Figure 3.5: RSW FEA setup to calculate temperature distribution

4

LME crack initiation

This chapter studies how weld time influences the Fe-Zn interface and LME during RSW of electrogalvanized TWIP steel. Eight weld times ranging from 300 ms to 1700 ms were investigated under constant welding parameters. At 300 ms, the Zn coating remained intact with no intermetallic phases detected. At 500 ms, continuous layers of δ, Γ, and α-Fe(Zn) phases formed at the weld shoulder, confirmed by SEM-EDS, STEM-EDS, and EBSD, with α-Fe(Zn) showing Al enrichment and Mn depletion. At 700 ms, initial LME cracks appeared, accompanied by fragmented IM layers. For weld times between 900 ms and 1700 ms, crack width and depth increased significantly (from 21 µm to 490 µm), while IM phases were absent. Finite element analysis (FEA) simulations of temperature distribution correlated with experimental observations: IM formation occurred within the predicted stability range at 500 ms, became discontinuous at 700 ms, and disappeared at higher weld times as local temperatures exceeded 800 °C. These results demonstrate that IM formation precedes LME crack initiation and that prolonged weld time accelerates IM breakdown and crack propagation. The findings provide a mechanistic link between thermal conditions, interfacial reactions, and LME severity, offering guidance for optimizing RSW parameters in automotive applications.

4.1. Introduction

The context for this study, including the properties of TWIP steel, the role of zinc coatings, and the RSW process, is described in Chapter 2. As discussed there, Fe-Zn intermetallic phases at the weld interface play a central role in controlling the availability of liquid Zn and the onset of LME cracking. This chapter addresses that gap by examining how the Fe-Zn interface evolves across eight weld times from 300 ms to 1700 ms, and by linking the formation and breakdown of intermetallic phases to the onset of LME crack initiation.

LME mechanisms are not yet fully understood because crack initiation and propagation depend on the combined effects of stress, temperature, strain, and steel

Parts of this chapter have been published in Materials Science and Engineering A, Volume 972 (2026) [1]

microstructure. The local variations in stress, temperature, and microstructure across a weld further increase this complexity and result in different types of LME cracks forming in different regions of the weld [2]. Several theories have been suggested to explain the micro-mechanisms of LME, which depend on the specific solid/liquid metal pair. In the Fe-Zn system, stress-assisted GB diffusion is considered to be the dominant micro-mechanism. Most stress-assisted LME models are based on the Rehbinder effect, where liquid Zn penetrates GBs, lowers the steel surface energy, and causes embrittlement once a critical stress is reached [3–5].

Fe-Zn intermetallics (IM) play an important role at controlling LME at the interface of the steel substrate and Zn coating during RSW. When the Zn coating is subjected to temperatures above 427 °C under electrode force, it reacts with Fe to form IM compounds. The presence, thickness, and stability of these compounds determine how Zn is transported and how it remains available at the interface [6–10]. According to Murugan et al., at 700 °C the δ phase in the interface coating transforms into liquid Zn and Γ. Under these conditions, Γ is not stable with Fe, leading to the formation of a thin Zn-rich ferritic (α-Fe(Zn)) layer as Zn diffuses into Fe. Zn redistribution between α-Fe(Zn), Γ, and liquid Zn continuously re-establishes equilibrium, with Zn ultimately moving from the liquid phase through Γ into the steel [2]. Lee et al. reported that an Al-rich diffusion-inhibiting layer suppresses the formation of Fe-Zn IM at the Zn/steel interface, but this layer is destroyed during RSW due to heat and electrode stress. In cracked regions, fine α-Fe(Zn) particles appear on the steel surface and cracks propagate along austenite grain boundaries beneath this layer [11]. The crack area consists of Γ and α-Fe(Zn), showing that Zn infiltrates grain boundaries. The α-Fe(Zn) particles increase interfacial area and act as brittle phases, providing pathways for Zn infiltration and thereby accelerating LME, which becomes more severe with higher welding current [12]. Additionally, Al oxide zones at the Fe-Zn interface have been observed in previous studies. These oxide zones have a grain size that is independent of the relative concentrations of Al in the coating or the steel [13–15]. When these Al oxides and Fe-Zn IMs break down, Zn from the coating is available to diffuse into the GBs of the substrate. Ikeda et al. reported that in grain boundaries infiltrated with Zn but not yet cracked, a nanoscale Γ phase could be characterized. The observation of this phase indicates that strain heterogeneities are locally enhanced within the grain boundary network, and IM formation does not occur only after cracks develop and liquid Zn penetrates, but instead acts as a primary nanoscale factor that weakens grain boundaries and promotes crack initiation [16]. Although different Fe-Zn IM phases have been reported in studies where welding current was varied, the true sequence of events before, during, and after IM formation at the weld interface has not been examined in detail. In addition, while weld current has been widely studied, the effect of weld time has received little attention. Increasing the weld time not only increases the temperature in the nugget and shoulder (area adjacent to the electrode) regions but also influences the diffusion kinetics that govern IM formation and stability [17–20]. The effect of weld time on these processes is not well understood, leaving a gap in knowledge about the evolution of the Fe-Zn interface during RSW. In this study, eight welding conditions with WT from 300 ms to 1700 ms were studied, and the Fe-Zn interface evolution was characterized, while keeping all other welding parameters constant. The aim of this

chapter is to capture the evolution of the Fe-Zn interface at the weld shoulder: before IM formation, during IM formation, crack initiation and crack growth. The weld shoulder was selected because LME cracks consistently initiate in this region due to the availability of liquid Zn and favourable stress and temperature conditions[12]. Furthermore, an FEA simulation of the RSW process with the same materials, weld setup and parameters was run to validate the experimental observations and provide a complete picture of the Fe-Zn interface during RSW.

4.2. Materials and methods

The materials used in the RSW study, the RSW setup, parameters and the characterization tools used to analyse weld cross-sections are presented in Chapter 3. The FEA modelling framework in SORPAS used in this chapter to simulate temperature distributions is detailed in Section 3.4

4.3. Results

4.3.1. Microstructure characterisation of LME cracks

SEM analysis of the RSW joints (Figure 4.1) shows the evolution of the Fe-Zn interface with increasing weld time. At 300 ms, the Zn coating and interface remained intact, with no visible damage. At 500 ms, no LME cracks were observed, but the Zn layer showed local break-up and pore formation. At 700 ms, the first LME cracks appeared at the weld shoulder, consistent with Type B intergranular cracks. As the weld time was increased to 900 ms, 1100 ms, 1300 ms, 1500 ms and 1700 ms, the severity of embrittlement was observed to increase. LME severity was quantified by measuring the width and depth of cracks. Since Fe-Zn IM formation and crack initiation occur between 300 ms and 700 ms, most characterization in this study was focused on this weld time range.

The crack depth and width from all samples at each weld parameter were averaged. Both the average depth and width showed the same increasing trend with weld time, as shown in Figure 4.2. The average crack depth was 21 µm at 700 ms and increased to 32 µm at 900 ms. As the weld time increased to 1100 ms, the depth reached 60 µm. As the weld time was increased further, a larger increase was observed in crack depth, reaching 125 µm, 220 µm, and 490 µm at 1300 ms, 1500 ms, and 1700 ms, respectively. Similar trends were observed for crack width, with an average width of 2 µm at a weld time of 700 ms, and increasing to an average width of 57 µm at the highest weld time of 1700 ms. The Zn coating thickness was measured both on regions away from the weld and in the weld shoulder. The Zn coating away from the weld was measured to be between 5-10 µm, consistent with typical electrogalvanized coatings [21]. In the weld shoulder region, the coating thickness increased to 15-25 µm due to the accumulation of liquid Zn, because the electrode force drives molten Zn outward from the weld centre.

4.3.2. Fe-Zn interface characterization

In this section, welds produced at 300 ms, 500 ms and 700 ms are studied in further detail. The characterization focuses on the weld shoulder region, and results from SEM,

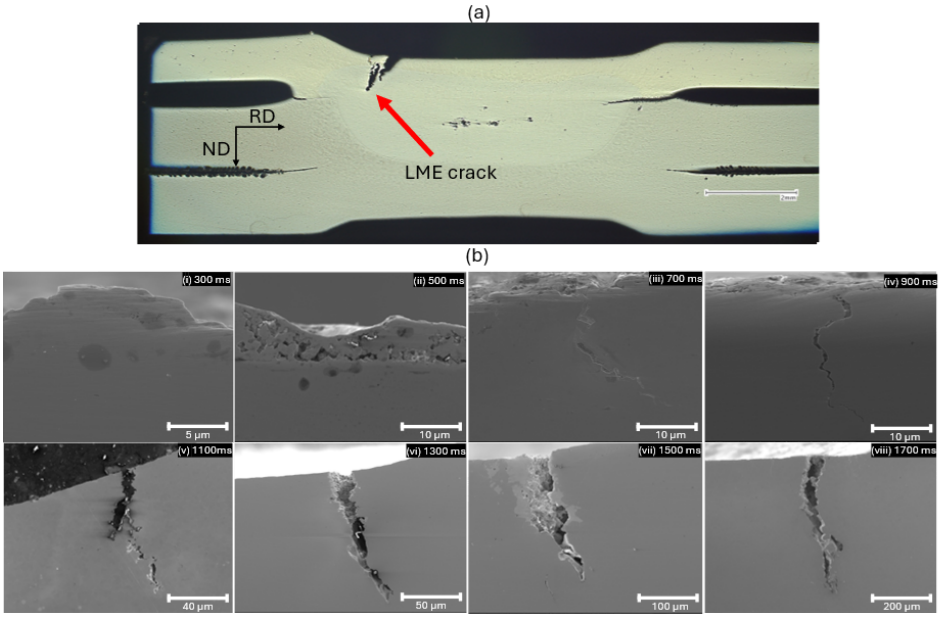


Figure 4.1: (a) Representative optical micrograph of weld cross-section at WT=1700 ms showing an LME crack (b) SEM micrographs of RSW shoulder region at weld time of (i) 300 ms (ii) 500 ms (iii) 700 ms (iv) 900 ms (v) 1100 ms (vi) 1300 ms (vii) 1500 ms (viii) 1700 ms

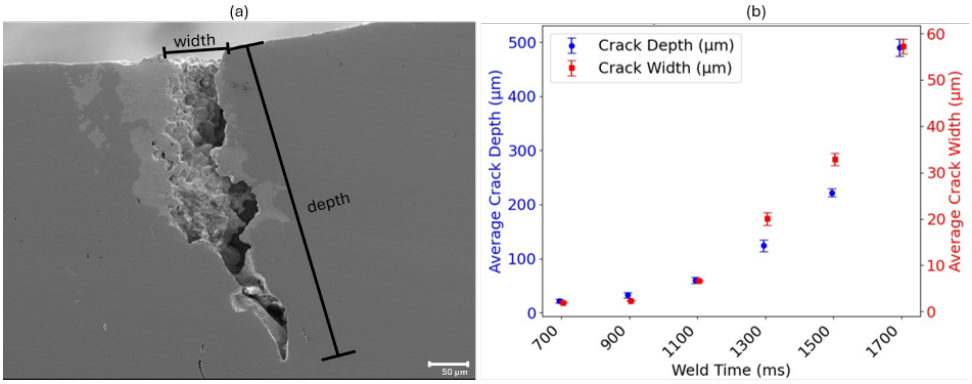


Figure 4.2: (a) Schematic diagram for crack dimension measurement (b) Average LME crack depth and crack width at different weld times

EDS and EBSD are presented. These characterization techniques are used to identify the phases present at the Fe-Zn interface and to describe the elemental distribution in and around the interface at different weld times. From the composition of the steel

used, the Fe-Zn phase diagram as well as other studies on the Fe-Zn interface [22], the possible phases present in the interface is listed in Table 4.1.

Table 4.1: Possible phases present in Fe-Zn interface [22, 23]

Phase	**Formula**	**Crystal structure**	**Temperature range (□)**
α-Fe	α-Fe(Zn)	BCC	<782
Γ	Fe_3Zn_{10}	BCC	530-665
$Γ_1$	Fe_5Zn_{21}	FCC	540-665
δ	$FeZn_{10}$	HCP	530-782
ζ	$FeZn_{13}$	monoclinic	430-530

WT = 300 ms

At a weld time of 300 ms, the electrogalvanized Zn coating remains intact on the TWIP steel. The steel retains its fully austenitic structure, and no Fe-Zn IM phases can be identified by EBSD, as shown in Figure 4.3. Analysis along the weld shoulder shows no evidence of LME cracks. The Zn coating is unindexed by EBSD and appears black in colour. From the EDS elemental map, three distinct regions can be identified at the interface, as shown in Figure 4.3. The average weight percentage of various alloying elements in these regions is measured (Table 4.2). The uppermost region corresponds to the Zn coating, below which there is an intermediate interface layer that is Fe rich and shows enrichment in Al and depletion of Mn relative to the bulk TWIP steel substrate, which forms the bottommost layer.

Table 4.2: Average weight percentage of different elements in the coating, interface and steel substrate

	Fe (wt %)	Zn (wt %)	Al (wt %)	Mn (wt %)
Coating	12.93	78.34	0.23	0.18
Interface	60.91	24.97	4.15	8.37
Steel	75.21	0.47	1.86	17.25

WT = 500 ms

At a weld time of 500 ms, no LME crack was observed in the RSW samples. However, multiple IM phases are observed in the weld shoulder region. These phases appear as distinct layers at the Fe-Zn interface. To characterize the phases and their distribution, XRD, SEM-EDS, EBSD and STEM-EDS analyses were performed on this sample. The analysis was performed at the Fe-Zn interface at the weld shoulder region, shown in Figure 4.4.

XRD

XRD analysis was carried out in the weld shoulder region to identify the phases present. The XRD spectrum is shown in Figure 4.5 with the detected phases labelled. Zn, ZnO, δ

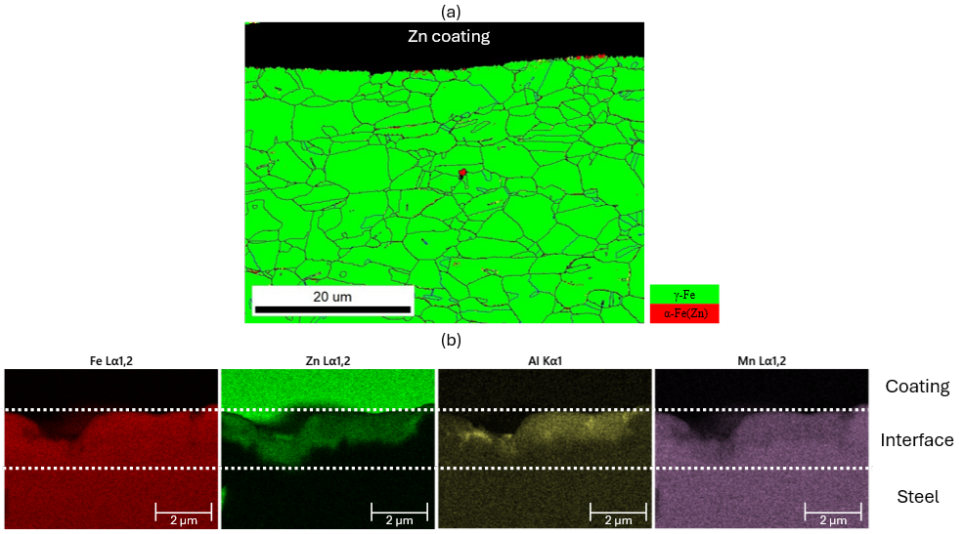


Figure 4.3: Characterization of RSW sample at WT = 300 ms showing (a) EBSD phase map of Fe-Zn interface (b) EDS elemental map of Fe, Zn, Mn and Al showing the different layers of the Fe-Zn interface

and Γ were identified from the diffraction peaks. Notably, α-Fe(Zn) and austenite could not be identified by XRD. Due to the similar atomic configurations, Γ and Γ_1 IM phases are not easily distinguishable [23].

EBSD

Figure 4.6(a) and (b) show the EBSD phase map of the Fe-Zn interface at two different magnifications of 1500x and 6000x respectively, and indicates the formation of layered Fe-Zn IMs. The δ phase is observed at the top, followed by a layer of Γ. Below this, a continuous chain of α-Fe(Zn) is present at the interface, with austenitic Fe underneath. The α-Fe chain is interspersed with the Γ phase and exhibits an elongated morphology. Although EBSD phase identification characterizes the intermediate layer as α-Fe(Zn), the results need further validation due to potential misindexation during EBSD. Thus, SEM-EDS and STEM were used to validate EBSD characterization.

EDS

Elemental mapping and point composition analysis were done to study the distribution of alloying elements at the Fe-Zn interface, as shown in Figure 4.7. The elemental maps show Zn-rich IM layers, below which an Fe-rich, Zn-poor phase is interspersed within a Zn-rich, Fe-poor phase. The Fe-rich phase, identified as α-Fe(Zn) by EBSD, is enriched in Al, with Al concentration higher than in the surrounding steel or IM layers. The same phase also shows Mn depletion compared to the steel substrate, which is confirmed by

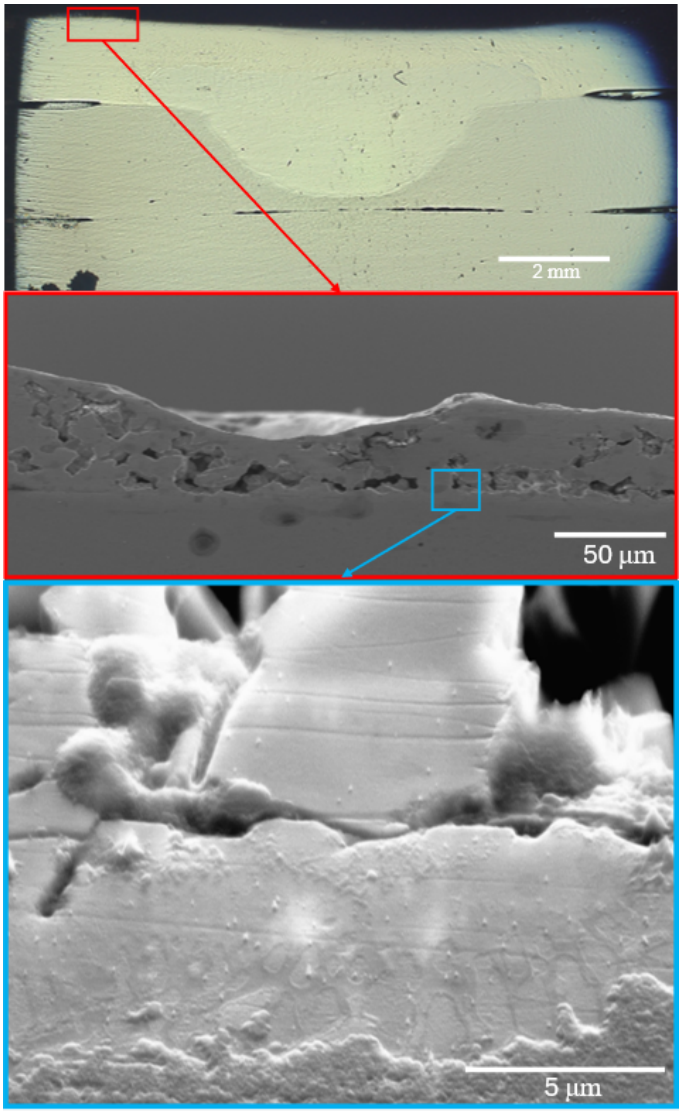


Figure 4.4: Analysis area of RSW shoulder Fe-Zn interface for characterization

point analysis. The Fe-rich phase has a composition of 72.06 wt% Fe, 18.92 wt% Zn, 5.91 wt% Al and 2.11 wt% Mn. The region above this phase contains 73.18 wt% Zn, 20.43 wt% Fe, 0.24 wt% Al and 4.67 wt% Mn. Based on composition and phase identification, the Fe-rich phase is most consistent with α-Fe(Zn), while the phase above corresponds to the Γ phase.

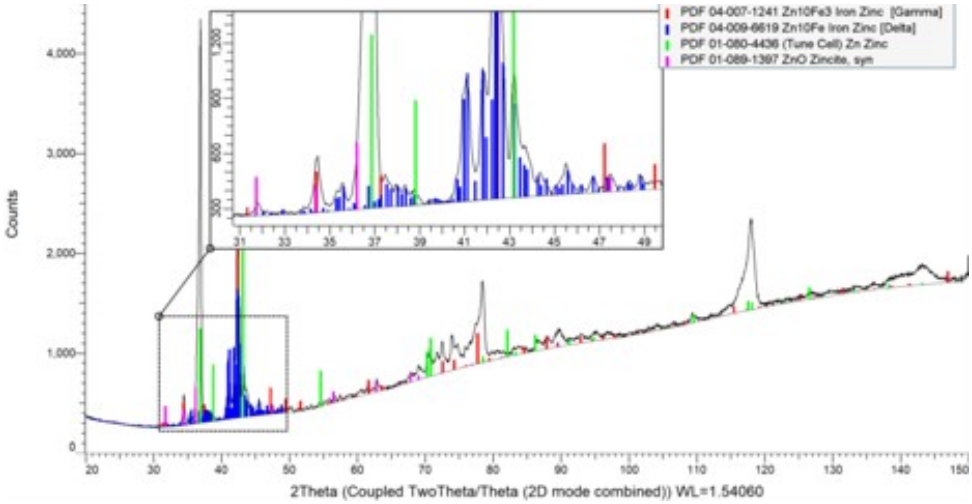


Figure 4.5: XRD spectrum from weld shoulder of RSW sample at WT = 500 ms

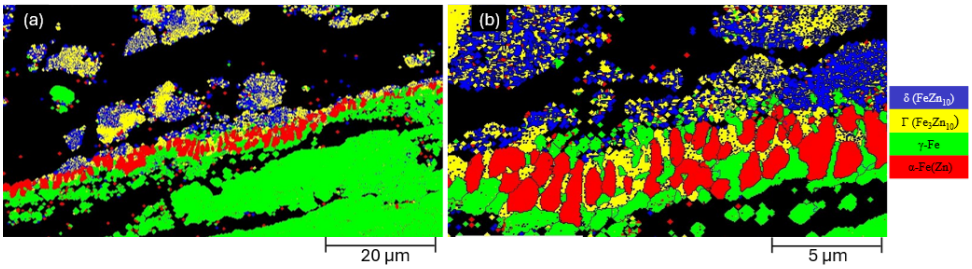


Figure 4.6: EBSD phase map of RSW sample at WT = 500 ms at a magnification of (a) 1500x (b) 6000x

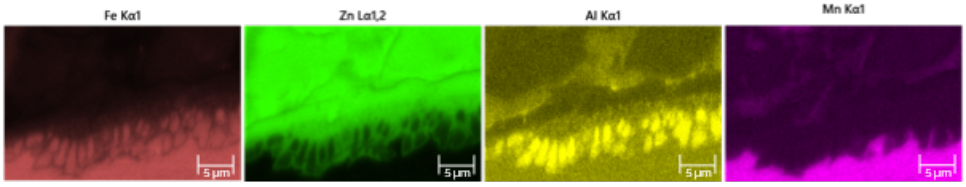
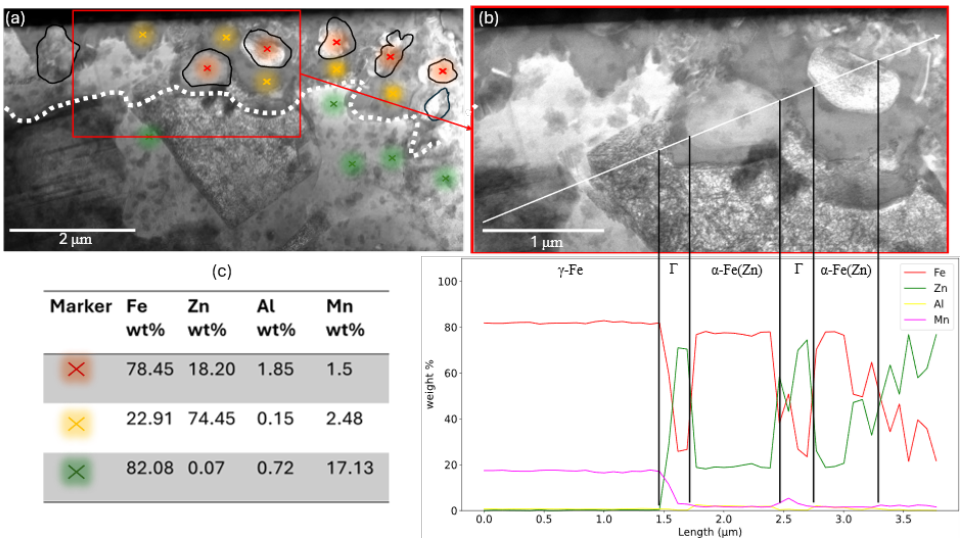


Figure 4.7: SEM-EDS map of RSW Fe-Zn interface at WT = 500 ms of Fe, Zn, Mn and Al

STEM

STEM analysis was carried out on a lamella from the Fe-Zn interface. The objective of this analysis was to confirm the identity of the BCC phase that EBSD had suggested

asα-Fe. STEM-EDS line scans and point elemental analysis were performed to determine the composition of the different phase regions, as shown in Figure 4.8.



Marker	Fe wt%	Zn wt%	Al wt%	Mn wt%
×	78.45	18.20	1.85	1.5
×	22.91	74.45	0.15	2.48
×	82.08	0.07	0.72	17.13

Figure 4.8: STEM-EDS analysis of RSW sample at WT = 500 ms showing (a) point analysis to measure elemental distribution of different phases, (b) line scan of Fe-Zn IM phases, (c) weight percentages of various alloying elements from point analysis

The STEM-EDS results validate the SEM-EDS observations, showing that a Zn-rich α-Fe layer forms between the austenite and the Fe-Zn IM layers, as shown in Figure 4.9. The Fe and Zn weight percentage measured in these grains corresponds stoichiometrically to α-Fe(Zn) [12]. Similarly, the phase surrounding these grains is characterized to be Γ, which forms an uneven interface with the underlying austenitic steel. STEM-EDS elemental mapping further confirms these results, showing a Zn-rich interface containing grains that are relatively poorer in Zn, Al and Mn and enriched in Fe.

WT = 700 ms

Characterization of the RSW samples at WT = 700 ms were performed using EDS and EBSD, as shown in Figure 4.10. A narrow LME crack is observed at the edge of the weld shoulder. At the crack opening, no IMs or α-Fe(Zn) grains were present. Unlike the continuous layered structure observed at 500 ms, these phases appear discontinuous and fragmented in the 700 ms sample. These results indicate that 700 ms represents the transition stage, where IM layers begin to break down and LME crack formation is observed.

WT = 900 ms to 1700 ms

Figure 4.12 shows the EBSD phase maps obtained from RSW samples with weld times between 900 ms and 1700 ms. LME cracks are present in all samples within this range.

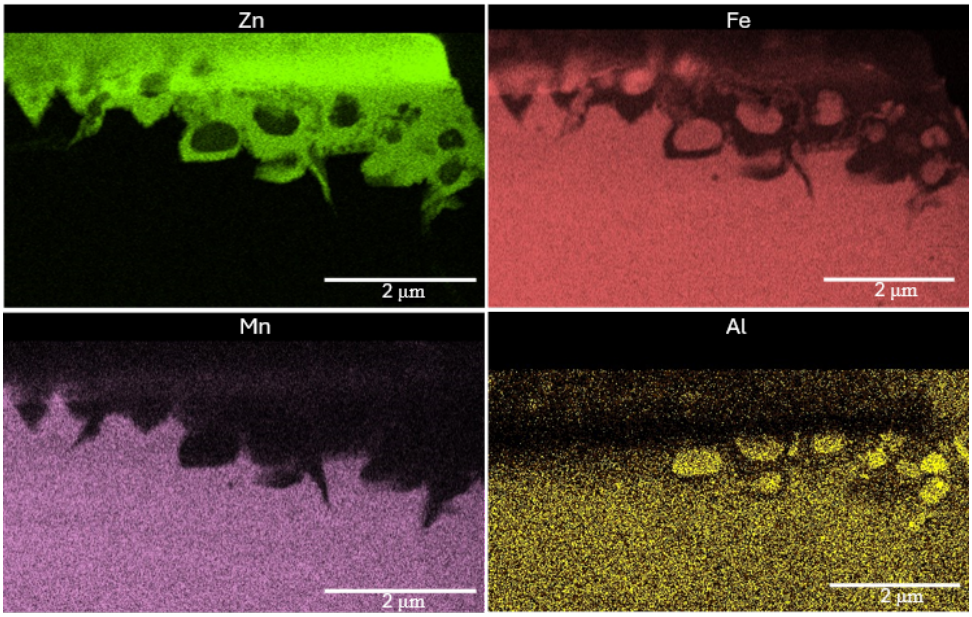


Figure 4.9: STEM-EDS map of RSW Fe-Zn interface at WT = 500 ms

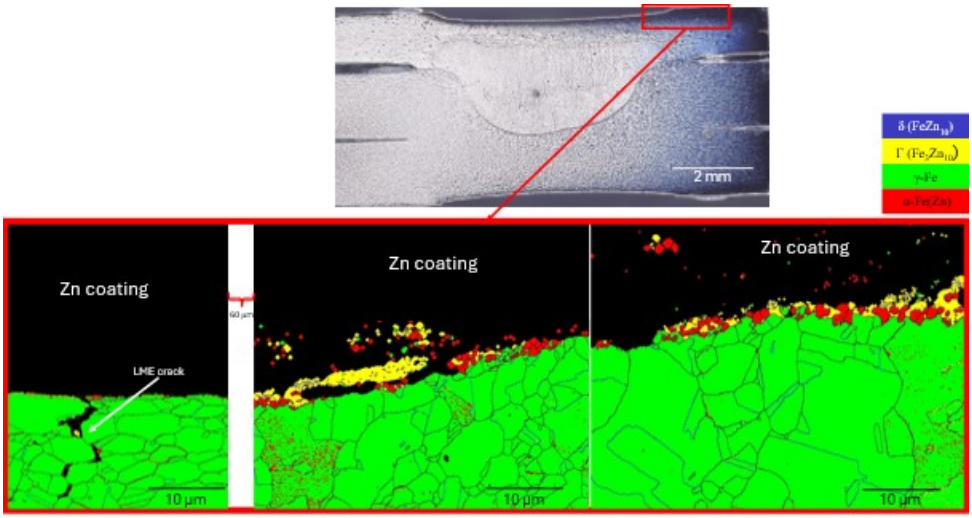


Figure 4.10: EBSD phase map of RSW weld shoulder region at WT = 700 ms showing LME crack and IM formation

No Fe-Zn IM phases were characterized at any of the RSW samples. As shown in Figure 4.2, both the depth and width of the LME cracks increase with increasing weld time. At a weld time of 900 ms to 1300 ms, the crack initiates in the shoulder region and all the characterized grains are predominantly austenitic. At weld times of 1500 ms and 1700 ms, the lower part of the crack extends into the weld fusion zone, which is indexed as ferritic. While the crack dynamics and growth in the weld fusion zone are affected by the welding conditions, it is not the focus of this study.

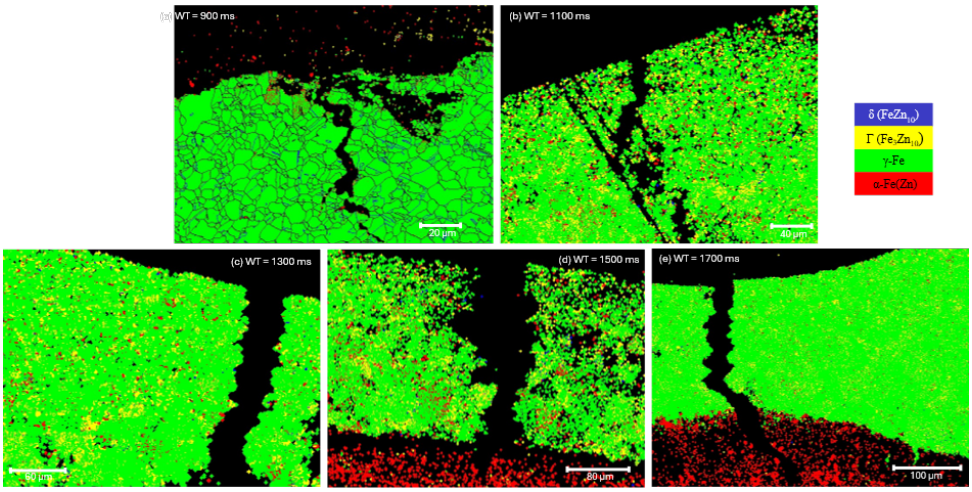


Figure 4.11: EBSD phase maps of RSW samples at weld times of (a) 900 ms (b) 1100 ms (c) 1300 ms (d) 1500 ms (e) 1700 ms

4.3.3. Comparing FEA and experimental observations

Comparison of weld nugget geometry

To validate the accuracy of the FEA model, the weld nugget areas from the RSW simulation and the experimentally obtained weld cross-sections were compared at weld times of 500 ms, 700 ms, and 900 ms. Figure 4.12 shows the comparison between the experimental cross-sections and the simulated weld nuggets, and Table 4.3 summarizes the calculated nugget areas.

At 500 ms, the simulation predicted incomplete fusion between the two DX54 sheets, which was consistent with the experimental cross-section. The difference between simulated and experimental nugget areas was 5.91%. At 700 ms, the model predicted a larger weld nugget extending into the bottom sheet, matching the micrograph, with a 4.87% difference in area. At 900 ms, the same trend was observed, with the nugget fully developed and a smaller difference of 1.69% between simulation and experiment.

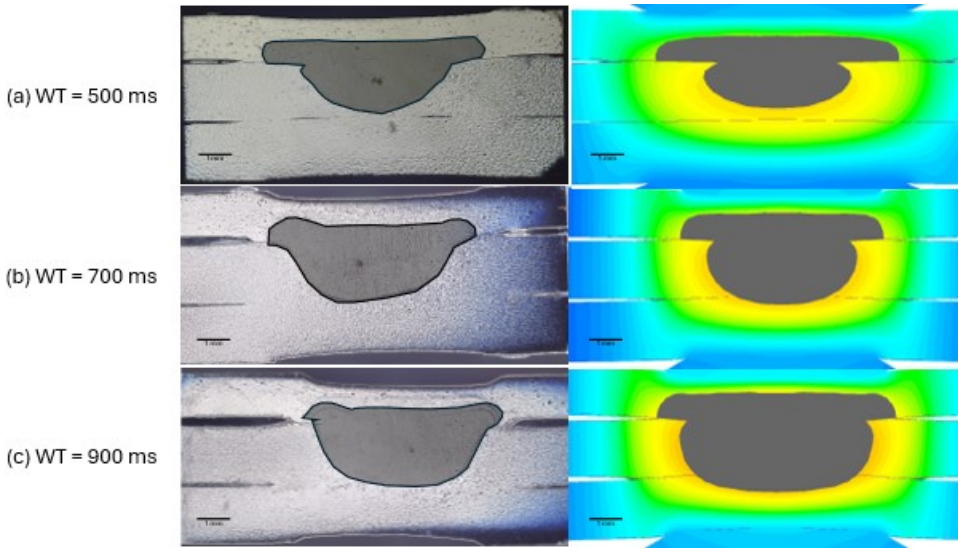


Figure 4.12: Comparison of weld nugget geometry between RSW cross-sections and FEA simulations at weld times of (a) 500 ms (b) 700 ms (c) 900 ms

Table 4.3: Comparison of weld nugget area between RSW cross-section and FEA simulation

Average weld nugget area from RSW sample (mm^2)	Weld nugget area from FEA simulation (mm^2)
6.52 ± 0.23	6.93
9.57 ± 0.38	10.06
10.43 ± 0.42	10.61

Temperature distribution analysis

Figure 4.13 shows the temperature distribution predicted by the FEA simulation across the weld cross-sections at weld times of 500 ms, 700 ms, and 900 ms, corresponding to the end of the weld time stage when the peak temperature is reached. Four points, A, B, C, and D, located between 3.4 mm and 5 mm from the weld centre were selected for detailed temperature analysis. These positions correspond to the weld shoulder region, where Fe-Zn IMs were experimentally observed. Figure 15 also shows the temperature evolution at these points throughout the weld cycle.

At a weld time of 500 ms, the simulation shows that location D reaches a peak temperature of 470 °C. Locations C reaches a peak temperature of 645 °C and B reaches 816 °C. The peak temperature at Location A is 882 °C. At a weld time of 700 ms, location D reaches at peak temperature of 587°C. Locations C and B reach peak temperatures of 771 °C and 930 °C, respectively, while location A reaches 980 °C. Locations A and B reach a temperature above the boiling point of Zn. At a weld time of 900 ms, locations A, B, C and reach peak temperatures of 1067 °C, 1015 °C, 875 °C

and 675 °C respectively.

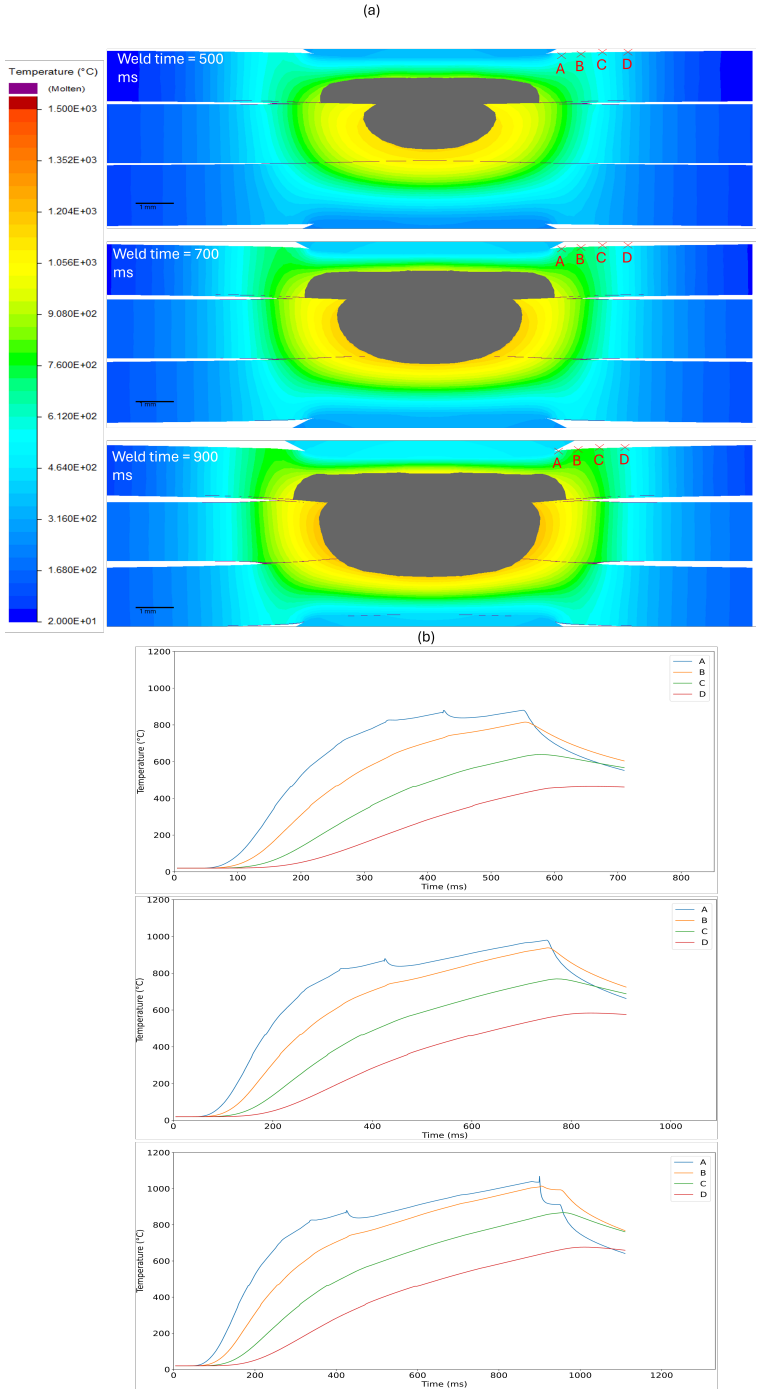


Figure 4.13: Temperature distribution during RSW at weld times of 500ms, 700ms and 900 ms

4.4. Discussion

In this study, all welding parameters were kept constant except for weld time to characterize the development of the Fe-Zn interface. Increasing weld time increases the temperature in the nugget and shoulder regions, which directly affects the formation of IMs, infiltration of Zn in the steel GBs, and the initiation and propagation of LME cracks [17, 19]. An FEA model was developed on SORPAS to replicate RSW conditions. The FEA model accurately reproduces RSW conditions based on the comparison between the simulated and experimental weld nugget areas and nugget geometry. The differences in calculated nugget areas could be a result of loss of material from the cross-section during sample preparation or cutting. When the temperature in the weld region exceeds 419 °C, Zn begins to melt. The applied electrode force pushes liquid Zn from the electrode-steel interface onto the weld shoulder [24]. At the lowest weld time of 300 ms, the Fe-Zn interface at the weld shoulder does not form IM layers. Some Al segregation at the interface is observed. Although not characterized by EBSD, this Al rich region could be a remnant of the Al oxide layer that is observed to form at the Fe-Zn interface during hot dip galvanisation [13–15]. At a weld time of 500 ms, the temperature at the weld shoulder region (locations C and D from Figure 4.13) are between 470 °C to 650 °C, as calculated by the FEA model. Locations A and B exceeds 800 °C, above the stability limit for IMs. According to the Fe-Zn phase diagram, δ transforms to Γ and liquid Zn at 660 °C and Γ becomes α and liquid Zn at 782 °C [23, 25]. Figure 4.14 shows the ternary phase diagram of Fe-Zn-Mn and the possible IM phases that can form. These peritectic reactions results in the layers of IM phases observed at the Fe-Zn interface at the weld shoulder. SEM-EDS, STEM, and EBSD characterization of the 500 ms sample showed the formation of δ, $\Gamma/\Gamma1$, and α-Fe(Zn) layers above the austenitic steel. The identification of α-Fe(Zn) within the Γ matrix has been debated, with different studies reaching different conclusions depending on the methods used. Bertolo et al. reported a similar interfacial phase but characterized it as Γ from spherical indexation analysis of EBSD data and the absence of an α-Fe peak in XRD spectra [26]. In contrast, the present results from SEM-EDS and STEM-EDS show compositions with Fe contents greater than 75 wt%, consistent with α-Fe(Zn). EBSD also indicated a BCC structure, further supporting this identification. The absence of α-Fe(Zn) peaks in XRD performed in the current study could be due to the limited penetration depth of X-rays in the weld shoulder, where excess Zn solidifies after being displaced from the electrode-steel interface. The calculated thickness of the Zn layer in the weld shoulder is between 15-25 µm, which is higher than the penetration depth of the characterization technique, which is roughly 10 µm [27].

Several other studies have also reported α-Fe(Zn) forming within a Γ matrix immediately above the austenitic steel, in agreement with the Fe-Zn phase diagram [29], which permits α-Fe(Zn) as a stable phase under these conditions [12, 16, 23, 30]. EDS analysis also indicates that α-Fe(Zn) is enriched in Al compared to both the surrounding IMs and the bulk TWIP steel, while also showing a depletion in Mn. This partitioning behaviour suggests that Al is preferentially stabilized in the Fe-rich α-Fe(Zn) phase. According to Lee et al., Al oxide layer typically forms between the Zn coating and the steel, acting as a barrier for Zn penetration. When welding temperatures and stresses cause the Al oxide barrier to break down, IMs can form, but the Al originating

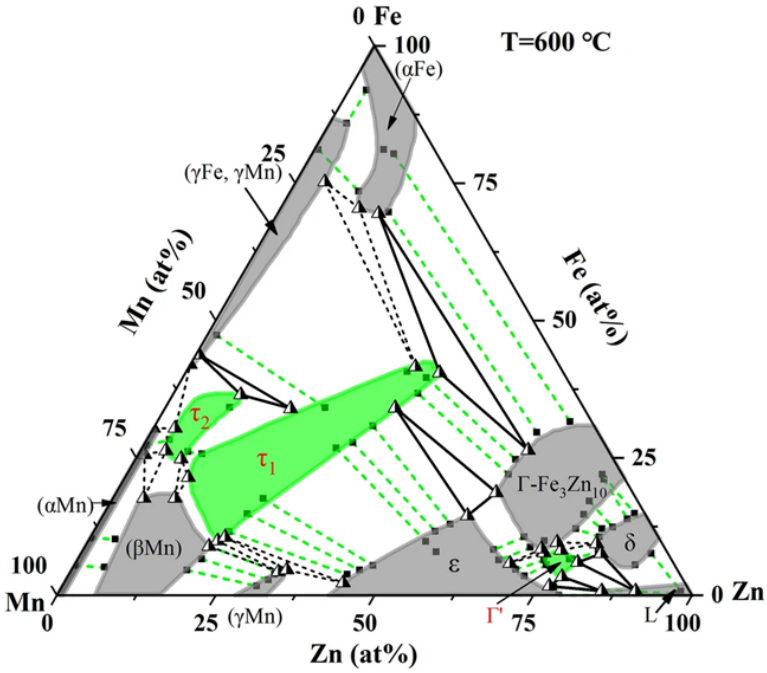


Figure 4.14: Fe-Zn-Mn phase diagram at 600 °C [28]

from the oxide layer does not diffuse far due to limited mobility [30]. Al is a ferrite stabilizer [31], and Mn in an austenite stabilizer [32]. During RSW, in regions where Al weight percentage is higher (1.85 wt% compared to 0.72 wt%) and Mn concentration is lower (2.48 wt% compared to 17 wt%) than in the bulk TWIP steel, it becomes thermodynamically favourable for α-Fe(Zn) to form. This explains the observed Al enrichment and Mn depletion in α-Fe(Zn), as well as its stability at the Fe-Zn interface under welding conditions. It is also important to note that the EDS line scan profiles of Fe and Zn at the interface collected in the present study closely matched the results by other studies discussed in this section.

At WT = 700 ms, LME cracks initiate at the weld shoulder, but IMs are not present near the crack opening. Unlike the continuous chain of IM phases observed at WT = 500 ms, these IM layers at WT = 700 ms are broken and discontinuous. At a weld time of 700 ms, Figure 4.13 from the FEA simulation shows the temperature at locations A and B exceeds the boiling temperature of Zn. Location C reaches 771°C which is almost at the maximum temperature of α-Fe(Zn) formation. This predicts a partially formed and discontinuous IM layer, consistent with the experimental observation of fragmented Fe-Zn layers shown in Figure 4.6. At a weld time of 900 ms, locations A, B, and C all reach temperatures above 800 °C, too high for Fe-Zn IM stability. These conditions correspond to the absence of IMs and the appearance of LME cracks in the experimental samples. Crack openings provide escape paths for liquid Zn from the

weld shoulder [6, 8, 33]. As a result, once cracks have initiated, the conditions are no longer favourable for stable intermetallic layers to form. At weld times between 900 ms and 1700 ms, results show that local temperatures at the weld shoulder exceed the stability range of Fe-Zn IMs. EBSD analysis confirms that no Fe-Zn IM phases are present at these weld times, while LME cracks are observed in all samples. The absence of δ, Γ, Γ_1 and α-Fe(Zn) phases indicate that the shoulder region experiences temperatures above 800 °C - above the upper stability limit for Fe-Zn IMs. The LME cracks at weld times of 1500 ms and 1700 ms grow into the martensitic weld fusion zone. The progressive increase in crack depth and width from 900 ms to 1700 ms indicates that continued heating enhances liquid Zn penetration along GBs under tensile stress. This suggests that once IMs break down, liquid Zn can penetrate through the austenitic GBs and diffuse through the steel, propagating the LME crack [34].

4.5. Conclusions

This chapter investigated the evolution of the Fe-Zn interface during RSW of electrogalvanized TWIP steel, with weld times ranging from 300 ms to 1700 ms, while all other parameters were held constant. The sequence of IM formation, their stability, and their relation to the onset of LME were identified through combined experimental observations and FEA simulations.

At 300 ms, the Zn coating remained intact and no IMs were observed. At 500 ms, δ, Γ, and α-Fe(Zn) phases formed as continuous layers at the weld shoulder. The α-Fe(Zn) phase was confirmed by SEM-EDS, STEM-EDS, and EBSD, showing Al enrichment and Mn depletion. At 700 ms, cracks initiated at the weld shoulder. IMs were absent at the crack opening but appeared as discontinuous and fragmented layers farther from the weld centre. Between 900 ms and 1700 ms, crack width and depth increased, and no IMs were present at the interface.

The FEA model, validated by comparison of simulated and experimental weld nugget areas, was used to analyse temperature distribution during welding. Simulations showed that at 500 ms, shoulder temperatures at selected locations matched the stability range for δ, Γ, Γ_1, and α-Fe(Zn), supporting the formation of continuous IM layers. At 700 ms, higher local temperatures predicted partial IM stability, consistent with fragmented layers observed experimentally. At 900 ms, temperatures exceeded the IM stability range, corresponding to conditions favourable for LME crack formation.

Overall, the combined experimental and simulation results show that Fe-Zn IM formation occurs before LME crack initiation and that increasing weld time leads to IM breakdown as local temperatures exceed their stability range. The validated FEA model provides a reliable method to link temperature and Fe-Zn IM formation during RSW of TWIP steel.

References

[1] G. Mahadevan, V. Bertolo, S. Sabooni, H. Gao, V. Popovich, L. A. I. Kestens and M. Hermans. ‘Characterizing the influence of weld time on the Fe-Zn interface during liquid metal embrittlement of resistance spot welded TWIP steel’.

In: *Materials Science and Engineering: A* 972 (Oct. 2026), p. 150666. ISSN: 0921-5093. DOI: 10.1016/j.msea.2026.150666. URL: https://www.sciencedirect.com/science/article/pii/S0921509326009469.

[2] S. P. Murugan, V. Vijayan, C. Ji and Y. D. Park. 'Four types of LME cracks in RSW of Zn-coated AHSS'. In: *Weld J* 99.3 (2020), 75s–92s.

[3] E. E. Glickman. 'Dissolution Condensation Mechanism of Stress Corrosion Cracking in Liquid Metals: Driving Force and Crack Kinetics'. In: *Metallurgical and Materials Transactions A* 42.2 (1st Feb. 2011), pp. 250–266. ISSN: 1543-1940. DOI: 10.1007/s11661-010-0429-6.

[4] E. Glickman. 'Grain Boundary Grooving Accelerated by Local Plasticity as a Possible Mechanism of Liquid Metal Embrittlement'. In: *Interface Science* 11.4 (1st Oct. 2003), pp. 451–459. ISSN: 1573-2746. DOI: 10.1023/A:1026100112248.

[5] V. V. Popovich and I. G. Dmukhovskaya. 'Rebinder effect in the fracture of Armco iron in liquid metals'. In: *Soviet materials science : a transl. of Fiziko-khimicheskaya mekhanika materialov / Academy of Sciences of the Ukrainian SSR* 14.4 (1st July 1978), pp. 365–370. ISSN: 1573-885X. DOI: 10.1007/BF01154711.

[6] W. Dong, K. Ding, H. Pan, M. Lei and Y. Gao. 'Effect of Welding Current on Liquid Metal Embrittlement of the Resistance Spot Welded Galvanized QP980 Advanced High-Strength Steel'. In: *TMS 2022 151st Annual Meeting & Exhibition Supplemental Proceedings*. The Minerals, Metals & Materials Series. Cham: Springer International Publishing, 2022, pp. 1254–1261. ISBN: 978-3-030-92381-5. DOI: 10.1007/978-3-030-92381-5_119.

[7] Z. Ling, T. Chen, L. Kong, M. Wang, H. Pan and M. Lei. 'Liquid Metal Embrittlement Cracking During Resistance Spot Welding of Galvanized Q&P980 Steel'. In: *Metallurgical and Materials Transactions A* 50.11 (1st Nov. 2019), pp. 5128–5142. ISSN: 1543-1940. DOI: 10.1007/s11661-019-05388-6.

[8] J. S. Dohie, J. Cahoon and W. Caley. 'The Grain-Boundary Diffusion of Zn in α-Fe'. In: *Journal of Phase Equilibria and Diffusion* 28.4 (1st Aug. 2007), pp. 322–327. ISSN: 1863-7345. DOI: 10.1007/s11669-007-9093-y.

[9] Y. Ikeda, H. C. Ni, A. Chakraborty, H. Ghassemi-Armaki, J. M. Zuo, R. D. Kamachali and R. Maaß. 'Segregation-induced grain-boundary precipitation during early stages of liquid-metal embrittlement of an advanced high-strength steel'. In: *Acta Materialia* 259 (15th Oct. 2023), p. 119243. ISSN: 1359-6454. DOI: 10.1016/j.actamat.2023.119243.

[10] M. H. Razmpoosh. 'Investigation of Liquid-Metal-Embrittlement Crack-path: Role of Grain Boundaries and Responsible Mechanism'. Accepted: 2020-07-24T17:23:26Z. PhD thesis. University of Waterloo, 24th July 2020.

[11] A. Ghatei-Kalashami, M. S. Khan, F. Goodwin and Y. N. Zhou. 'Investigating the mechanism of zinc-induced liquid metal embrittlement crack initiation in austenitic microstructure'. In: *Journal of Materials Science* (17th Oct. 2023). ISSN: 1573-4803. DOI: 10.1007/s10853-023-08963-w.

[12] S. P. Murugan, J. Kim, J. Kim, Y. Wan, C. Lee, J. B. Jeon and Y.-D. Park. 'Role of liquid Zn and α-Fe(Zn) on liquid metal embrittlement of medium Mn steel: An ex-situ microstructural analysis of galvannealed coating during high temperature tensile test'. In: *Surface and Coatings Technology* 398 (25th Sept. 2020), p. 126069. ISSN: 0257-8972. DOI: 10.1016/j.surfcoat.2020.126069.

[13] S. Feliu Jr. and V. Barranco. 'XPS study of the surface chemistry of conventional hot-dip galvanised pure Zn, galvanneal and Zn-Al alloy coatings on steel'. In: *Acta Materialia* 51.18 (2003), pp. 5413–5424. DOI: 10.1016/S1359-6454(03)00408-7.

[14] H. Biber. 'Scanning auger microprobe study of hot-dipped regular-spangle galvanized steel: Part I. surface composition of As-produced sheet'. In: *Metallurgical Transactions A* 19.6 (1988), pp. 1603–1608. DOI: 10.1007/BF02674035.

[15] A. Rodnyansky, Y. Warburton and L. Hanke. 'Segregation in hot-dipped galvanized steel'. In: *Surface and Interface Analysis* 29.3 (2000), pp. 215–220. DOI: 10.1002/(SICI)1096-9918(200003)29:3<215::AID-SIA703>3.0.CO;2-X.

[16] Y. Ikeda, R. Yuan, A. Chakraborty, H. Ghassemi-Armaki, J. M. Zuo and R. Maaß. 'Early stages of liquid-metal embrittlement in an advanced high-strength steel'. In: *Materials Today Advances* 13 (1st Mar. 2022), p. 100196. ISSN: 2590-0498. DOI: 10.1016/j.mtadv.2021.100196.

[17] C. Böhne, G. Meschut, M. Biegler and M. Rethmeier. 'Avoidance of liquid metal embrittlement during resistance spot welding by heat input dependent hold time adaption'. In: *Science and Technology of Welding and Joining* 25.7 (1st Oct. 2020), pp. 617–624. ISSN: 1362-1718. DOI: 10.1080/13621718.2020.1795585.

[18] S. Dwibedi, B. Kumar, S. R. Bhoi, S. R. Tripathy, S. Pattanaik, S. Prasad and R. Behera. 'To investigate the influence of weld time on joint characteristics of Hastelloy X weldments fabricated by RSW process'. In: *Materials Today: Proceedings*. 10th International Conference of Materials Processing and Characterization 26 (1st Jan. 2020), pp. 2763–2769. ISSN: 2214-7853. DOI: 10.1016/j.matpr.2020.02.576.

[19] H. Moshayedi and I. Sattari-Far. 'Resistance spot welding and the effects of welding time and current on residual stresses'. In: *Journal of Materials Processing Technology* 214.11 (1st Nov. 2014), pp. 2545–2552. ISSN: 0924-0136. DOI: 10.1016/j.jmatprotec.2014.05.008.

[20] H. Long, Y. Hu, X. Jin, J. Shao and H. Zhu. 'Effect of holding time on microstructure and mechanical properties of resistance spot welds between low carbon steel and advanced high strength steel'. In: *Computational Materials Science* 117 (1st May 2016), pp. 556–563. ISSN: 0927-0256. DOI: 10.1016/j.commatsci.2016.01.011.

[21] H. Zhang and J. Senkara. *Resistance Welding: Fundamentals and Applications*. Boca Raton: CRC Press, 20th Dec. 2005. 444 pp. ISBN: 978-0-429-10159-5. DOI: 10.1201/b12507.

[22] M. Krenn. *Characterization of Fe-Zn Intermetallic Compounds via Advanced Electron Microscopy / Author Martin Krenn*. 2025.

[23] H. Inui, N. L. Okamoto and S. Yamaguchi. 'Crystal Structures and Mechanical Properties of Fe–Zn Intermetallic Compounds Formed in the Coating Layer of Galvannealed Steels'. In: *ISIJ International* 58.9 (2018), pp. 1550–1561. DOI: 10.2355/isijinternational.ISIJINT-2018-066.

[24] D. Bhattacharya. 'Liquid metal embrittlement during resistance spot welding of Zn-coated high-strength steels'. In: *Materials Science and Technology* 34.15 (13th Oct. 2018). _eprint: https://doi.org/10.1080/02670836.2018.1461595, pp. 1809–1829. ISSN: 0267-0836. DOI: 10.1080/02670836.2018.1461595.

[25] Y. G. Kim, I. J. Kim, J. S. Kim, Y. I. Chung and D. Y. Choi. 'Evaluation of Surface Crack in Resistance Spot Welds of Zn-Coated Steel'. In: *MATERIALS TRANSACTIONS* 55.1 (2014), pp. 171–175. DOI: 10.2320/matertrans.M2013244.

[26] V. Bertolo, G. Mahadevan, R. de Kloe, R. H. Petrov and V. Popovich. 'Decoupling early-stage cracking and propagation mechanisms in liquid metal embrittlement of Zn-galvanised TWIP steel'. In: *Journal of Materials Research and Technology* 38 (1st Sept. 2025), pp. 1617–1632. ISSN: 2238-7854. DOI: 10.1016/j.jmrt.2025.08.055.

[27] Y. Waseda, E. Matsubara and K. Shinoda. *X-Ray Diffraction Crystallography: Introduction, Examples and Solved Problems*. Berlin, Heidelberg: Springer, 2011. ISBN: 978-3-642-16634-1 978-3-642-16635-8. DOI: 10.1007/978-3-642-16635-8.

[28] K. Liu, X. Huang, W. Yang, P. Wang and H. Xu. 'Phase Equilibria of the Fe-Mn-Zn System at 600°C'. en. In: *JOM* 75.11 (Nov. 2023), pp. 4762–4770. ISSN: 1543-1851. DOI: 10.1007/s11837-023-06054-4. URL: https://doi.org/10.1007/s11837-023-06054-4.

[29] O. K. von Goldbeck. 'Fe—Zn Iron—Zinc'. In: *IRON—Binary Phase Diagrams*. Ed. by O. K. von Goldbeck. Berlin, Heidelberg: Springer, 1982, pp. 172–175. ISBN: 978-3-662-08024-5. DOI: 10.1007/978-3-662-08024-5_79.

[30] H. Lee, M. C. Jo, S. S. Sohn, S.-H. Kim, T. Song, S.-K. Kim, H. S. Kim, N. J. Kim and S. Lee. 'Microstructural evolution of liquid metal embrittlement in resistance-spot-welded galvanized TWinning-Induced Plasticity (TWIP) steel sheets'. In: *Materials Characterization* 147 (1st Jan. 2019), pp. 233–241. ISSN: 1044-5803. DOI: 10.1016/j.matchar.2018.11.008.

[31] J. Cui, K. Li, Z. Yang, Z. Wu and Y. Wu. 'Investigation of effects of aluminum additions on microstructural evolution and mechanical properties of ultra-high strength and vanadium bearing dual-phase steels'. In: *Journal of Materials Research and Technology* 31 (1st July 2024), pp. 1117–1131. ISSN: 2238-7854. DOI: 10.1016/j.jmrt.2024.06.148.

[32] R. L. Klueh, P. J. Maziasz and E. H. Lee. ‘Manganese as an austenite stabilizer in Fe□Cr□Mn□C steels’. In: *Materials Science and Engineering: A* 102.1 (1st June 1988), pp. 115–124. ISSN: 0921-5093. DOI: 10.1016/0025-5416(88)90539-3.

[33] R. Frappier, P. Paillard, R. L. Gall and T. Dupuy. ‘Embrittlement of Steels by Liquid Zinc: Crack Propagation after Grain Boundary Wetting’. In: *Advanced Materials Research* 922 (2014), pp. 161–166. ISSN: 1662-8985. DOI: 10.4028/www.scientific.net/AMR.922.161.

[34] D. Bhattacharya, L. Cho, E. van der Aa, A. Pichler, N. Pottore, H. Ghassemi-Armaki, K. O. Findley and J. G. Speer. ‘Influence of the starting microstructure of an advanced high strength steel on the characteristics of Zn-Assisted liquid metal embrittlement’. In: *Materials Science and Engineering: A* 804 (15th Feb. 2021), p. 140391. ISSN: 0921-5093. DOI: 10.1016/j.msea.2020.140391.

5

Effect of steel microstructure on LME crack path

Liquid Metal Embrittlement during RSW of Zn-coated TWIP steel results in intergranular cracking driven by the interaction of liquid Zn, stress, and the GB network. This chapter investigates how GB misorientation and orientation relative to the electrode force loading axis influence LME crack path selection across six weld times from 700 ms to 1700 ms. A comparative framework was developed in which, at each triple junction along the LME crack, the misorientation and angle relative to the loading axis of the LME GB are evaluated against those of the LME-free GB. Σ3 coherent twin boundaries were LME-free at all weld times regardless of their orientation to the stress axis. Non-twin CSL boundaries (Σ5 to Σ41 were predominantly LME-free at low weld times but progressively became LME GBs at high weld times, when their stress normalisation factor - a measure of a GBs alignment with the loading axis - exceeded that of the competing boundary. The fraction of triple junctions where the LME GB had the higher stress normalisation factor increased from 58% at 700 ms to 93% at 1700 ms, while the preference for the higher-misorientation-angle boundary declined from 73% to 56% over the same range. An LME susceptibility index incorporating GB energy, temperature-dependent Zn diffusivity, and stress alignment is proposed as a framework for predicting crack path selection and guiding GB engineering strategies to reduce LME in resistance spot welded TWIP steel.

5.1. Introduction

The context for this study on crack path selection, including the properties of TWIP steel, the role of zinc coatings, and the RSW process, is described in Chapter 2. The present chapter focuses specifically on how GB character governs LME crack path selection during RSW, and how this relationship evolves with increasing weld time.

Parts of this chapter have been published in Materialia, Volume 48 (2026) [1].

Several micro-mechanisms have been proposed depending on the solid/liquid metal system involved, as discussed in Section 2.4.1. For the Fe-Zn system, stress-assisted GB (GB) diffusion is considered the dominant micro-mechanism. Stress-assisted LME models are derived from the Rehbinder effect, in which liquid Zn penetrates GBs, reduces the surface energy of the steel, and promotes embrittlement once a critical stress level is exceeded [2–4] . Since stress-assisted GB diffusion is considered to play a dominant role in the Fe-Zn system, the characteristics of the GBs influence LME crack initiation and propagation. Among these characteristics, GB misorientation is a fundamental crystallographic parameter that defines the orientation relationship between adjacent grains [2, 5, 6]. Because GB structure and energy are directly related to misorientation, variations in misorientation affect the susceptibility of specific boundaries to liquid Zn penetration under the combined action of stress and temperature during RSW [3]. Therefore, understanding how GB misorientation influences LME behaviour is essential for clarifying crack path selection and identifying which boundaries are more likely to act as preferential pathways for crack growth.

Bhattacharya et al. studied the influence of starting microstructure on the severity of embrittlement in Zn coated AHSS [7]. The study concluded that the prior austenitic GBs (PAGBs) provided low energy paths for crack propagation and hence are preferred for embrittlement. The DP steel's lower area fraction of PAGBs, because of the inter-critical annealing, reduces the availability of low energy paths for crack propagation [7].

Although misorientation angles were measured between grains on either side of the crack, the number of GBs misorientation angles analysed was insufficient to ascertain which grains were preferred for crack propagation. For a given microstructure, it was observed that for a misorientation angle greater than 15°, a lower critical stress is required for LME, due to the increase in GB energy [8]. Atomistic models and TEM observations were employed to study the kinetics of liquid metal penetration in the Al-Ga system. The observations of this study quantitatively verified that a low unit cell volume of the coincident site lattice (CSL) Σ GBs enabled much slower liquid metal penetration compared to high Σ GBs. Razmpoosh et al. validated these observations for a Fe-Zn system, and investigated the influence of GB misorientation angle and crystallographic plane on LME crack propagation and LME susceptibility of the FCC Fe-Zn couple [9]. A trace analysis technique using EBSD was applied to LME susceptible GBs, where it was concluded that the orientation of GB planes had a significant effect on the crack path. It was observed that liquid Zn penetrated the GBs of the Fe matrix along high-index planes and the (5 3 1) plane had the highest susceptibility to exhibit LME [9]. According to Razmpoosh et al., LME cracks in Fe-Zn systems tend to follow high□angle random austenite GBs, and the susceptibility of these boundaries depends on the tensile stress component normal to the boundary plane, with a threshold stress of roughly 80% of the yield strength required to trigger liquid Zn penetration and grain□boundary decohesion. According to Gong et al., the applied stress axis controls both the depth and rate of liquid metal penetration along GBs once a critical normal stress on the boundary is exceeded [10]. According to Hong et al., the susceptibility of individual GBs to embrittle is governed by the stress component perpendicular to the grain□boundary plane together with the grain□boundary character, so that high□angle random, high□index boundaries with larger excess free volume are most prone to embrittlement, whereas

low□Σ CSL boundaries remain comparatively LME resistant [11]. Bertolo et al. studied Zn-galvanised TWIP steel and deliberately induced LME cracks, then reconstructed the crack path relative to the austenite GB network [12]. Using EBSD mapping and tracing the crack path, the study showed that intergranular LME cracks preferentially propagate along HAGBs and avoid low-Σ CSL boundaries. In this framework, the global tensile axis defines the stress state, and the orientation of individual boundaries relative to this axis determines the resolved normal stress and their susceptibility to LME. Although previous studies have examined the role of grain-boundary character in LME crack propagation, how these relationships evolve under the conditions present during RSW has not been systematically studied. In particular, the combined influence of GB misorientation and the orientation of GBs relative to the loading axis during welding remains unclear. Furthermore, the extent to which welding parameters affect these relationships during crack propagation is not well understood. Therefore, this study investigates how GB misorientation and GB orientation with respect to the loading axis influence LME crack paths, and how these effects change under different welding parameters during RSW.

5.2. Materials and Methods

The materials used in the RSW study, the RSW setup, parameters and the characterization tools used to analyse weld cross-sections are presented in Chapter 3. The FEA modelling framework in SORPAS used in this chapter to simulate stress distributions is detailed in Section 3.4. The simulations focused on the weld shoulder area, where LME cracks were observed in the experiments. The model was configured to replicate the experimental welding conditions, including sheet materials, sheet thicknesses, electrode geometry, and applied welding parameters. The simulations provided the evolution of stress components in the x and y directions as a function of time at the weld shoulder. These stress-time profiles were used to assess the orientation of the loading axis relative to the GBs in the TWIP steel.

5.3. Results

5.3.1. Microstructure characterization of LME cracks

Figure 5.1 presents the EBSD image quality (IQ) maps of LME cracks obtained from the different RSW conditions, covering weld times from 700 ms to 1700 ms. No LME cracks were observed at weld times of 300 ms and 500 ms, so these weld conditions are not part of the study. The IQ maps also reveal the GB network in the cross-section. In the figure, black lines represent high angle GBs (HAGBs) with misorientations between 15° and 65°, while blue lines denote low angle GBs (LAGBs) with misorientations between 5° and 15°. Σ3 CSL GBs are highlighted in red and represent twin boundaries, which are predominant in TWIP steel. The LME crack in Figure 5.1 at a weld time of 1700 ms is observed to propagate into the weld fusion region. Figure 5.2 also shows how the LME crack depth and width is measured and the variation in LME crack depth and width as a function of weld time. Both crack depth and width increase with increasing weld time, which can be attributed to the higher heat input during welding.

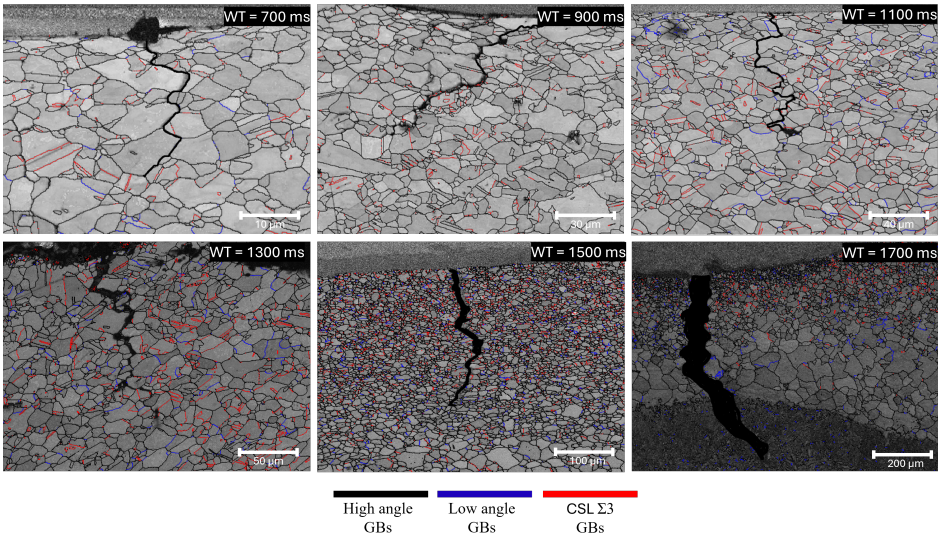


Figure 5.1: EBSD image quality map showing LME cracks and grain structure for different RSW weld times in the weld shoulder region

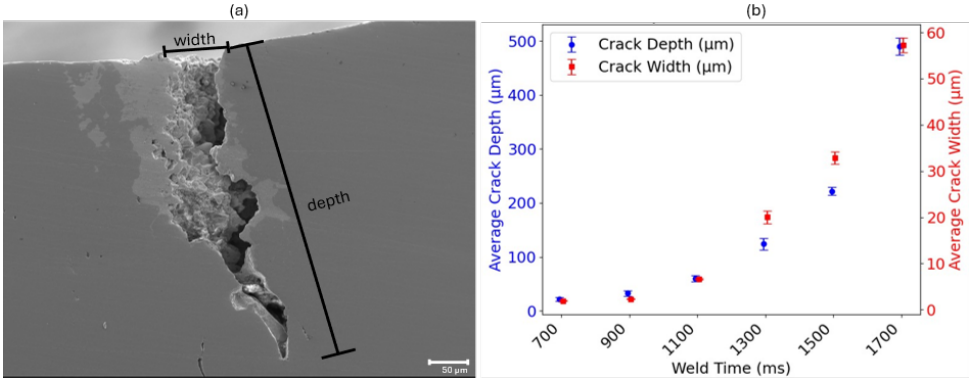


Figure 5.2: (a) Schematic diagram for crack dimension measurement (b) Average LME crack depth and crack width at different weld times

5.3.2. Analysis framework

The misorientation analysis framework used in this study is illustrated schematically in Figure 5.3. This framework is adapted from the study by Bertolo et al [12]. Figure 5.3(a) shows a schematic representation of the grain structure and GB network in the TWIP steel RSW cross-section. Two distinct categories of GB misorientations are identified and measured. The first category, indicated by blue arrows, are the misorientations

between adjacent grains separated by the LME crack - that is, the GBs along which LME crack propagation occurs. These are referred to henceforth as 'LME GBs'. In the schematic, this corresponds to the misorientations between grain pairs G1/G2, G2/G3, G3/G4, G4/G5, and G5/G6. The second category, indicated by red arrows, comprises the misorientations between grains that form part of a triple junction that the LME crack passes through, but did not propagate - that is, the GBs at each triple junction that were available to the crack as an alternative path but were not selected. These are referred to henceforth as LME-free GBs. In the schematic, these correspond to grain pairs G1/G3, G2/G4, G3/G5, and G4/G6. This paired measurement at each triple junction - one LME GB and one LME-free GB forms the basis of the comparative crack path analysis. By comparing the LME and LME-free GBs, the study aims to understand how the GB character affects the LME crack path under changing RSW parameters. The loading direction in Figure 5.3(a) corresponds to the direction of the applied electrode force during RSW, which generates compressive stresses along this axis. The magnitude of the stresses in the y-axis (loading direction) and x-axis is shown in Figure 5.4, where both the electrode-axis (y) component σ_y and the transverse (x) component σ_x are negative. This compressive stress state is from the combined effect of thermal expansion and the electrode force [13, 14]. The y-component is more compressive than the x-component ($\sigma_y < \sigma_x < 0$) for the entire duration of the RSW cycle. Under this biaxial stress state, the normal stress acting on a GB inclined at angle θ to the y-axis is given by the standard plane-stress transformation [15]:

$$\sigma_n(\theta) = \sigma_y.sin^2(\theta) + \sigma_x.cos^2(\theta) \tag{5.1}$$

In the stress-assisted GB diffusion model, it is the stress component normal to the boundary plane that governs the thermodynamic driving force for Zn transport along the boundary [16]. The Fe-Zn system undergoes GB wetting governed by the condition $\gamma_{GB} > 2\gamma_{SL}$ independent of the macroscopic stress state [17, 18]. Once Zn has penetrated a boundary, the stress-assisted diffusion model predicts that the diffusing Zn atoms generate local tensile stress at the crack tip through a wedging mechanism, providing the driving force for intergranular decohesion even in the absence of macroscopic tensile loading [16]. The angle between an LME GB and the loading direction is denoted by θ, and the corresponding angle for an LME-free GB is denoted ϕ. From these angles, a stress factor is defined as the cosine of the angle θ/ϕ the GB makes with the loading direction which is equal to 1 when the GB is parallel to the loading axis and 0 when the GB is perpendicular to the loading axis. The stress factor therefore provides a normalised scalar measure of the mechanical driving force acting on each GB. The macroscopic biaxial compressive field measured in this study therefore does not prevent LME from occurring. Boundaries experiencing the least compressive normal stress i.e. those most parallel to the electrode force direction, are the least mechanically suppressed pathways for Zn-driven crack propagation, which is the basis for the stress normalisation factor used in this analysis. It should be noted that the stress normalisation factor used throughout this analysis is a geometric approximation derived from the macroscopic, bulk stress field at the weld shoulder as computed by FEA. It does not capture the local stress state at individual GBs, which is modified by elastic and plastic anisotropy between neighbouring grains, local stress concentrations

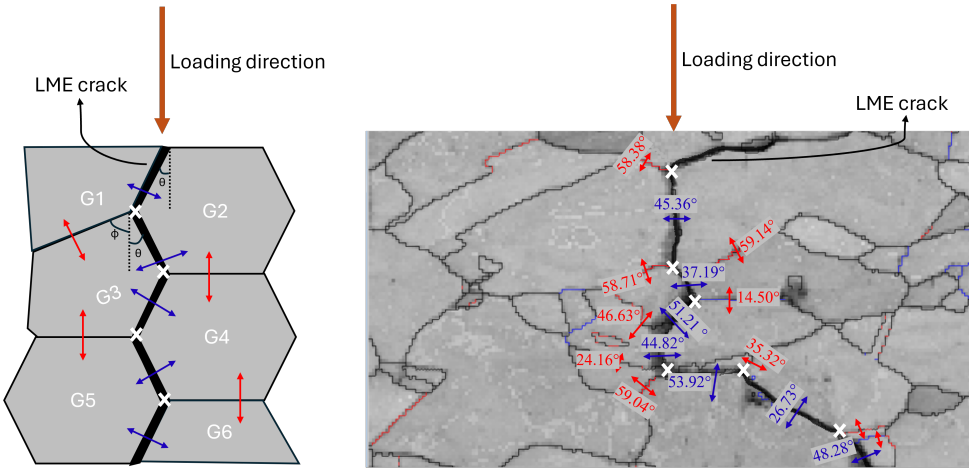


Figure 5.3: (a) Schematic representation of grain structure surrounding LME crack with white X denoting GB triple junctions, blue arrows denoting LME GBs and red arrows denoting LME-free GBs (b) Representative EBSD IQ map showing GB misorientation measurements surrounding LME cracks.

at triple junctions, and the changing temperature across the HAZ during the weld cycle [19]. As a result, the stress normalisation factor should be interpreted as a relative metric to compare two competing boundaries at a triple junction. This approximation is considered acceptable to compare which of two boundaries at the same triple junction experiences the less compressive normal stress, where both boundaries are subject to the same macroscopic stress state.

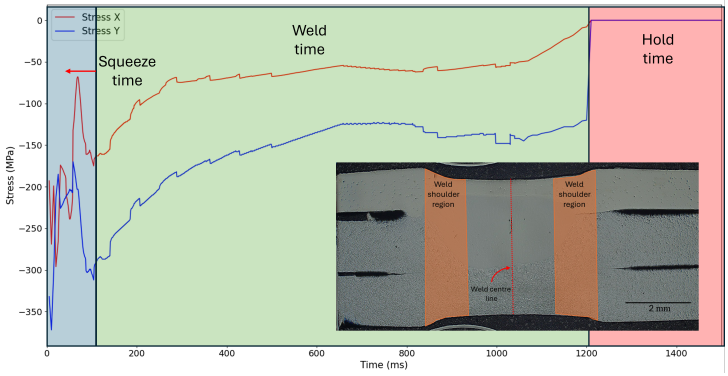


Figure 5.4: Stress in the X and Y directions vs time plot in the weld shoulder region calculated using the FEA model

Figure 5.3(b) shows a representative EBSD IQ map illustrating the LME crack path and the misorientation measurements made at LME GBs and LME-free GBs at triple junctions ahead of the crack. The GB misorientations calculated from the EBSD data capture both the misorientation angle and the misorientation axis. This measurement procedure was applied to all LME cracks observed across the six weld times investigated in this study (700 ms, 900 ms, 1100 ms, 1300 ms, 1500 ms, and 1700 ms). At a weld time of 1700 ms, the width of the LME crack was too large to directly determine the original GB structure across the crack. To address this, the micrograph was separated along the crack and the regions on either side were reconstructed and stitched together, as illustrated in Figure 5.5. This reconstruction was possible by matching features such as grain morphology and the geometry of the weld fusion zone on both sides of the crack, which allowed neighbouring grains to be identified. GB orientation relationships were determined only for the FCC TWIP phase of the steel and were not evaluated within the fusion zone.

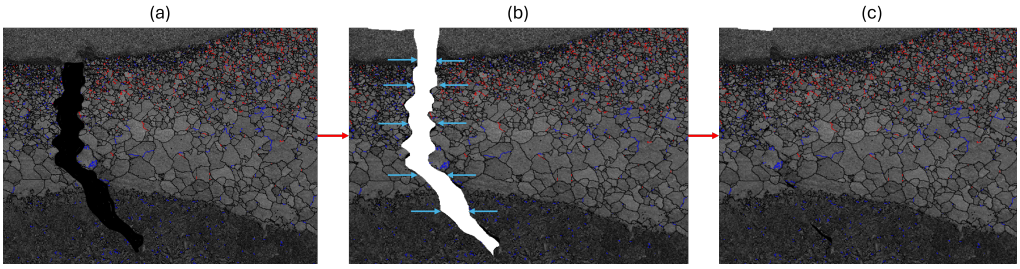


Figure 5.5: (a) IQ map showing GBs at weld time = 1700 ms (b) process of 'closing' the LME crack to identify neighbouring grains (c) reconstructed GB map to perform misorientation analysis

5.3.3. GB MISORIENTATION AND LOADING AXIS ORIENTATION

Figure 5.6 presents the misorientation angle distributions for LME GBs and LME-free GBs for all weld times, and Figure 5.7 shows the misorientation distribution function (MDF) map for all LME and LME-free GBs at all weld times combined in one map. The distribution of LME GB misorientation angles follows an approximately Gaussian profile centred in the range of 35-55°. The unwelded base microstructure is also observed to have the same distribution as the LME-free GBs of the welded samples. This indicates that the LME crack does not exhibit a strong preference for a specific misorientation angle within in the HAGB range. The crack propagates through random HAGBs that constitutes the majority of boundaries in the material. The number of triple junctions identified for each weld time is summarised in Table 5.1. At each triple junction, there is an LME GB and LME-free GB ahead of it. From both figures, it can be seen that for LME GBs, the MDF reveals a preferential clustering of misorientations in the <111> tilt axis family at misorientation angles between approximately 25° and 45° where the crack propagates through random HAGBs that constitutes the majority of boundaries in the material. In contrast, for LME-free GBs, the MDF displays a sharp, high-intensity

peak at the <111> axis and misorientation angles of 55-65°, which corresponds to Σ3 CSL coherent twin boundaries that are a characteristic microstructural feature of low stacking fault energy TWIP steels [20]. This observation holds consistently across all weld times investigated in this study: in every condition, the LME crack path never propagated through a Σ3 twin boundary. The avoidance of Σ3 boundaries by the LME crack, regardless of weld time or temperature indicates that these boundaries are a barrier to liquid metal penetration and crack propagation.

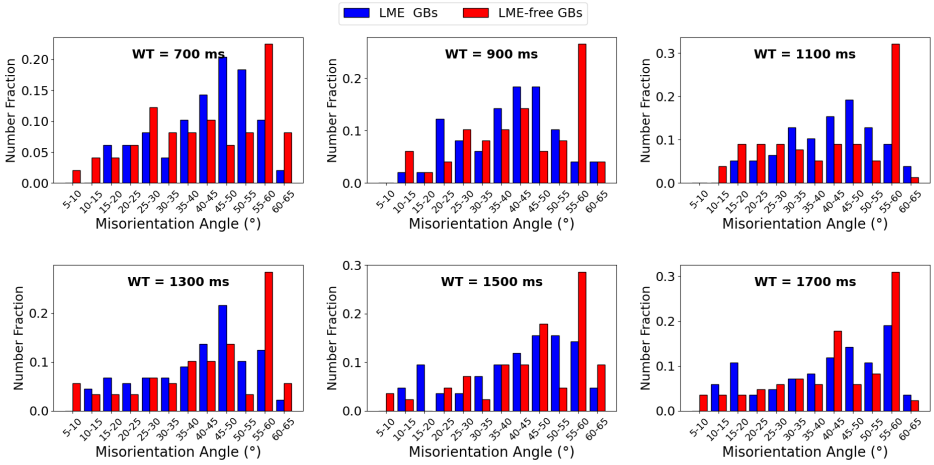


Figure 5.6: Misorientation angle distribution of LME and LME-free GBs for all weld times

Table 5.1: Number of triple junctions analysed at different weld times

Weld time (ms)	Number of triple junctions analysed
700	52
900	55
1100	64
1300	77
1500	89
1700	85

At each triple junction the LME crack passes through, the crack faces a choice between two GBs that differ in their misorientation angle and orientation relative to the loading axis. To determine which of these factors govern the path the LME crack selects and how they are affected by weld time, the assessed misorientation and the stress normalisation factor is plotted for both sets of GBs at each triple junction. Figure 5.8 presents scatter plots of the stress normalisation factor against misorientation angle for LME GBs and LME-free GBs across all six weld times. GBs are classified into six categories to enable systematic comparison: (a) LME LAGBs (misorientation < 15°), (b)

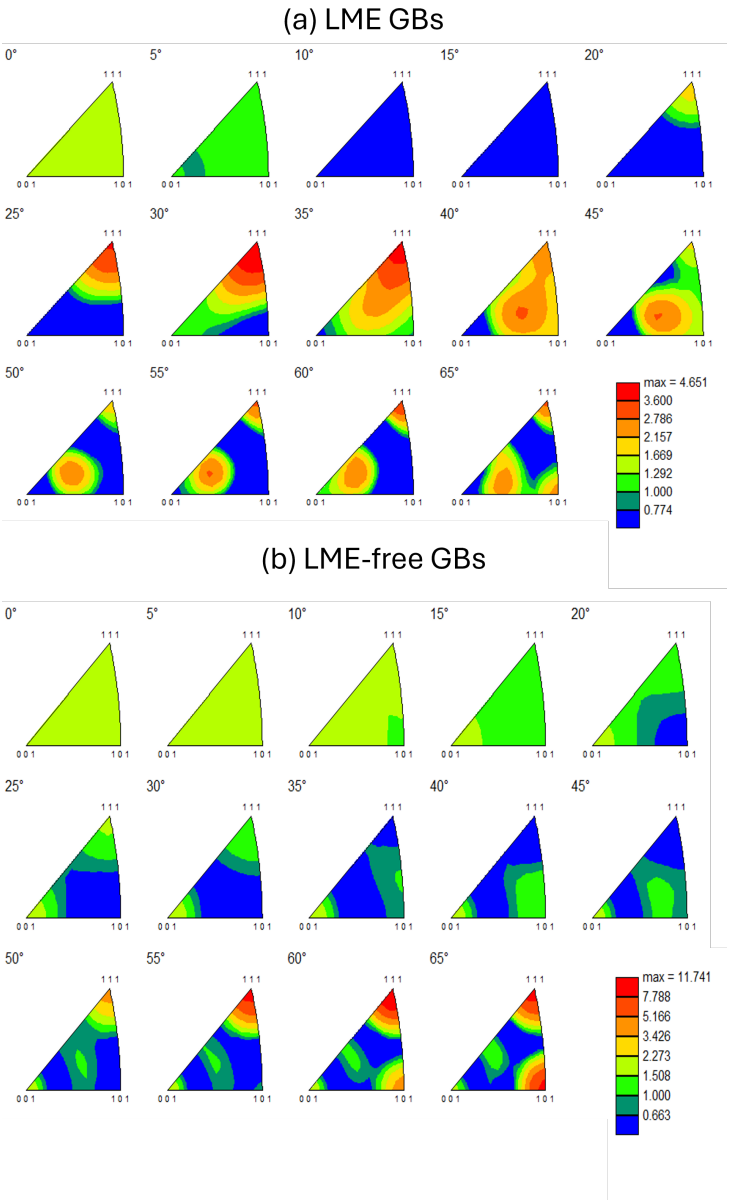


Figure 5.7: Misorientation distribution function for (a) LME GBs (b) LME-free GBs

LME HAGBs (misorientation ≥ 15°, non-CSL), (c) LME CSL GBs (Σ5 – Σ41, excluding Σ3), (d) LME-free HAGBs, (e) LME-free CSL GBs (Σ5-Σ41), and (f) LME-free Σ3 GBs. For HAGBs through which the crack propagates (filled blue circles), the distribution evolves with weld time. At 700 ms, these boundaries are spread across the full stress

normalisation factor range (0.1-1.0) with misorientation angles between 25-55°. With increasing weld time, the GBs progressively cluster at higher stress factors. When the weld time is above 1300 ms most points lie between 0.8-1.0, and at 1700 ms they are concentrated near 1. For LAGBs that the LME crack propagates through (filled blue triangles), the stress normalisation factor lies between 0.6 and 1.0 at all weld times, indicating that crack propagation through LAGBs occurs only when they are well aligned with the loading axis. Σ3 CSL boundaries (filled red triangles) were consistently observed to be LME-free. Non-Σ3 CSL GBs the LME crack propagated through (filled red squares) were not observed at the lowest weld time but appear at higher weld times, primarily at high stress normalisation factors, indicating crack propagation when their orientation is more aligned with the loading axis. LME-free HAGBs (filled red circles) are distributed broadly across all stress factors and misorientation angles at every weld time, and this distribution does not change significantly between 700 ms and 1700 ms. However, their overall fraction decreases with weld time. LME-free non-Σ3 CSL boundaries (filled red squares) are present across all stress factors up to a weld time of 1100 ms, but at higher weld times some of these boundaries allow LME cracks to propagate through when their stress factor is sufficiently high. The distribution of stress normalisation factors for LME and LME-free GBs and the average angle of both sets of GBs with the loading axis is shown in Figure 5.9. These individual trends are further quantified in Figure 5.10, Figure 5.11 and Figure 5.12. For all weld times, the distribution for LME-free GBs remains largely unchanged across the full range of stress normalisation factors. In contrast, the distribution for LME GBs evolves with weld time. At 700 ms and 900 ms, although a peak is observed at high stress normalisation factors, LME GBs are present across the full range from 0 to 1. With increasing weld time, the fraction of LME GBs at higher stress normalisation factors (0.7-1.0) increases. By 1700 ms, no LME GBs are observed below a stress normalisation factor of 0.5, and approximately 80% of these GBs lie above 0.8.

Figure 5.10(a) shows that the percentage of Σ3 CSL boundaries remains approximately constant for all weld times. This is expected because these twin boundaries are uniformly distributed in the TWIP steel microstructure and are not affected by the welding parameters. Figure 15.10(b) shows the fraction of LME-free CSL boundaries that are not twin boundaries. This percentage decreases from 26% at a weld time of 700 ms to 15% at 1700 ms. Since the overall GB distribution in the microstructure does not change with weld time, this indicates that a greater fraction of these boundaries are embrittled at higher weld times.

Figure 5.11(a) shows the fraction of LME GBs that are LAGBs. This increases from 6% at 700 ms to 17.4% at 1700 ms. Figure 5.11(b) shows the percentage of LME GBs that are non-twin CSL boundaries (Σ5-Σ41). This fraction is 2.6% at 700 ms, increases to 4% at 1100 ms, and further increases to 16% at 1700 ms. When both boundaries ahead of a triple junction are random HAGBs, the preference for the boundary with the higher stress normalisation factor increases with weld time. At 700 ms, the boundary with the higher stress factor is selected in 63% of cases, increasing to 68% at 900 ms and 72% at 1100 ms. This trend becomes more pronounced at higher weld times, reaching 88% at 1300 ms, and remaining high at 85% and 87% for 1500 ms and 1700 ms, respectively.

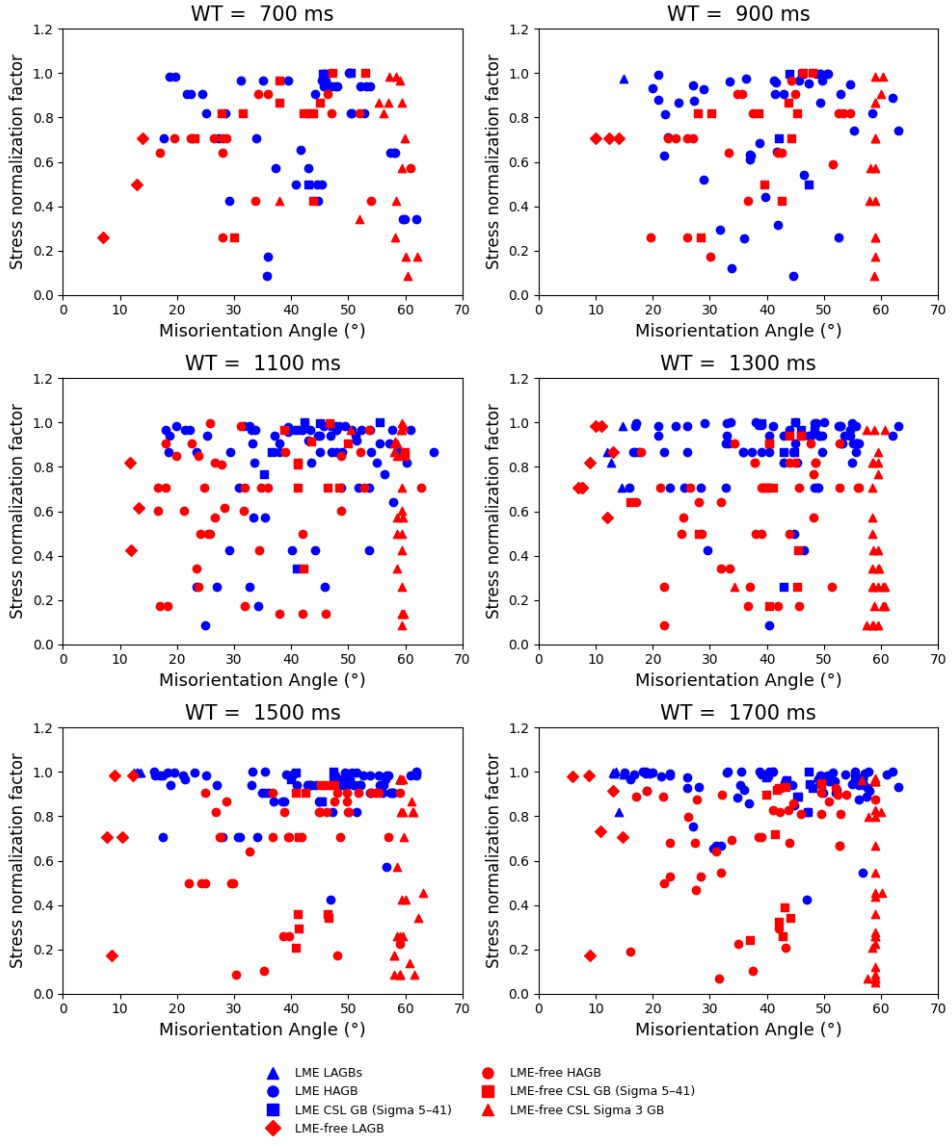


Figure 5.8: GB misorientation angle vs stress normalisation factor with loading axis of different types of GBs for all weld times

Figure 5.12(a) shows the percentage of triple junctions where the LME GB has a higher misorientation angle than the LME-free GB, excluding CSL boundaries. Previous studies indicate that GBs with higher misorientation angles are more susceptible to LME. At a weld time of 700 ms, the higher misorientation GB was the preferred crack path

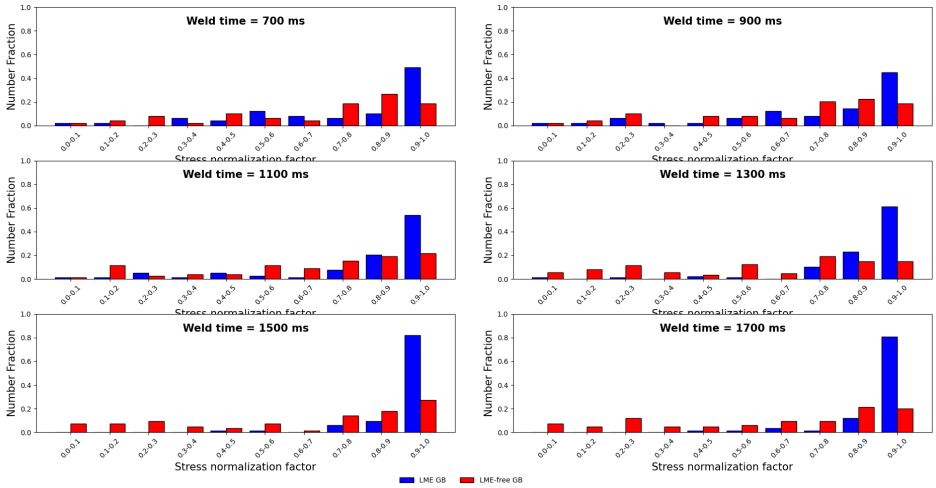


Figure 5.9: (a) Distribution of the stress normalisation factor for LME and LME-free grains for weld times from 700 ms to 1700 ms (b) Average angle of LME and LME-free GBs with the loading axis for weld times from 700 ms to 1700 ms

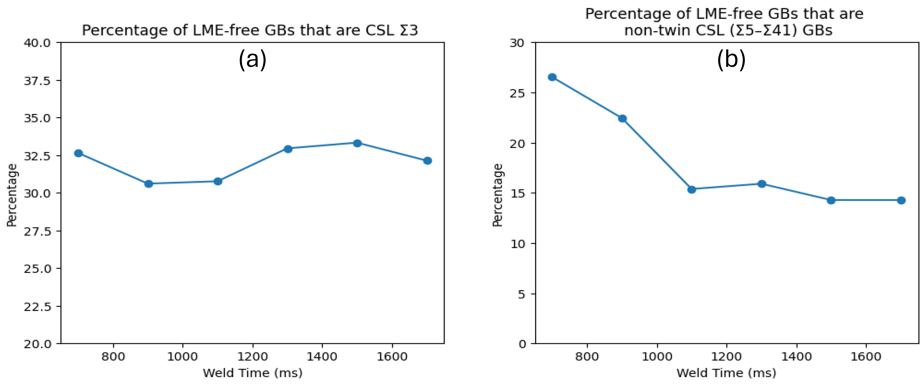


Figure 5.10: For weld times between 700 ms and 1700 ms, (a) Percentage of LME-free GBs are CSL Σ3 twin GBs (b) percentage of LME-free CSL GBs that are non CSL Σ3 GBs

in 73% of the cases. This percentage is 68% at 900 ms and 72% at 1100 ms, but decreases to 58% at 1300 ms, 55% at 1500 ms, and 56% at 1700 ms, indicating a downward trend. Figure 5.12(b) shows the percentage of cases where the LME GB has a higher stress normalisation factor than the LME-free GB, for non CSL boundaries. In contrast to misorientation, this metric shows a clear increasing trend. At 700 ms, the boundary with the higher stress normalisation factor is the preferred crack path in 58% of the cases, increasing to 91% at 1700 ms.

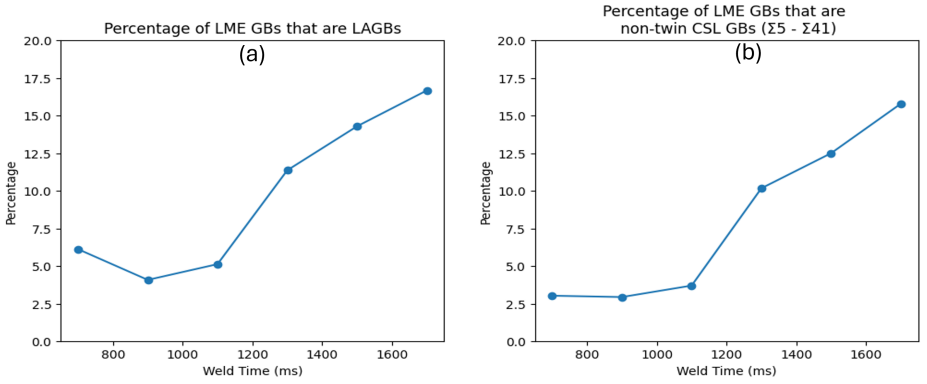


Figure 5.11: For weld times between 700 ms and 1700 ms, (a) Percentage of LME-free GBs are not CSL Σ3 twin GBs (b) percentage of LME-free CSL GBs that are non Σ3

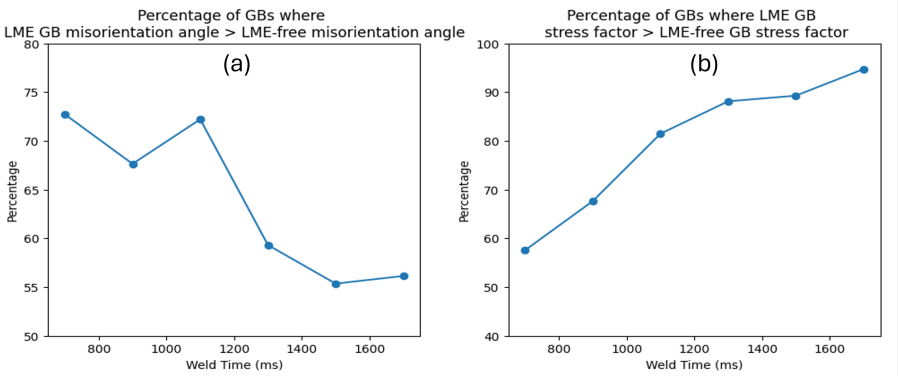


Figure 5.12: For weld times between 700 ms and 1700 ms, (a) percentage of GBs where the LME GB misorientation angle is greater than the LME-free misorientation angle (b) percentage of GBs where the LME GB stress normalization factor > LME-free GB stress factor1

5.4. Discussion

The results of this study are interpreted within the framework of stress assisted GB diffusion, which is the accepted transport mechanism for LME in the Fe-Zn system [3, 21, 22]. DiGiovanni et al. observed that Zn penetration depth increased with applied stress, with a diffusion profile predicted by the stress-assisted diffusion model of Klinger and Rabkin [16, 21]. Murugan et al. showed that LME sensitivity in galvannealed medium Mn steel during high-temperature tensile testing is governed not only by the presence of liquid Zn but by the fraction of effective liquid Zn available at the moment of deformation [23]. At the atomic scale, GB decohesion in the Fe-Zn system occurs when Zn atoms diffuse through the GB ahead of the propagating crack and weakens the Fe-Fe bonds and causes fracture under applied load [16]. Chen et al. found that the

segregation of TWIP steel alloying elements like Al, Mn, Mo, and Ti to the α/γ interface has an effect on the interfacial cohesion [24]. Based on this framework, the results presented in the previous section are now examined in detail. The influence of GB misorientation and orientation with respect to the loading axis on LME crack propagation is discussed by considering each type of GB individually. The analysis presented in this study is further used to propose a predictive index for LME susceptibility, combining the effects of GB character and stress alignment. In addition, these results are used to identify GB engineering strategies that can be applied to reduce LME susceptibility.

5.4.1. Effect of GB type on LME crack path

HAGBs

The misorientation angle distributions in Figure 5.6 show that the LME crack propagates predominantly through random HAGBs, consistent with the general HAGB distribution of the recrystallised austenite in TWIP steel [25]. This observation is in agreement with the studies by Razmpoosh et al., Bertolo et al. and Bhattacharya et al. who noted that higher misorientation angles correspond to higher GB energy, greater excess free volume, and faster GB diffusivity for substitutional solutes, and makes stress-assisted Zn diffusion kinetically faster along these boundaries [7, 9, 12]. The MDF for LME GBs in Figure 8 reveals clustering in the <111> tilt axis family at a misorientation of 25-45°, and is consistent with the observations of Bertolo et al. that misorientation angle above approximately 25° reduces the minimum stress factor required for LME to approach zero [12]. As more GBs become embrittled by Zn diffusion, the misorientation angle between competing boundaries at a triple junction becomes less useful in determining which boundary is susceptible to LME. When the analysis is limited to triple junctions where both competing boundaries are random HAGBs, the preference for the boundary with the higher stress normalisation factor increases with weld time. The percentage rises from 63% at 700 ms to 68% at 900 ms and 72% at 1100 ms, followed by a sharper increase to 88% at 1300 ms, and remains high at 85% and 87% for 1500 ms and 1700 ms, respectively. Since both boundaries in this case are structurally similar, this trend indicates that crack path selection is controlled by mechanical factors rather than GB misorientation. With increasing weld time, as more HAGBs become sufficiently embrittled, the crack preferentially follows boundaries better aligned with the loading axis.

CSL GBs

Σ3 coherent twin boundaries are avoided by the LME crack for all six weld times, despite these boundaries constituting 30-33% of available GBs. This observation validates previous findings by Razmpoosh et al and Bertolo et al. [9, 12]. Bertolo et al. confirmed this resistance specifically in the same TWIP steel under Gleeble hot tensile conditions, where no Σ3 boundary participated in Zn penetration or cracking even at stress normalisation factors as high as 0.8 [12]. The present RSW study demonstrates that this was observed across a range of weld times and correspondingly high temperatures and weld heat inputs. The thermodynamic condition for liquid metal GB penetration requires $\gamma_{GB} > 2\gamma_{SL}$, where γGB is the GB energy and γ_{SL} is the solid-liquid interfacial

energy [12]. For coherent Σ3 <111> twin boundaries in FCC austenite, the near-zero excess free volume means this condition is not met under the conditions of RSW, independent of stress state. In Figure 5.8, Σ3 boundaries (filled green triangles) appear at stress normalisation factors between 0.8-1 in all weld time conditions, without the crack propagating at any weld time.

The fraction of non-twin CSL (Σ5 - Σ41) boundaries in LME-free GBs (Figure 5.11a) varies from 26% at 700 ms to 15% at 1700 ms and the increase in LME GBs that are non-twin CSL boundaries (Figure 5.10b) from 3% to 16% show that these GBs are more prevalent in the LME crack path as the weld time increases. At each weld time condition there is an effective diffusion depth for Zn governed by the combined effects of temperature, applied stress, and time. These CSL boundaries have a lower excess free volume and GB energy than random HAGBs but higher than Σ3 [40]. Murugan et al. found that LME severity increases linearly with the fraction of effective liquid Zn at the deformation temperature [23]. In RSW, higher weld times increase peak HAZ temperature and reduce isothermal solidification extent during the weld cycle, increasing the effective liquid Zn fraction at the moment of peak stress. In 100% of the observed cases where the LME crack traversed a non-twin CSL boundary, the stress factor of that boundary exceeded that of the competing LME-free GB at the same triple junction. Gong et al.'s observation also shows that GB decohesion under LME is dependent on orientation, with boundaries aligned parallel to the loading axis showing little or no cracking even when structurally susceptible [10]. This demonstrates that structural embrittlement is a necessary but not sufficient condition for non-twin CSL boundaries: the mechanical driving force must also be locally favourable.

LAGBs

LAGB fraction increases with weld time in LME GBs from approximately 6% at 700 ms to 17% at 1700 ms (Figure 5.10). In contrast to random HAGBs, which at a weld time of 700 ms are distributed across a wide range of stress normalisation factors, LAGBs appear in the crack path exclusively at stress normalisation factors above 0.7 across all weld times. Razmpoosh et al. confirmed that low-angle random boundaries resist LME [9], and Bertolo et al. found in the same TWIP steel that LAGBs required a normalised stress factor of at least 0.5 to participate in LME under hot tensile conditions [12]. The present RSW results are consistent with both findings, and show that LAGBs are only affected by LME when they are well-aligned with the loading axis, when the stress normalisation factor is above 0.5. At weld times below 1300 ms, Zn diffusion is insufficient to overcome the barrier for diffusion via LAGBs [6, 26]. As weld time increases and HAZ temperatures rise, the Zn diffusivity along all boundary types increases, and the greater cumulative Zn flux eventually reaches the threshold required to embrittle even LAGBs [2, 16]. In every observed case where the LME crack traversed a LAGB, the stress normalisation factor of that LAGB exceeded that of the competing boundary at the same triple junction.

5.4.2. Misorientation angle vs Stress Normalisation factor

Figure 5.12 shows that the preference for the higher-misorientation boundary declines from 73% at 700 ms to 56% at 1700 ms, while the preference for the boundary with the higher stress normalisation factor increases from 58% to 93% over the weld time same range. The stress-assisted diffusion model of Klinger and Rabkin predicts that the diffusion flux along a GB scales with both the GB diffusivity and the normal stress acting on the boundary [16]. The GB diffusivity is an exponential function of GB energy, which in the HAGB regime is controlled principally by the excess free volume associated with the GB structure [6, 21]. At lower temperatures, the absolute GB diffusivity is lower across all GB types, and the relative difference in diffusivity between a high-energy and a lower-energy random HAGB is large enough to make misorientation a criteria that determines the crack path. A GB with a higher misorientation angle presents a structurally more open pathway for Zn penetration, such that the crack preferentially selects it even when the stress alignment is less favourable. This is consistent with the observation of Razmpoosh et al. that crack propagation in the Fe-Zn system is a function of both misorientation angle and the stress component perpendicular to the boundary plane, with misorientation acting as a necessary condition for penetration at low applied stress [9].

As weld time increases, peak HAZ temperatures rises. Mahadevan et al. showed in this same TWIP steel system that Zn diffusion distance ahead of LME cracks increases with weld time, with GB diffusion estimated to be approximately 30 times greater than bulk diffusion [27]. As temperature increases, the relative differences in diffusivity between competing random HAGBs of different misorientation angle narrow, because all boundaries in the HAGB regime share a qualitatively similar open atomic structure. The misorientation dependent difference that made one boundary a more preferred crack path than another at low weld times becomes less of a deciding factor when both boundaries are now above the diffusion threshold required for Zn penetration and intergranular decohesion.

Murugan et al. demonstrated that LME severity scales with the fraction of effective liquid Zn present at the moment of peak stress [23]. At higher weld times, the effective Zn fraction available at the weld shoulder increases. Once both competing boundaries at a triple junction are susceptible to Zn penetration, the mechanical driving force becomes the sole remaining discriminator. Boundaries more parallel to the loading axis experience a less compressive (or more tensile) normal stress, which both thermodynamically favours GB wetting per the condition $\gamma_{GB} > 2\gamma_{SL}$ and increases the stress-assisted Zn flux through the wedging mechanism described by Klinger and Rabkin [16, 17]. Gong et al. similarly observed that once a critical stress threshold is exceeded, the orientation of the boundary relative to the applied stress axis controls the depth and rate of liquid metal penetration, with boundaries parallel to the loading axis being least mechanically suppressed [10]. The two factors should therefore be understood not as competing explanations for LME crack path selection, but as sequential governing parameters whose relative effects shifts as the temperature of the process increases.

5.4.3. Proposed framework for LME GB susceptibility index

The GB structural character is a function of five independent macroscopic degrees of freedom: three parameters describing the crystallographic misorientation between adjacent grains, and two parameters describing the inclination of the boundary plane [28]. The present analysis captures the misorientation component through the misorientation axis-angle pair, and approximates the mechanical component through the angle relative to the loading direction. Both are projections of higher-dimensional quantities, which cannot directly be used to predict LME. The Read-Shockley model gives the GB energy $\gamma \propto \theta(A - \ln \theta)$, where A is a material constant that depends on elastic moduli and Burgers vector [28]. This function increases with θ up to approximately 15°, where the dislocation cores begin to overlap and the model breaks down. In the HAGB regime, GB energy no longer varies with misorientation angle alone and is also dependent on the misorientation axis. The depth and width of the energy minima at CSL orientations depend on the Σ value and the boundary plane orientation. For Σ3 coherent twin boundaries on the (111) plane, the energy approaches zero for perfectly coherent boundaries [28]. This has also been experimentally verified in Cu bicrystals by Wang et al [29]. Saylor et al. confirmed experimentally that the GB energy function shows Read-Shockley behaviour at small misorientations and a broad minimum near the Σ3 misorientation, and additionally found that the energy depends on the rotation axis [30]. The trends observed across all weld times and boundary types suggest that a unified predictive criterion for crack path selection at a triple junction is a useful direction for future work. Based on the present observations, such an index would need to incorporate at minimum: (i) the GB energy as a proxy for structural susceptibility to Zn penetration; (ii) a temperature-dependent Zn diffusivity term that scales with the excess free volume; and (iii) a mechanical stress normalisation factor capturing boundary alignment with the loading axis. The present study does not develop or validate such an index quantitatively; rather, it is proposed as a framework to guide future experimental and modelling efforts, informed by the trends identified here.

Several limitations would need to be acknowledged in applying such an index. The GB energy required as input is not measured for this specific TWIP steel HAZ microstructure and would need to be determined experimentally through five-parameter characterisation or atomistic simulation. Additionally, the relationship between GB energy and Zn diffusivity is taken from an empirical approximation that has been validated primarily in other FCC systems rather than Fe-Zn-Mn at RSW temperatures, and the relevant diffusion constants are not accurately calculated for the conditions studied here. The stress normalisation factor used throughout this study is a static approximation of what is in reality a transient, spatially varying stress tensor that evolves throughout the weld cycle [21]. Finally, the framework does not incorporate GB chemistry, which Razmpoosh et al. showed can independently modify embrittlement susceptibility through solute segregation [9]. Validating such an index quantitatively would require five-parameter GB characterisation to resolve boundary plane orientation, atom probe or STEM-EDS measurements of solute segregation at individual boundaries, and stress state calculations at individual GBs from crystal plasticity modelling rather than the macroscopic FEA stress field used in this study.

5.4.4. GB ENGINEERING FOR LME MITIGATION

The results of this study show that GB engineering (GBE) is a potential strategy to reduce LME susceptibility in TWIP steel. Across all six weld times investigated, Σ3 coherent twin boundaries were avoided by the LME crack, regardless of their orientation relative to the loading axis. This behaviour establishes that the structural resistance of Σ3 boundaries to liquid Zn penetration is not overcome by the mechanical driving force alone. Their near-zero excess free volume prevents the thermodynamic condition $\gamma_{GB} > 2\gamma_{SL}$ required for GB wetting from being satisfied under RSW conditions. The finding that non-Σ3 CSL boundaries (Σ5 – Σ41) similarly resisted LME at lower weld times, only becoming relevant at higher weld times at high stress normalisation factors, indicating that CSL GBs also offer a degree of structural protection.

GBE through thermomechanical processing (TMP) can be used to increase the fraction of low-Σ CSL boundaries through repeated cycles of small plastic pre-strain and subsequent annealing [31]. TMP drives strain-induced GB migration (SIBM) accompanied by annealing twin formation, which creates CSL boundaries and disrupts the connected random HAGB network [32]. Kokawa et al. demonstrated that an optimised TMP treatment in type 304 austenitic stainless steel maximises the CSL boundary fraction and produces a clear discontinuity in the corrosive random boundary network, arresting the propagation of intergranular attack from the surface [33]. Zhang et al. applied 5% compressive pre-strain to 316L austenitic stainless steel and showed that the special boundary fraction increased from 55% to 74% after annealing at 1273 K for 90 minutes, with the growing Σ9 and Σ27 boundary populations progressively replacing segments of the random HAGB network [34]. An LME crack cannot propagate indefinitely if the random boundary network is interrupted by clusters of CSL boundaries that are structurally impermeable to liquid Zn.

The present study demonstrates that the relative influence of GB misorientation on crack path selection reduces with increasing weld time: at 700 ms, higher misorientation boundaries are preferred in 73% of triple junctions, but falls to 56% at 1700 ms. At the highest weld times and heat inputs, the combination of temperature, Zn availability, and increased peak stresses at the weld periphery means that even non-Σ3 CSL boundaries become susceptible to LME. Practically, a GBE treatment would need to be integrated as a final heat treatment step after the conventional continuous annealing cycle, or designed as a modified annealing schedule compatible with galvanising operations, since standard continuous annealing produces a largely recrystallised microstructure. The LME susceptibility index framework proposed in the preceding section, which would incorporate GB energy, stress normalisation factor, and a temperature-dependent diffusivity term, could serve as a quantitative design target for such a process.

5.5. CONCLUSIONS

This study investigated the influence of GB misorientation and orientation relative to the loading axis on LME crack path in Zn-coated TWIP steel RSW across six weld times from 700 ms to 1700 ms. The following conclusions can be drawn:

- LME GBs were predominantly random HAGBs with misorientation angles of 35-55°. Σ3 coherent twin boundaries were LME-free at every weld time

investigated regardless of their orientation relative to the loading axis. Non-twin CSL boundaries (Σ5-Σ41) were predominantly LME-free at low weld times but progressively became LME GBs at higher weld times, at high stress normalisation factors and only when their stress factor exceeded that of the competing LME-free GB at the same triple junction.

- The fraction of triple junctions at which the LME GB had a higher stress normalisation factor than the competing LME-free GB increased from 58% at 700 ms to 91% at 1700 ms. Simultaneously, the preference for the higher misorientation GB reduced from 73% to 56%. LAGBs appeared as LME GBs only at high weld times and only at high stress normalisation factors.
- An LME GB susceptibility index is proposed that combines GB orientation and character, stress-assisted diffusion and a mechanical orientation factor. This framework provides a basis for interpreting the observed trends across all boundary types and weld times within a single predictive criterion, and could be a quantitative design target for GB engineering strategies aimed at reducing LME susceptibility in TWIP steel during RSW.

References

[1] G. Mahadevan, S. Sabooni, V. Popovich, L. A. I. Kestens and M. Hermans. 'Characterizing the effect of GB misorientation on liquid metal embrittlement crack path of resistance spot welded TWIP steel'. In: *Materialia* 48 (Aug. 2026), p. 102776. ISSN: 2589-1529. DOI: 10.1016/j.mtla.2026.102776. URL: https://www.sciencedirect.com/science/article/pii/S2589152926001286.

[2] E. E. Glickman. 'Dissolution Condensation Mechanism of Stress Corrosion Cracking in Liquid Metals: Driving Force and Crack Kinetics'. In: *Metallurgical and Materials Transactions A* 42.2 (1st Feb. 2011), pp. 250–266. ISSN: 1543-1940. DOI: 10.1007/s11661-010-0429-6.

[3] E. Glickman. 'Grain Boundary Grooving Accelerated by Local Plasticity as a Possible Mechanism of Liquid Metal Embrittlement'. In: *Interface Science* 11.4 (1st Oct. 2003), pp. 451–459. ISSN: 1573-2746. DOI: 10.1023/A:1026100112248.

[4] V. V. Popovich and I. G. Dmukhovskaya. 'Rebinder effect in the fracture of Armco iron in liquid metals'. In: *Soviet materials science : a transl. of Fiziko-khimicheskaya mekhanika materialov / Academy of Sciences of the Ukrainian SSR* 14.4 (1st July 1978), pp. 365–370. ISSN: 1573-885X. DOI: 10.1007/BF01154711.

[5] C. DiGiovanni, X. Han, A. Powell, E. Biro and N. Y. Zhou. 'Experimental and Numerical Analysis of Liquid Metal Embrittlement Crack Location'. In: *Journal of Materials Engineering and Performance* 28.4 (1st Apr. 2019), pp. 2045–2052. ISSN: 1544-1024. DOI: 10.1007/s11665-019-04005-2.

[6] Y. Hao, C. Tan, X. Yu, R. Chen, Z. Nie, Y. Ren, S. Yang, Y. Li and F. Wang. 'Effect of grain boundary misorientation angle on diffusion behavior in molybdenum-tungsten systems'. In: *Journal of Alloys and Compounds* 819 (5th Apr. 2020), p. 152975. ISSN: 0925-8388. DOI: 10.1016/j.jallcom.2019.152975.

[7] D. Bhattacharya, L. Cho, E. van der Aa, A. Pichler, N. Pottore, H. Ghassemi-Armaki, K. O. Findley and J. G. Speer. 'Influence of the starting microstructure of an advanced high strength steel on the characteristics of Zn-Assisted liquid metal embrittlement'. In: *Materials Science and Engineering: A* 804 (15th Feb. 2021), p. 140391. ISSN: 0921-5093. DOI: 10.1016/j.msea.2020.140391.

[8] M. H. Razmpoosh, B. Langelier, E. Marzbanrad, H. S. Zurob, N. Zhou and E. Biro. 'Atomic-scale Investigation of Liquid-Metal-Embrittlement Crack-path: Revealing Mechanism and Role of Grain Boundary Chemistry'. In: *Acta Materialia* 204 (1st Feb. 2021), p. 116519. ISSN: 1359-6454. DOI: 10.1016/j.actamat.2020.116519.

[9] M. H. Razmpoosh, A. Macwan, F. Goodwin, E. Biro and Y. Zhou. 'Crystallographic study of liquid-metal-embrittlement crack path'. In: *Materials Letters* 267 (15th May 2020), p. 127511. ISSN: 0167-577X. DOI: 10.1016/j.matlet.2020.127511.

[10] X. Gong, F. Hu, J. Chen, H. Wang, H. Gong, J. Xiao, H. Wang, Y. Deng, B. Pang, X. Huang, Y. Li and Y. Yin. 'Effect of temperature on liquid metal embrittlement susceptibility of an Fe10Cr4Al ferritic alloy in contact with stagnant lead-bismuth eutectic'. In: *Journal of Nuclear Materials* 537 (15th Aug. 2020), p. 152196. ISSN: 0022-3115. DOI: 10.1016/j.jnucmat.2020.152196.

[11] S.-H. Hong, J.-H. Kang, D. Kim and S.-J. Kim. 'Si effect on Zn-assisted liquid metal embrittlement in Zn-coated TWIP steels: Importance of Fe-Zn alloying reaction'. In: *Surface and Coatings Technology* 393 (15th July 2020), p. 125809. ISSN: 0257-8972. DOI: 10.1016/j.surfcoat.2020.125809.

[12] V. Bertolo, G. Mahadevan, R. H. Petrov and V. Popovich. 'The role of microstructure in crack growth during liquid metal embrittlement of Zn-galvanised TWIP steel'. In: *Journal of Materials Research and Technology* 38 (1st Sept. 2025), pp. 2569–2577. ISSN: 2238-7854. DOI: 10.1016/j.jmrt.2025.08.097.

[13] X. Wan, Y. Wang and P. Zhang. 'Numerical simulation on deformation and stress variation in resistance spot welding of dual-phase steel'. In: *The International Journal of Advanced Manufacturing Technology* 92.5 (1st Sept. 2017), pp. 2619–2629. ISSN: 1433-3015. DOI: 10.1007/s00170-017-0191-7.

[14] S. P. Murugan, V. Vijayan, C. Ji and Y. D. Park. 'Four types of LME cracks in RSW of Zn-coated AHSS'. In: *Weld J* 99.3 (2020), 75s–92s.

[15] S. P. Timoshenko, J. N. Goodier and H. N. Abramson. 'Theory of Elasticity (3rd ed.)' In: *Journal of Applied Mechanics* 37.3 (1st Sept. 1970), p. 888. ISSN: 0021-8936. DOI: 10.1115/1.3408648.

[16] L. Klinger and E. Rabkin. 'The effect of stress on grain boundary interdiffusion in a semi-infinite bicrystal'. In: *Acta Materialia* 55.14 (1st Aug. 2007), pp. 4689–4698. ISSN: 1359-6454. DOI: 10.1016/j.actamat.2007.04.039.

[17] T. Auger, S. Hémery, M. Bourcier, C. Berdin, M. Martin and I. Robertson. 'Crack path in liquid metal embrittlement: Experiments with steels and modeling'. In: *Frattura ed Integrita Strutturale* 10.35 (2016), pp. 250–259. ISSN: 1971-8993. DOI: 10.3221/IGF-ESIS.35.29.

[18] M. Arndt, P. Kürnsteiner, T. Truglas, J. Duchoslav, K. Hingerl, D. Stifter, C. Commenda, J. Haslmayr, S. Kolnberger, J. Faderl and H. Groiss. 'Multiscale Investigation of Microcracks and Grain Boundary Wetting in Press-Hardened Galvanized 20MnB8 Steel'. In: *Metals* 14.1 (29th Dec. 2023). ISSN: 2075-4701. DOI: 10.3390/met14010046.

[19] C. Zheng, L. Xu, X. Feng, Q. Huang, Y. Li, Z. Zhang and Y. Yang. 'Influence of Grain Orientation and Grain Boundary Features on Local Stress State of Cu-8Al-11Mn Alloy Investigated Using Crystal Plasticity Finite Element Method'. In: *Materials* 15.19 (7th Oct. 2022). ISSN: 1996-1944. DOI: 10.3390/ma15196950.

[20] C. Béal. 'Mechanical behaviour of a new automotive high manganese TWIP steel in the presence of liquid zinc'. Issue: 2011ISAL0029. Theses. INSA de Lyon, Mar. 2011.

[21] C. DiGiovanni, A. Ghatei Kalashami, E. Biro and N. Y. Zhou. 'Liquid metal embrittlement transport mechanism in the Fe/Zn system: Stress-assisted diffusion'. In: *Materialia* 18 (1st Aug. 2021), p. 101153. ISSN: 2589-1529. DOI: 10.1016/j.mtla.2021.101153.

[22] J.-U. Kim, S. P. Murugan, J.-S. Kim, W. Yook, C.-Y. Lee, C. Ji, J. B. Jeon and Y.-D. Park. 'Liquid metal embrittlement during the resistance spot welding of galvannealed steels: synergy of liquid Zn, α-Fe(Zn) and tensile stress'. In: *Science and Technology of Welding and Joining* 26.3 (1st Apr. 2021), pp. 196–204. ISSN: 1362-1718. DOI: 10.1080/13621718.2021.1880816.

[23] S. P. Murugan, J. Kim, J. Kim, Y. Wan, C. Lee, J. B. Jeon and Y.-D. Park. 'Role of liquid Zn and α-Fe(Zn) on liquid metal embrittlement of medium Mn steel: An ex-situ microstructural analysis of galvannealed coating during high temperature tensile test'. In: *Surface and Coatings Technology* 398 (25th Sept. 2020), p. 126069. ISSN: 0257-8972. DOI: 10.1016/j.surfcoat.2020.126069.

[24] Y. Chen, C. Wang and W. Xu. 'The Influence of Alloying Segregation on Zinc-Induced Embrittlement at the α/γ-Fe Interface'. In: *Metallurgical and Materials Transactions A* 53.5 (1st May 2022), pp. 1604–1612. ISSN: 1543-1940. DOI: 10.1007/s11661-022-06630-4.

[25] C. Beal, X. Kleber, D. Fabregue and M. Bouzekri. 'Embrittlement of a zinc coated high manganese TWIP steel'. In: *Materials Science and Engineering: A* 543 (1st May 2012), pp. 76–83. ISSN: 0921-5093. DOI: 10.1016/j.msea.2012.02.049.

[26] K.-D. Bauer, M. Todorova, K. Hingerl and J. Neugebauer. 'A first principles investigation of zinc induced embrittlement at grain boundaries in bcc iron'. In: *Acta Materialia* 90 (15th May 2015), pp. 69–76. ISSN: 1359-6454. DOI: 10.1016/j.actamat.2015.02.018.

[27] G. Mahadevan, V. Bertolo, S. Sabooni, V. Popovich, L. A. I. Kestens and M. Hermans. 'Characterizing zinc diffusion during liquid metal embrittlement of resistance spot welded TWIP steel'. In: *Welding in the World* (10th Feb. 2026). ISSN: 1878-6669. DOI: 10.1007/s40194-026-02384-4.

[28] Humphreys and Hatherley. *The Structure and Energy of Grain Boundaries*. DOI: 10.1016/B978-008044164-1/50008-6.

[29] J. Wang, N. Li and A. Misra. 'Structure and stability of Σ3 grain boundaries in face centered cubic metals'. In: *Philosophical Magazine* 93.4 (1st Feb. 2013). _eprint: https://doi.org/10.1080/14786435.2012.716908, pp. 315–327. ISSN: 1478-6435. DOI: 10.1080/14786435.2012.716908.

[30] D. M. Saylor, A. Morawiec, B. L. Adams and G. S. Rohrer. 'Misorientation Dependence of the Grain Boundary Energy in Magnesia'. In: *Interface Science* 8.2 (1st Aug. 2000), pp. 131–140. ISSN: 1573-2746. DOI: 10.1023/A:1008764219575.

[31] C. Takushima, J.-i. Hamada and S. Tsurekawa. 'Rapid Achievement of High Frequency of CSL Boundaries in Austenitic Stainless Steel via Reduced Stacking Fault Energy'. In: *ISIJ International* 65.1 (2025), pp. 133–141. DOI: 10.2355/isijinternational.ISIJINT-2024-259.

[32] F. Shi, X. Li, Y. Hu, C. Su and C. Liu. 'Optimization of grain boundary character distribution in Fe-18Cr-18Mn-0.63N high-nitrogen austenitic stainless steel'. In: *Acta Metallurgica Sinica (English Letters)* 26.5 (1st Oct. 2013), pp. 497–502. ISSN: 2194-1289. DOI: 10.1007/s40195-013-0323-5.

[33] H. Kokawa, M. Shimada, Z. J. Wang, Y. S. Sato and M. Michiuchi. 'Grain Boundary Engineering for Intergranular Corrosion Resistant Austenitic Stainless Steel'. In: *Key Engineering Materials* 261-263 (2004), pp. 1005–1010. ISSN: 1662-9795. DOI: 10.4028/www.scientific.net/KEM.261-263.1005.

[34] M. Zhang, C. Zhang, H. Wu and B. Yang. 'Effects of Grain Boundary Engineering on the Microstructure and Corrosion Fatigue Properties of 316L Austenitic Stainless Steel'. In: *Frontiers in Materials* 9 (29th June 2022). ISSN: 2296-8016. DOI: 10.3389/fmats.2022.931848.

6

Quantifying Zinc Diffusion Ahead of LME Cracks

Liquid Metal Embrittlement during RSW of TWIP steel is primarily driven by stress-assisted GB diffusion of Zn. Although GB diffusion is widely recognized as the dominant LME mechanism, experimental quantification is challenging due to resolution limitations. This study characterizes Zn diffusion in TWIP steel during RSW by conducting Energy Dispersive X-ray Spectroscopy (EDS) line scans ahead of LME cracks in both the rolling direction (RD) and normal direction (ND) over weld times from 700 ms to 1700 ms. Results reveal that Zn diffusion distance increases with weld time, with consistently higher diffusion in the ND. To compare experimental measurements with diffusion theory, an FEA simulation based on Fick's law was employed to approximate bulk Zn diffusion under varying temperatures. The model predicts Zn diffusion trends consistent with experimental observations. Although the diffusion distance predicted in the simulation exceeds measured values, directional trends are accurately captured. A theoretical framework to compare GB and bulk diffusion was proposed. GB diffusion distance of Zn is estimated to be approximately 30 times greater than bulk diffusion, establishing a quantitative link between weld time and Zn diffusion during RSW of TWIP steel.

6.1. Introduction

The materials context for this study, including the properties of TWIP steel, the role of Zn coatings, and the RSW process, is described in Chapter 2. This chapter builds directly on that foundation to address the relationship between RSW weld time and the distance of Zn diffusion ahead of LME cracks. Multiple studies have shown TWIP steel to have a high susceptibility for LME despite its superior strength and ductility [2–4]. The complexity of LME is increased by the inhomogeneous stresses, temperatures

Parts of this chapter have been published in Welding in the World, Volume 70 (2026) [1].

and microstructure across different regions of the spot weld. These variations lead to the formation of different types of LME cracks in different areas of the weld [5]. A number of theories have been proposed to explain the micro-mechanisms behind LME. These micro-mechanisms vary depending on the combination of metals in the LME system. For Fe-Zn, stress-assisted GB diffusion has been observed to be the most likely micro-mechanism [6, 7]. The 'Rehbinder effect' underpins most of the proposed models for stress-assisted LME, which proposes that the liquid Zn penetrates the grain boundaries and reduces the surface energy of the steel which drives the embrittlement above a critical level of stress [8]. Multiple characterization studies have been performed on RSW showing LME in order to understand the effects of microstructure and temperature on crack initiation and propagation [8–12]. These studies have quantitatively characterized Zn diffusion during LME. Kang et al. used STEM analysis to investigate Zn distribution along GBs ahead of LME crack tips and reported localized Zn penetration. While these measurements provide direct evidence of Zn penetration along GBs, they are limited to individual line scans at selected locations and cannot be extended across a wide range of welding parameters due to the complexity of sample preparation and the time intensive nature of high resolution characterization [13]. Similarly, Ling et al. attempted to quantitatively measure Zn content in LME-affected regions; however, limitations in characterization resolution prevented reliable quantification of Zn diffusion along GBs [10]. RSW process parameters also have an effect on LME, with studies showing that LME is more severe when the welding heat input is higher, resulting in more severe LME when the welding current or weld time is increased [8, 12, 14, 15]. While studying LME severity by analysing the number of cracks and crack dimensions is useful, it offers an incomplete picture because it does not account for the underlying Zn diffusion mechanisms that drive crack formation and propagation [16]. Characterizing the overall Zn diffusion, particularly its interaction with stress and temperature gradients, is crucial for a more comprehensive understanding of LME. Klinger et al. proposed a "diffusion wedge" theory, which describes how the embrittling species diffuses along grain boundaries ahead of an LME crack, forming a wedge-like concentration profile. This theory provided a mathematical framework linking stress, temperature, GB and bulk diffusion [16]. Dohie et al. developed an empirical model on Zn diffusion in α-Fe based on experimental observations. While this model predicted the temperature dependent diffusion constants of Zn in α-Fe, it did not account for the effect of stress on Zn diffusion [17]. DiGiovanni et al. investigated the influence of stress on Zn diffusion that formulated a modification of the Fisher equation for GB diffusion to account for the contribution of stress, that also incorporated the model developed by Klinger et al. [11, 18]. Although the variation on Zn diffusion with stress was investigated in the study by DiGiovanni et al., the influence of temperature was not experimentally validated.

The presence of liquid Zn at the crack tip and the solid state diffusion of Zn ahead of the crack tip are recognized as the most critical steps governing LME. However, there has been a lack of detailed characterization studies linking weld time to the diffusion of Zn ahead of the crack tip. GB diffusion, although dominant in LME mechanisms, is challenging to measure experimentally due to the limited resolution of techniques like Energy Dispersive X-Ray Spectroscopy (EDS), which cannot reliably capture

Zn concentrations along narrow GB regions. Since GB diffusion and bulk diffusion are related through established models, such as Fisher's model [18], analysing bulk diffusion enables an indirect understanding of GB diffusion. Although previous studies systematically investigate the effect of welding process parameters on LME, the severity of embrittlement is only quantified by the number of cracks and crack depth and not on their effect on the microstructure or mechanism governing LME [8]. Moreover, most of the characterization studies induce LME on the steel samples using high temperature thermo-mechanical testing [2, 13, 19, 20]. Although this technique is useful in studying LME, it does not accurately replicate the inhomogeneous temperature, stress or microstructural conditions during RSW, which strongly affects crack propagation [21]. The main goal of the research presented here is to systematically study the effect of welding time on the diffusion of Zn ahead of the crack tip during RSW. Understanding the effect of weld time on Zn diffusion would thus lead to a better understanding of LME mechanisms and the design of the welding process that could result in reducing LME susceptibility.

This study investigates the influence of RSW weld time on Zn diffusion by comparing Zn diffusion profiles ahead of the crack tip in the rolling direction (RD) and normal direction (ND) relative to the sample at different weld times. By examining diffusion behaviour in different directions and utilizing measurable bulk diffusion data, this study establishes a link between weld parameters, stress distribution, and Zn diffusion in the context of LME mechanisms. Additionally, a simplified 2D analytical diffusion model is used to evaluate the comparative trends of Zn diffusion in the RD and ND directions and to provide a simple framework to compare experimentally measured bulk Zn diffusion distances under varying weld conditions. The purpose of this model is not to reproduce the exact diffusion process, but rather to validate the general trends in Zn diffusion distances at different RSW weld times. Although previous studies have investigated the effect of weld time on LME during RSW, this is the first quantitative study linking RSW weld time and Zn diffusion distance of TWIP steel. The novelty of this study is in the extensive range of weld times studied and the quantitative link established between GB and bulk Zn diffusion for Fe-Zn systems.

6.2. Materials and methods

The materials used, the RSW setup and the process parameters are further elaborated on in Chapter 6.2.

6.2.1. Characterization

A VHX7000N optical microscope was used to identify LME cracks on the surface of the spot weld. These crack locations were used to select the areas to perform cross-section analysis. Once the cracks were identified, they were sectioned with the cutting plane passing through the middle of the crack. To prepare the samples for SEM analysis, the cross-sections were ground using progressively finer sandpaper and then polished sequentially with a 3 µm silica paste followed by a 1 µm diamond paste to achieve a smooth surface suitable for imaging and microscopy. Scanning Electron Microscopy

(SEM) was conducted with a JEOL IT800SHL™ equipped with a field emission gun at 10 kV and 3.2 nA beam current. The SEM system can perform Energy Dispersive X-ray Spectroscopy (EDS) with an Oxford Instruments® Maxim 100™ detector. The primary objective of the EDS analysis was to investigate the bulk diffusion of Zn from the crack tip into the surrounding steel grains. This served two purposes: (a) to study the influence of weld time on Zn diffusion and LME cracking behaviour (b) to validate the theoretical framework of stress-assisted diffusion. As illustrated in Figure 6.1, EDS line scans were conducted in two principal directions relative to the sample reference system: the normal direction (ND) and the rolling direction (RD). All cracks were observed to propagate perpendicular to the weld surface along the ND. The line scans aimed to capture and compare the Zn diffusion profiles along these directions to identify any directional differences in the bulk diffusion behaviour. SEM was used to measure the width and depth of LME cracks. The width was measured at the crack opening and the depth was measured from the surface crack opening to the crack tip, as shown in Figure 6.2.

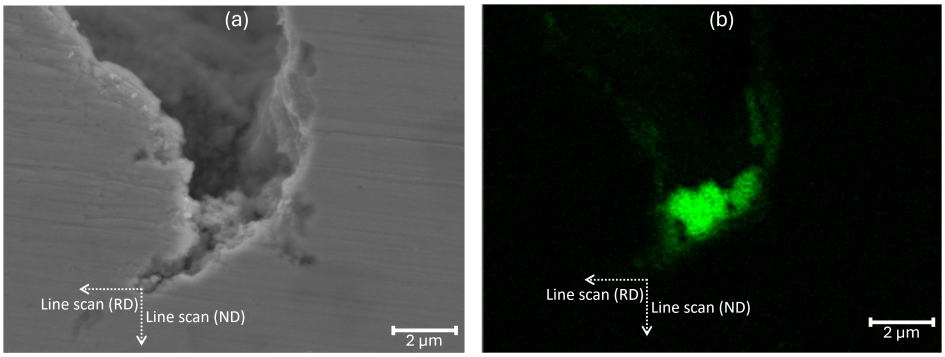


Figure 6.1: (a) SEM micrograph of a representative LME crack tip illustrating EDS line scan directions relative to the sample coordinate system (b) EDS map showing distribution of Zn in the LME crack illustrating EDS line scan directions relative to the sample coordinate system

6.2.2. Numerical modelling framework

The purpose of this simulation is to approximate the bulk diffusion of Zn at different temperatures and compare the resulting diffusion profiles with those measured at LME cracks from RSW tests at varying weld times. Theoretical line scans of Zn concentration in both the ND and RD from the crack tip are calculated based on solving the 2D diffusion equation using a continuum finite element formulation of Fick's second law [22] and compared with experimentally obtained EDS line scans of Zn bulk diffusion ahead of the crack tip. The model assumes that the LME crack remains fully filled with liquid Zn, acting as an infinite reservoir for diffusion, ensuring a constant Zn concentration at the crack interface. The crack dimensions are fixed throughout the simulation, focusing solely on bulk diffusion rather than dynamic crack propagation. The formation of Fe-Zn intermetallic phases is also not included in the model, allowing for a direct evaluation of

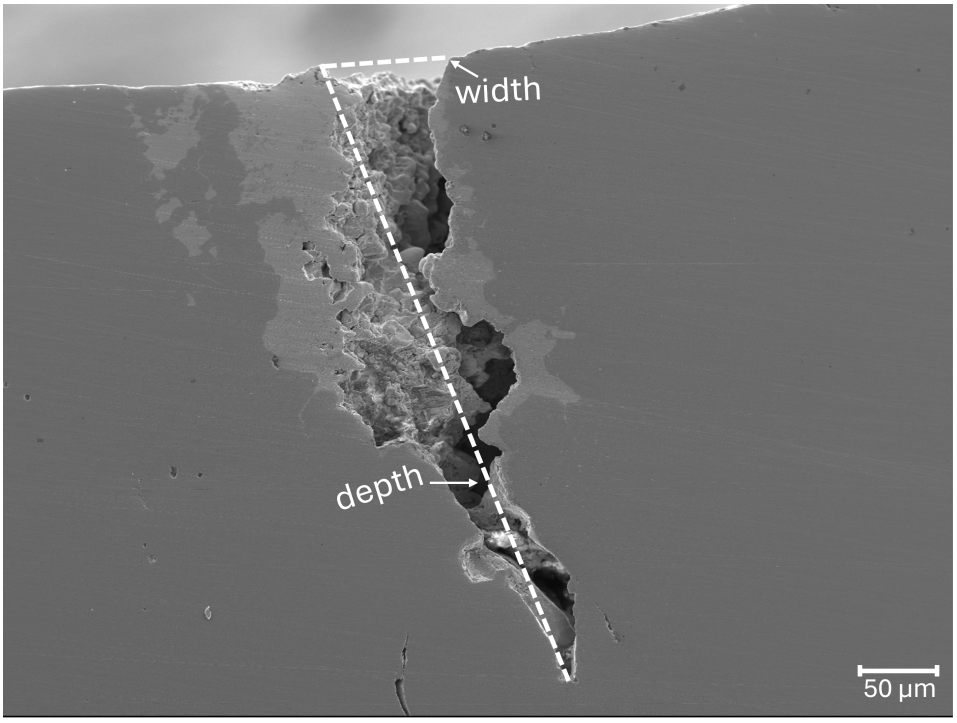


Figure 6.2: Schematic measurement of LME crack width and depth from the weld surface. The crack depth (indicated by the white line) is measured from the surface opening to the crack tip in the cross-section

Zn diffusion in the steel matrix. This simplification was necessary to isolate and compare bulk diffusion trends without the added complexity of dynamic phase transformations or material loss.

Initial and boundary conditions

The simulation grid consisted of 10000 x 10000 points, corresponding to a spatial resolution of $\Delta x = \Delta y = 0.1$ µm. For the initial condition, an LME crack is simulated as a triangular wedge filled with Zn as shown in Figure 6.3. In the initial condition, the concentration of Zn in the coating and the crack is taken to be 100% and the steel to be 0%. The temporal evolution of Zn concentration was computed using time steps of $\Delta t = 1$ ms with the total simulation time set to match the welding process duration. The temperature and stress values are obtained from prior experimental research by Murugan et al. [5]. According to Murugan et al., the temperature at the region of the LME cracks observed in the current study is between 650 □ and 1000 □, and the maximum stress experienced in this region is 200 MPa. Lower weld times (for example, 700 ms) were represented in the model by temperatures around 650-700 °C, while

longer weld times (such as 1700 ms) corresponded to higher temperatures of about 850-900 °C. Although direct temperature measurements were not calculated for each weld time, the selected range represents realistic welding conditions to capture how Zn diffusion changes with increasing temperature. Since the boiling temperature of Zn is 907 □, temperatures higher than that were not considered in the simulation, as no more liquid Zn would be available for LME.

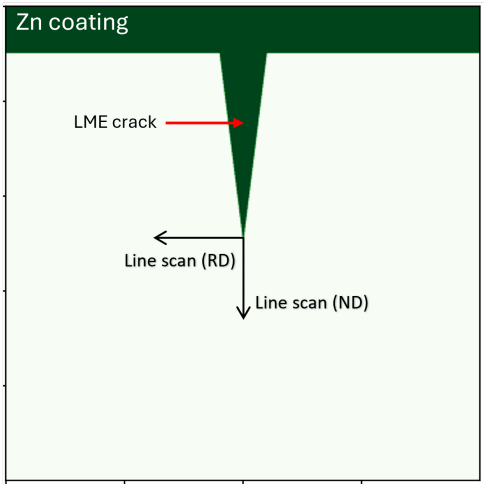


Figure 6.3: Initial condition for Zn diffusion simulation with theoretical line scans in RD and ND directions

The diffusion constant was calculated using the Arrhenius relationship in:

$$D_{\text{eff}} = D_0 \exp\left(-\frac{Q}{RT}\right) \tag{6.1}$$

where D_0 is the pre-exponential diffusion factor, Q is the activation energy, T is the absolute temperature and R is the gas constant. The DICTRA package in ThermoCalc software was used to obtain values for D_0 and Q for Zn in FCC-Fe.

Bulk diffusion modelling

The diffusion of Zn from the crack tip into the steel substrate was modelled using Fick's second law:

$$\frac{C}{t} = \cdot (D_{\text{eff}} C) \tag{6.2}$$

where C is the Zn concentration, t is time, and D_{eff} is the effective diffusion coefficient. The model assumes that the crack is fully filled with liquid Zn, which acts as an infinite source for diffusion, and that the length of the crack remains constant throughout the simulation. The formation of intermetallic phases at the Zn-steel interface is neglected.

6.2.3. Effect of stress

Stress influences diffusion by altering the chemical potential gradient, which in turn affects the flux of diffusing species [23]. The chemical potential is given by:

$$\mu = \mu^0 + RT \ln C + \frac{\Omega\sigma}{RT} \tag{6.3}$$

where μ^0 is the reference chemical potential, R is the gas constant, T is the temperature, σ is the stress, and Ω is the atomic volume. Differentiating this expression results in a modified diffusion flux equation, where the flux J is given as:

$$J = -D\left(C + \frac{\Omega}{RT} C\sigma\right) \tag{6.4}$$

Substituting this to modify Fick's second law as:

$$\frac{C}{t} = \cdot(DC) + \cdot\left(\frac{D\Omega}{RT} C\sigma\right) \tag{6.5}$$

Thus, when a stress gradient is present, the effective diffusion constant D_{eff} can be written as:

$$D_{\text{eff}} = D_0 \exp\left(\frac{-Q}{RT}\right) \exp\left(\frac{\Omega\sigma}{RT}\right) \tag{6.6}$$

The contribution of the applied stress to the effective diffusion constant is $\Omega\Delta\sigma/RT$, which can be calculated by substituting D_0 = 1.2 x $10^{-5} m^2/s$ (DICTRA), Q = 155522 J/mol (DICTRA), R=8.314 J/mol.K, T = 1080 K which is the boiling temperature of Zn and the highest temperature that LME can occur, Ω = 1.18 x 10-29 m^3 (ThermoCalc) and $\Delta\sigma$ = 200 MPa. It is important to clarify that Murugan et al. specifies 200 MPa is the stress and not the stress gradient [5]. This stress value was conservatively used as an upper bound estimate for □σ to evaluate the possible magnitude of stress-assisted diffusion effects. This approach likely overestimates the gradient and therefore provides a conservative estimate showing that stress contributions to bulk diffusion remain negligible. The term $\Omega\Delta\sigma/RT$ can thus be calculated as $2.92x10^{-25}$, which is so negligible that it can be ignored completely from bulk diffusion calculations. Although stress has an important role to play in GB diffusion of Zn ahead of the crack tip [24], it has a negligible effect on the bulk diffusion which is the focus of this study and can thus be ignored in the numerical simulation of bulk Zn diffusion. Local stress concentrations near the crack tip promote atomic transport along GBs by altering chemical potential gradients. Thus, even though bulk diffusion is largely unaffected by stress in the current model, stress-assisted GB diffusion is recognized as the principal mechanism driving Zn transport and crack propagation during LME.

6.3. Results

SEM characterization was performed on all RSW samples, with the cross-section of the LME cracks at various weld times presented in Figure 6.4. Most samples exhibited a single crack, with multiple cracks observed only at a WT of 1700 ms. The cracks were

all identified as Type B cracks [5], which are typically associated with the weld shoulder region as shown in Figure 6.5

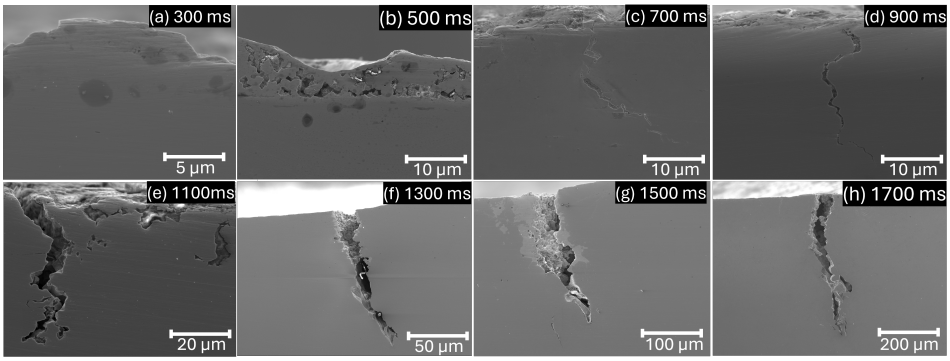


Figure 6.4: SEM micrographs of LME cracks at weld time of (a) 300 ms (b) 500 ms (c) 700 ms (d) 900 ms (e) 1100 ms (f) 1300 ms (g) 1500 ms (h) 1700 ms

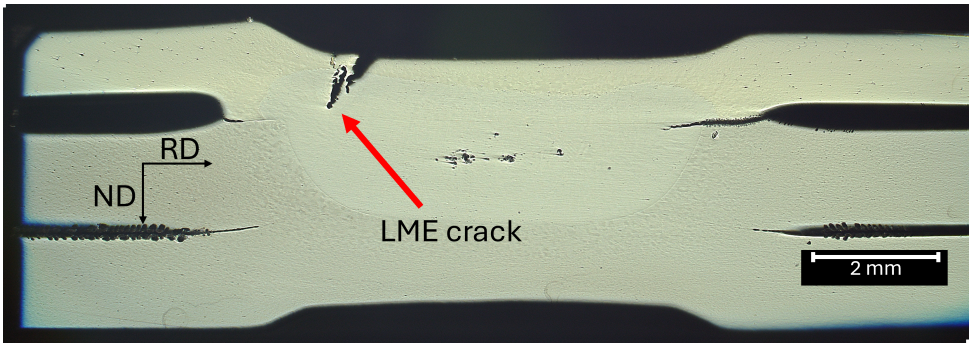


Figure 6.5: Representative optical micrograph of weld cross-section at WT=1700 ms showing a typical LME crack in the weld shoulder region

The average crack depth and width were found to increase with increasing weld time, as shown in Figure 6.6. The crack width is measured at the opening of the crack. This trend suggests that longer weld times increase the severity of LME, possibly due to prolonged exposure to elevated temperatures and stress conditions that promote crack initiation and propagation. Cracks were not observed in samples welded for shorter durations (300 ms and 500 ms), indicating that a critical combination of temperature, stress, and time is required for LME crack formation. The average weld nugget area was measured for each weld time, as shown in the schematic diagram presented in Figure 6.7. The average weld nugget area is presented in Table 6.1. It is important to note that the nugget area could not be calculated for WT = 300 ms because the bottom DX54 sheet did not form a part of the spot weld. The heat input at this weld time was too

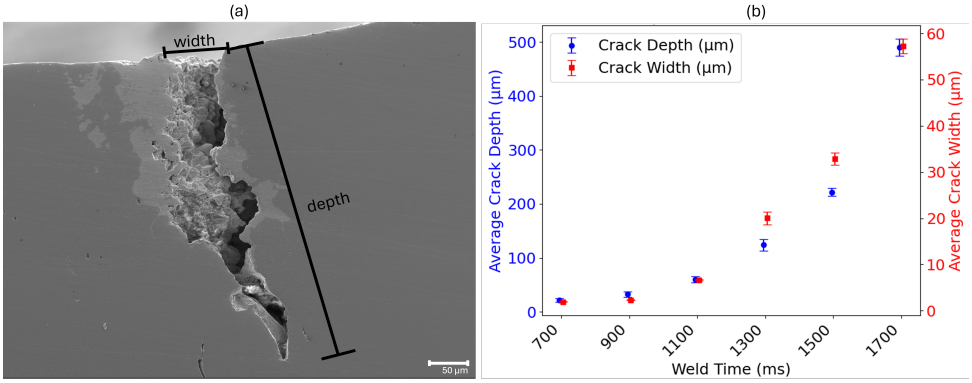


Figure 6.6: (a) Crack measurement methodology (b) Average LME crack depth and crack width at different weld times

low to sufficiently form a weld nugget at the DX54-DX54 interface. Previous studies have established that LME severity increases with increasing weld time, caused by increasing the heat input [25]. The insufficient heat input at the lower weld times of 300 and 500 ms in this study could explain the lack of observable LME.

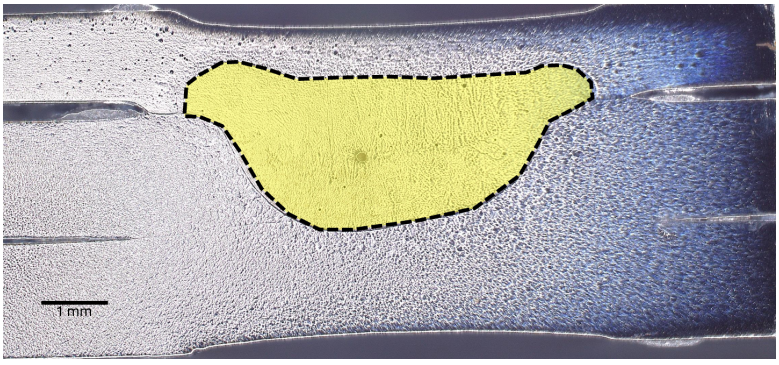


Figure 6.7: Schematic optical microscopy cross-section for weld nugget area measurement at WT = 700 ms

6.3.1. EDS Analysis

EDS line scans were performed for all samples with LME cracks at RSW weld times ranging from 700 ms to 1700 ms. Zn line scans were taken in the RD and ND directions, as described in Section 6.2.1. Zn diffusion profiles ahead of the crack tip in these directions were obtained, as shown in Figure 6.8 for a single sample. The Zn diffusion distance, defined as the distance from the crack tip where the Zn concentration drops to zero, was calculated from these profiles. The results show a strong correlation between RSW weld time and Zn diffusion distance, with longer weld times leading to increased

Table 6.1: Average weld nugget area for different weld times

Weld time (ms)	Average weld nugget area (mm^2)
300	NA
500	6.52 ± 0.23
700	9.57 ± 0.38
900	10.43 ± 0.42
1100	11.24 ± 0.65
1300	11.93 ± 0.59
1500	12.71 ± 0.82
1700	13.36 ± 0.76

Zn diffusion distances in both RD and ND directions. While this result can be predicted by diffusion theory, it has not been experimentally verified in previous studies on RSW or LME. Figure 6.8 compares Zn diffusion in the RD and ND directions at different weld times for a single set of weld times, and Figure 6.9 presents the average Zn diffusion distances across different weld times. In the ND, the average Zn diffusion distance is 0.55 ± 0.01 µm at WT = 700 ms, 0.65 ± 0.01 µm at WT = 900 ms, 1.08 ± 0.07 µm at WT = 1100 ms, 1.63 ± 0.12 µm at WT = 1300 ms, 2.56 ± 0.14 µm at WT = 1500 ms and 3.09 ± 0.11 µm at WT = 1700 ms. In the RD, the average Zn diffusion distance is 0.42 ± 0.02 µm at WT = 700 ms, 0.51 ± 0.02 µm at WT = 900 ms, 0.75 ± 0.05 µm at WT = 1100 ms, 1.34 ± 0.08 µm at WT = 1300 ms, 2.05 ± 0.08 µm at WT = 1500 ms and 2.51 ± 0.14 µm at WT = 1700 ms. In all cases, the diffusion distance in the ND is greater than in the RD, as indicated in Table **??**.

6.3.2. Comparison of EDS measurements with diffusion simulations

2D diffusion modelling was performed following the methodology described in Section 6.2.2. These simulations generated theoretical Zn diffusion profiles in the RD and ND directions from the crack tip, analogous to the experimental EDS line scans. The diffusion profiles were modelled at temperatures of 650 °C, 700 °C, 750 °C, 800 °C, 850 °C, and 900 °C, as shown in Figure 6.10. While these temperatures do not directly correspond to the weld times ranging from 700 ms to 1700 ms, they represent a similar trend, as higher weld times are associated with increased temperatures. The objective of this comparison is to assess whether the predicted diffusion profiles from the simulations align in magnitude with the experimentally measured Zn diffusion distances. The simulation results revealed trends that are consistent with the EDS measurements by comparing the plot in Figure 6.8 and Figure 6.10. An increase in temperature leads to a greater Zn diffusion distance, similar to the observed relationship between weld time and Zn diffusion in the experimental results. Additionally, the simulations confirm that Zn diffusion distances in the ND direction are consistently greater than in the RD direction, as shown in Figure 6.11.

The ratio of diffusion distances between the ND and RD in the simulations closely matches the experimentally observed ratios - the ratio of the average ND/RD diffusion

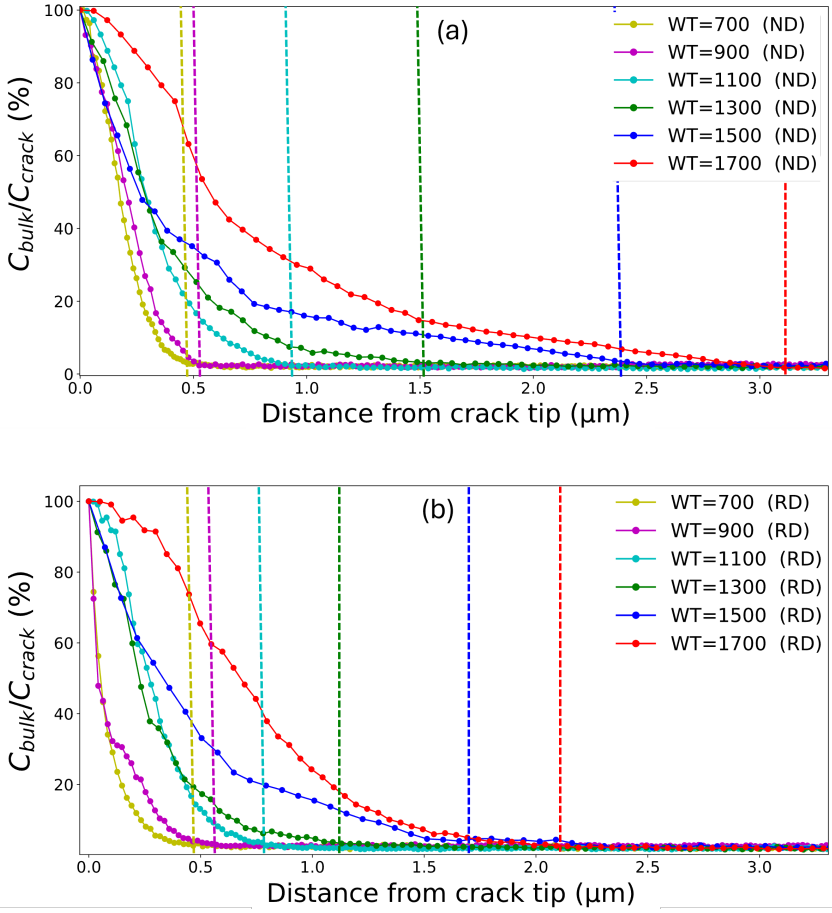


Figure 6.8: EDS Zn line scans ahead of the crack in the (a) ND direction (b) RD direction, with the dotted lines showing Zn diffusion distance for each weld time

distance for the experimentally measured EDS plots is 1.29 ± 0.09 and the same ratio for the simulated diffusion profiles is 1.42 ± 0.08. This suggests that while the model may overestimate Zn diffusion distances, it captures the relative directional differences in diffusion behaviour. A comparison of the measured and simulated Zn diffusion distances is presented in Table **??**. These values were taken from the Zn diffusion distance measurements from Figure 6.8 and the simulated Zn diffusion distances shown in Figure 6.11.

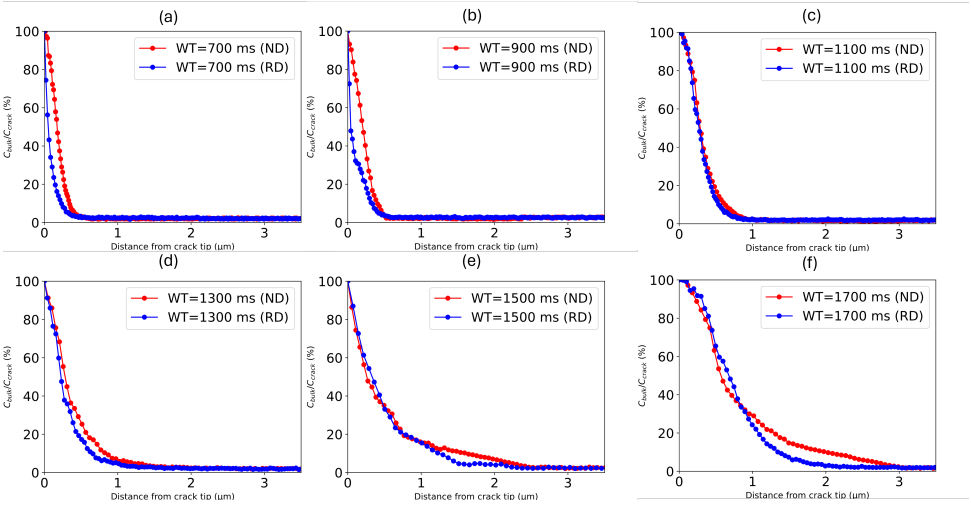


Figure 6.9: Comparing Zn diffusion profiles in ND (red) and RD (blue) directions for one set of RSW samples at a weld time of (a) 700 ms (b) 900 ms (c) 1100 (ms) (d) 1300 ms (e) 1500 ms (f) 1700 ms

Table 6.2: Comparison between experimentally measured and numerically simulated Zn diffusion distances

Experimentally measured results			**FEA results**		
Weld time (ms)	Average Zn diffusion distance RD (μm)	Average Zn diffusion distance ND (μm)	Temper-ature □	Predicted diffusion distance RD (μm)	Predicted diffusion distance ND (μm)
700	0.42 ± 0.02	0.55 ± 0.01	650	0.4	0.6
900	0.51 ± 0.02	0.65 ± 0.01	700	0.8	1.2
1100	0.75 ± 0.05	1.08 ± 0.07	750	1.3	1.8
1300	1.34 ± 0.08	1.63 ± 0.12	800	1.9	2.7
1500	2.05 ± 0.08	2.56 ± 0.14	850	2.7	4
1700	2.51 ± 0.14	3.09 ± 0.11	900	4.1	5.2

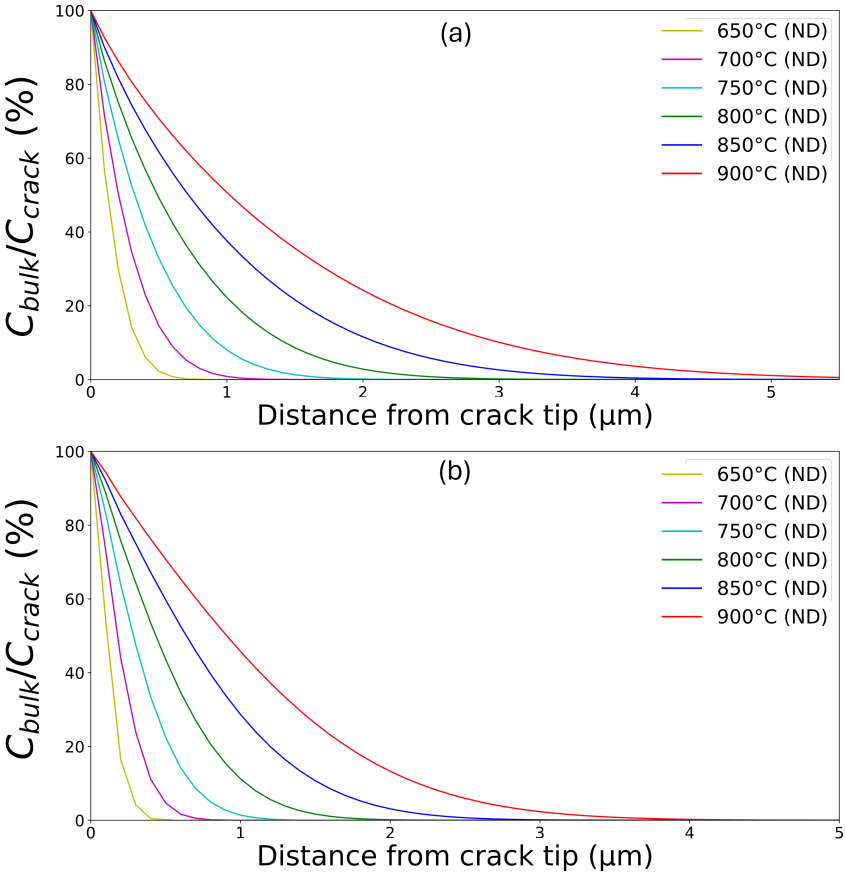


Figure 6.10: Simulated diffusion profiles of Zn from the crack tip at different temperatures in the (a) ND direction (b) RD direction

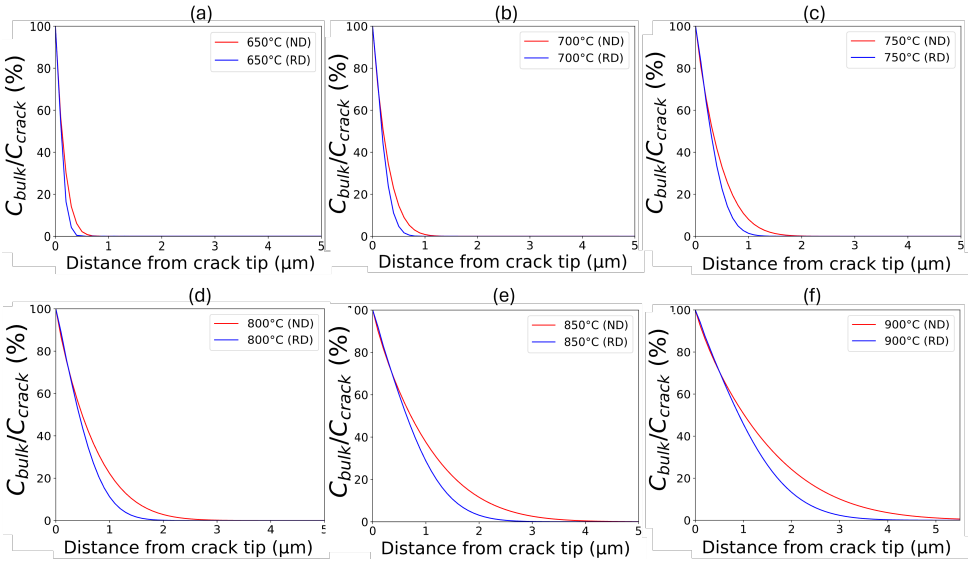


Figure 6.11: Simulated overlapping Zn diffusion profiles in the RD and ND directions from a theoretical LME crack at (a) 650°C (b) 700°C (c) 750°C (d) 800°C (e) 850°C (f) 900°C

6.4. Discussion

The analysis of LME crack geometry at different weld times shown in Figure 6.2 indicates that crack depth increases with increasing weld time. No cracks were observed in samples welded at 300 ms and 500 ms, suggesting that a minimum threshold of temperature and stress is required for LME initiation. The weld nugget size measurements presented in Table 3 show that the nugget area increases with weld heat input, which leads to more severe LME cracking [19]. This increase in LME severity with increasing heat input has also been observed in other studies.

All observed cracks were located in the weld shoulder region which is consistent with previous studies, suggesting that the heterogeneous temperature and stress conditions in this region accelerate LME crack initiation and propagation [5, 26]. Type C cracks reported in other studies on Zn-coated TWIP steels (e.g. by Murugan et al [5]) were not observed in the present work. This may be attributed to differences in welding conditions and joint configuration, particularly the use of a triple-stack weld with a heterogeneous material stack, which can alter local temperature gradients and stress distributions. It is possible that these cracks might be observed for the same welding conditions if more samples were analysed

6.4.1. Comparison between EDS and diffusion modelling

Figures 6.9 and 6.11 summarizes the experimentally measured Zn diffusion distances compared with the FEA predictions. These results show that both results are of the same order of magnitude - the ratio of the average ND/RD diffusion distance for the experimentally measured EDS plots is 1.29 ± 0.09 and the same ratio for the simulated diffusion profiles is 1.42 ± 0.08. The model validates directional trends and differences in diffusion between RD and ND but not the exact diffusion distances, which could be attributed to several factors. One possible source of discrepancy is the accuracy of thermodynamic data from ThermoCalc, which does not fully account for the effects of alloying elements and non-equilibrium conditions present during RSW. During RSW, the TWIP steel experiences rapid heating and cooling and nonequilibrium segregation of alloying elements such as Mn and Al. These conditions can significantly reduce the actual diffusivity of Zn compared to equilibrium predictions. As a result, the model likely overestimates diffusion distances because it assumes steady-state diffusivity values that are higher than those occurring in the spot weld. Microstructural variations such as local grain orientation and GB characteristics may introduce deviations between simulated and experimental diffusion profiles [30]. For example, GB misorientation has been observed to affect the diffusivity of alloying elements in steel. The degree of misorientation influences segregation behaviour, where certain alloying elements preferentially segregate to high-energy boundaries, locally modifying diffusion kinetics [27]. The presence of Fe-Zn intermetallics may also affect the diffusion of Zn into the steel substrate. The formation of Fe-Zn intermetallic compounds (such as Fe_3Zn_{10} and $FeZn_{10}$) at the steel-Zn interface acts as a barrier to Zn transport. These intermetallic layers trap Zn atoms and limit further diffusion into the matrix [28, 29]. The simulation neglects intermetallic phase formation and treats the Zn-steel interface as a pure diffusion boundary, and does not capture the reduction in effective diffusion flux,

leading to overestimated diffusion distances. The EDS results indicate that Zn diffusion distances in the ND direction are consistently greater than in the RD direction. This can be attributed to the nature of 2D diffusion and the initial conditions of the crack geometry. With a triangular crack propagating in the ND, the fundamental diffusion model predicts greater Zn penetration in this direction compared to the RD. Although the stress state differs between ND and RD, it does not influence the magnitude of bulk Zn diffusion, as demonstrated in Section 6.2.3. It is also possible that the EDS measurements capture Zn from grain boundaries in addition to bulk diffusion in the line scans. However, the spatial resolution of EDS is limited by a spot size of approximately 1 µm, while the typical GB width is on the order of a few nanometres [18]. Even if Zn segregates strongly at GBs, the signal from these nanometre-scale regions contributes less than 0.5% to the total volume sampled by the EDS beam. Therefore, the obtained line scans predominantly reflect Zn concentrations within the bulk grains rather than along GBs. This quantitative difference explains why the measured profiles correspond to bulk diffusion behaviour, while GB diffusion must be inferred indirectly [30, 31]. The directional dependence of Zn diffusion highlights the importance of crack geometry and diffusion pathways in governing Zn transport in LME-affected regions.

6.4.2. Bulk and GB diffusion of Zn

Stress-assisted GB diffusion has been identified as the dominant mechanism for LME in the Fe-Zn system. According to the ”diffusion wedge” theory proposed by Klinger et al, Zn atoms diffuse preferentially along GBs under LME conditions while also diffusing into the bulk material. The study proposed a mathematical formulation that describes the relationship between GB and bulk diffusion, stress, and the resulting concentration profiles within the diffusion wedge. The shape of this wedge are governed by the GB energy, time and the applied stress [16]. Experimental EDS analysis presented in Section 6.3.2 measures the Zn diffusion distance for different weld times that correspond to different temperatures and stress states. While direct measurement of GB diffusion is challenging, the analytical description of the diffusion wedge from Klinger et al. provides a way to estimate GB diffusion behaviour indirectly using the experimentally obtained bulk diffusion data. The mathematical formulation proposed by Klinger et al. was incorporated in the study by DiGiovanni et al., who modelled stress-assisted GB diffusion of Zn based on Fisher’s model of GB diffusion [11]. Their formulation describes the evolution of Zn concentration along GBs as follows:

$$\frac{c_{\mathrm{gb}}}{t} = D_{\mathrm{gb}} \frac{}{y}\left(\frac{c_{\mathrm{gb}}}{y} - \frac{c_{\mathrm{gb}}\Omega}{kT}\frac{\sigma}{y}\right) + \frac{2D_{\mathrm{bulk}}}{\delta}\frac{c}{x} \tag{6.7}$$

where c_{gb} is the concentration of Zn at the GB, D_{gb} and D_{bulk} are the diffusion constants at the GB and bulk, Ω is the atomic volume, σ is the stress, and δ is the width of the GB. DiGiovanni et al. neglected the contribution of bulk diffusion based on Harrison’s classification of GB kinetics [32]. However, this reasoning is not entirely applicable to Fe-Zn LME because (a) Harrison’s classification is based on diffusion studies in alkali halides, which do not necessarily translate to metal embrittlement mechanisms, and (b) experimental results in the present study indicate that bulk

diffusion of Zn is not negligible. If the bulk diffusion term is retained in the formulation, the relationship between GB and bulk diffusion can be used to estimate GB diffusion when bulk diffusion is known. At steady state, $(\partial c_{gb})/\partial t = 0$, simplifying Equation 6.4.2 to:

$$D_{\text{gb}} \frac{^2 c_{\text{gb}}}{y^2} + \frac{2D_{\text{bulk}}}{\delta} \frac{c}{x} = 0 \tag{6.8}$$

The GB concentration gradient can be approximated to an exponential decay according to Fisher's model as $c_g b = e^{(-y/L_G B)}$ where L_{GB} is the diffusion length of Zn along the GB and can be approximated as $\partial^2 c_{gb}/\partial y^2 \approx c_{gb}/L_{gb}^2$ [18]. The GB diffusion length can thus be approximated as:

$$L_{\text{gb}} \approx \left(\frac{D_{\text{gb}}}{D_{\text{bulk}}} \right)^{1/2} L_{\text{bulk}} \tag{6.9}$$

where L_{bulk} is the measured diffusion length of Zn in the bulk. Dohie et al. experimentally measured the GB diffusion of Zn in α-Fe and developed an empirical relationship between D_{gb} and temperature as $D_{gb} = -0.0034exp(-162000/RT)$ [21]. Using this, (D_{gb}/D_{bulk}) is calculated to be roughly 140, based on the temperature and calculated D_{bulk} values from Section 6.2.3. However, this relationship does not account for the effect of stress on diffusion. DiGiovanni et al. developed an experimentally validated model on the effect of stress on GB diffusion, which demonstrated that under the stress gradient present in the RSW setup, the GB diffusion distance increases by a factor of 2.5 compared to the stress-free case [11]. Combining the results obtained by Dohie et al. and DiGiovanni et al. along with the calculated bulk diffusion constants, the ratio of diffusion lengths in the GB and bulk is:

$$\frac{L_{\text{gb}}}{L_{\text{bulk}}} \approx 29.58 \tag{6.10}$$

This relationship can thus be used to approximate GB diffusion distances at different RSW weld times from the measured EDS bulk diffusion distances - the GB diffusion distance is roughly 30 times the experimentally measured bulk diffusion distance. Thus, using bulk diffusion as an indirect measure of GB diffusion provides a reasonable approximation. A more accurate prediction can be made by integrating the effect of stress in the model predicting the GB diffusion constant of Zn in α-Fe. This approach allows for experimental validation of theoretical LME mechanisms despite the inherent limitations of direct GB diffusion measurements. High resolution STEM characterization by Kang et al. and Bertolo et al. provides experimental evidence demonstrating the presence of Zn in grain boundaries ahead of the crack tip [13, 33]. However the length of the Zn diffusion region ahead of the crack tip is not fully quantified. Using bulk diffusion data to estimate GB diffusion at different temperature and stress conditions could thus be a more effective way to quantify and understand the underlying mechanisms governing crack propagation during LME. It is important to note that although the overall diffusion profiles are comparable between EDS measurements and the numerical simulation, the

study has its limitations. The resolution of EDS measurements, simulation assumptions about Zn availability and intermetallic formation and the lack of a direct correlation between weld time and temperature can be potential sources of discrepancy.

6.5. Conclusions

This study analyses Zn diffusion during LME in TWIP steel by experimentally measuring Zn diffusion distances in various directions over a wide range of weld times. Unlike prior LME studies where the weld time is varied, this work directly characterizes Zn diffusion profiles ahead of the crack tip and relates them to welding parameters. This methodology facilitates the investigation of the relationship between welding parameters, diffusion behaviour, and the propagation of LME cracks. The key findings of this study are:

- Zn diffusion and weld time relationship: EDS measurements confirm that Zn diffusion distance increases with weld time in both RD and ND directions, with ND diffusion consistently greater than RD. This directional dependence highlights the influence of crack geometry and diffusion pathways in Zn transport ahead of the crack tip.
- Comparison between experimental and simulated diffusion: Simulated Zn diffusion distances follow the same trends as experimental data but predict higher absolute values, likely due to limitations in ThermoCalc diffusion data, intermetallic formation and other microstructural effects. However, the ratio of ND to RD diffusion distances in simulations closely matches experimental results, supporting the model's ability to capture directional diffusion trends.
- The GB diffusion distance of Zn is approximately 30 times the bulk diffusion distance based on model approximations: Since GB diffusion is the dominant LME mechanism but difficult to quantify directly, this study demonstrates that bulk diffusion measurements can be used to estimate GB diffusion behaviour under varying weld conditions, and the GB diffusion distance of Zn is roughly 30 times the bulk diffusion distance. This represents a novel approach for indirectly quantifying GB diffusion during RSW, where direct experimental measurement remains challenging.

The diffusion trends identified in the study provide a practical foundation for process design and simulation of RSW. The validated directional dependence (ND > RD) and the estimated ratio between GB and bulk diffusion can be implemented in predictive weld models to evaluate LME risk before production trials. In this way, the study supports the development of optimized welding schedules that balance weld performance and LME resistance in Zn-coated automotive steels. Future research should focus on directly quantifying Zn diffusion for different welding conditions along grain boundaries using high-resolution techniques such as TEM or atom probe tomography to better understand the dominant LME mechanisms. The influence of alloying elements on Zn diffusion in TWIP steel also requires further study, as existing thermodynamic databases may not fully capture non-equilibrium effects during welding. Additionally, integrating Zn

diffusion models with dynamic crack propagation simulations would provide a more comprehensive understanding of LME crack growth and bridge the gap between theoretical predictions and experimental observations.

References

[1] G. Mahadevan, V. Bertolo, S. Sabooni, V. Popovich, L. A. I. Kestens and M. Hermans. 'Characterizing zinc diffusion during liquid metal embrittlement of resistance spot welded TWIP steel'. In: *Welding in the World* (10th Feb. 2026). ISSN: 1878-6669. DOI: 10.1007/s40194-026-02384-4.

[2] C. Beal, X. Kleber, D. Fabregue and M. Bouzekri. 'Embrittlement of a zinc coated high manganese TWIP steel'. In: *Materials Science and Engineering: A* 543 (1st May 2012), pp. 76–83. ISSN: 0921-5093. DOI: 10.1016/j.msea.2012.02.049.

[3] L. Chen, Y. Zhao and X. Qin. 'Some aspects of high manganese twinning-induced plasticity (TWIP) steel, a review'. In: *Acta Metallurgica Sinica (English Letters)* 26.1 (1st Feb. 2013), pp. 1–15. ISSN: 2194-1289. DOI: 10.1007/s40195-012-0501-x.

[4] S.-H. Hong, J.-H. Kang, D. Kim and S.-J. Kim. 'Si effect on Zn-assisted liquid metal embrittlement in Zn-coated TWIP steels: Importance of Fe-Zn alloying reaction'. In: *Surface and Coatings Technology* 393 (15th July 2020), p. 125809. ISSN: 0257-8972. DOI: 10.1016/j.surfcoat.2020.125809.

[5] S. P. Murugan, V. Vijayan, C. Ji and Y. D. Park. 'Four types of LME cracks in RSW of Zn-coated AHSS'. In: *Weld J* 99.3 (2020), 75s–92s.

[6] P. Gordon and H. H. An. 'The mechanisms of crack initiation and crack propagation in metal-induced embrittlement of metals'. In: *Metallurgical Transactions A* 13.3 (1st Mar. 1982), pp. 457–472. ISSN: 1543-1940. DOI: 10.1007/BF02643354.

[7] E. E. Glickman. 'Dissolution Condensation Mechanism of Stress Corrosion Cracking in Liquid Metals: Driving Force and Crack Kinetics'. In: *Metallurgical and Materials Transactions A* 42.2 (1st Feb. 2011), pp. 250–266. ISSN: 1543-1940. DOI: 10.1007/s11661-010-0429-6.

[8] Z. Ling, T. Chen, L. Kong, M. Wang, H. Pan and M. Lei. 'Liquid Metal Embrittlement Cracking During Resistance Spot Welding of Galvanized Q&P980 Steel'. In: *Metallurgical and Materials Transactions A* 50.11 (1st Nov. 2019), pp. 5128–5142. ISSN: 1543-1940. DOI: 10.1007/s11661-019-05388-6.

[9] J. Barthelmie, A. Schram and V. Wesling. 'Liquid Metal Embrittlement in Resistance Spot Welding and Hot Tensile Tests of Surface-refined TWIP Steels'. In: *IOP Conference Series: Materials Science and Engineering* 118 (Mar. 2016), p. 012002. ISSN: 1757-899X. DOI: 10.1088/1757-899X/118/1/012002.

[10] Z. Ling, M. Wang, L. Kong and K. Chen. 'Towards an explanation of liquid metal embrittlement cracking in resistance spot welding of dissimilar steels'. In: *Materials & Design* 195 (1st Oct. 2020), p. 109055. ISSN: 0264-1275. DOI: 10.1016/j.matdes.2020.109055.

[11] C. DiGiovanni, A. Ghatei Kalashami, E. Biro and N. Y. Zhou. 'Liquid metal embrittlement transport mechanism in the Fe/Zn system: Stress-assisted diffusion'. In: *Materialia* 18 (1st Aug. 2021), p. 101153. ISSN: 2589-1529. DOI: 10.1016/j.mtla.2021.101153.

[12] Y. G. Kim, I. J. Kim, J. S. Kim, Y. I. Chung and D. Y. Choi. 'Evaluation of Surface Crack in Resistance Spot Welds of Zn-Coated Steel'. In: *MATERIALS TRANSACTIONS* 55.1 (2014), pp. 171–175. DOI: 10.2320/matertrans.M2013244.

[13] H. Kang, L. Cho, C. Lee and B. C. De Cooman. 'Zn Penetration in Liquid Metal Embrittled TWIP Steel'. In: *Metallurgical and Materials Transactions A* 47.6 (1st June 2016), pp. 2885–2905. ISSN: 1543-1940. DOI: 10.1007/s11661-016-3475-x.

[14] G. Jung, I. S. Woo, D. W. Suh and S.-J. Kim. 'Liquid Zn assisted embrittlement of advanced high strength steels with different microstructures'. In: *Metals and Materials International* 22.2 (1st Mar. 2016), pp. 187–195. ISSN: 2005-4149. DOI: 10.1007/s12540-016-5579-7.

[15] D.-Y. Choi, A. Sharma, S.-H. Uhm and J. P. Jung. 'Liquid Metal Embrittlement of Resistance Spot Welded 1180 TRIP Steel: Effect of Electrode Force on Cracking Behavior'. In: *Metals and Materials International* 25.1 (1st Jan. 2019), pp. 219–228. ISSN: 2005-4149. DOI: 10.1007/s12540-018-0180-x.

[16] L. Klinger and E. Rabkin. 'The effect of stress on grain boundary interdiffusion in a semi-infinite bicrystal'. In: *Acta Materialia* 55.14 (1st Aug. 2007), pp. 4689–4698. ISSN: 1359-6454. DOI: 10.1016/j.actamat.2007.04.039.

[17] J. S. Dohie, J. Cahoon and W. Caley. 'The Grain-Boundary Diffusion of Zn in α-Fe'. In: *Journal of Phase Equilibria and Diffusion* 28.4 (1st Aug. 2007), pp. 322–327. ISSN: 1863-7345. DOI: 10.1007/s11669-007-9093-y.

[18] J. C. Fisher. 'Calculation of Diffusion Penetration Curves for Surface and Grain Boundary Diffusion'. In: *Journal of Applied Physics* 22.1 (1st Jan. 1951), pp. 74–77. ISSN: 0021-8979. DOI: 10.1063/1.1699825.

[19] K. Prabitz, M. Asadzadeh, M. Pichler, T. Antretter, C. Beal, H. Schubert, B. Hilpert, M. Gruber, R. Sierlinger and W. Ecker. 'Liquid metal embrittlement of advanced high strength steel: Experiments and damage modeling'. In: *Materials* 14.18 (2021). ISSN: 1996-1944. DOI: 10.3390/ma14185451.

[20] M. Tumuluru. 'Effect of silicon and retained austenite on the liquid metal embrittlement cracking behavior of GEN3 and high-strength automotive steels'. In: *Weld J* 98 (2019), 351S–364S.

[21] Y. Ikeda. 'Early stages of liquid-metal embrittlement in a 3rd generation advanced high strength steel'. In: (2024).

[22] 'Solutions of the Diffusion Equation'. In: *Diffusion in Solids: Fundamentals, Methods, Materials, Diffusion-Controlled Processes*. Ed. by H. Mehrer. Berlin, Heidelberg: Springer, 2007, pp. 37–53. ISBN: 978-3-540-71488-0. DOI: 10.1007/978-3-540-71488-0_3.

[23] P. Shewmon. *Diffusion in solids*. Springer, 2016.

[24] C. Di Giovanni. 'Liquid Metal Embrittlement in Resistance Spot Welding: The Thermomechanical Origin and Embrittler Transport Mechanism'. Accepted: 2021-08-05T18:13:07Z. PhD thesis. University of Waterloo, 5th Aug. 2021.

[25] K. M. Prabitz, T. Antretter, M. Rethmeier, B. El-Sari, H. Schubert, B. Hilpert, M. Gruber, R. Sierlinger and W. Ecker. 'Numerical and experimental assessment of liquid metal embrittlement in externally loaded spot welds'. In: *Welding in the World* 68.10 (1st Oct. 2024), pp. 2713–2722. ISSN: 1878-6669. DOI: 10.1007/s40194-024-01696-7.

[26] X. Wang, Y. Xie, Z. Liu, Q. Sun, X. Shen, Q. Zhang, Z. Hu and R. Misra. 'Zn-induced liquid metal embrittlement and mechanical properties of advanced high-strength steel with resistance spot weld'. In: *Materials Science and Engineering A* 843 (2022). ISSN: 0921-5093. DOI: 10.1016/j.msea.2022.143088.

[27] C. Herzig and Y. Mishin. 'Grain Boundary Diffusion in Metals'. In: *Diffusion in Condensed Matter: Methods, Materials, Models*. Ed. by P. Heitjans and J. Kärger. Berlin, Heidelberg: Springer, 2005, pp. 337–366. ISBN: 978-3-540-30970-3. DOI: 10.1007/3-540-30970-5_8.

[28] Y. Ikeda, R. Yuan, A. Chakraborty, H. Ghassemi-Armaki, J. M. Zuo and R. Maaß. 'Early stages of liquid-metal embrittlement in an advanced high-strength steel'. In: *Materials Today Advances* 13 (1st Mar. 2022), p. 100196. ISSN: 2590-0498. DOI: 10.1016/j.mtadv.2021.100196.

[29] H. Lee, M. C. Jo, S. S. Sohn, S.-H. Kim, T. Song, S.-K. Kim, H. S. Kim, N. J. Kim and S. Lee. 'Microstructural evolution of liquid metal embrittlement in resistance-spot-welded galvanized TWinning-Induced Plasticity (TWIP) steel sheets'. In: *Materials Characterization* 147 (1st Jan. 2019), pp. 233–241. ISSN: 1044-5803. DOI: 10.1016/j.matchar.2018.11.008.

[30] D. Shindo and T. Oikawa. 'Energy Dispersive X-ray Spectroscopy'. In: *Analytical Electron Microscopy for Materials Science*. Ed. by D. Shindo and T. Oikawa. Tokyo: Springer Japan, 2002, pp. 81–102. ISBN: 978-4-431-66988-3. DOI: 10.1007/978-4-431-66988-3_4.

[31] P. Lejček. 'Grain Boundaries: Description, Structure and Thermodynamics'. In: *Grain Boundary Segregation in Metals*. Ed. by P. Lejcek. Berlin, Heidelberg: Springer, 2010, pp. 5–24. ISBN: 978-3-642-12505-8. DOI: 10.1007/978-3-642-12505-8_2.

[32] L. G. Harrison. 'Influence of dislocations on diffusion kinetics in solids with particular reference to the alkali halides'. In: *Transactions of the Faraday Society* 57.0 (1st Jan. 1961), pp. 1191–1199. ISSN: 0014-7672. DOI: 10.1039/TF9615701191.

[33] V. Bertolo, G. Mahadevan, R. de Kloe, R. H. Petrov and V. Popovich. 'Decoupling early-stage cracking and propagation mechanisms in liquid metal embrittlement of Zn-galvanised TWIP steel'. In: *Journal of Materials Research and Technology* 38 (1st Sept. 2025), pp. 1617–1632. ISSN: 2238-7854. DOI: 10.1016/j.jmrt.2025.08.055.

7

Effect of RSW hold time on LME

While welding parameters such as current, force, and weld time have been studied in relation to Liquid Metal Embrittlement (LME), the effect of hold time on LME is a gap in literature. This chapter investigates the influence of RSW hold time on LME crack formation in an electrogalvanized TWIP steel, with the hold time varied from 5 ms to 355 ms in increments of 50 ms while all other welding parameters are constant. Optical microscopy was performed on RSW cross-sections to quantify the number and depth of LME cracks across three distinct regions of the weld: the electrode region, the weld shoulder region, and the weld periphery region. FEA simulations were carried out to characterize temperature evolution at each of these locations. Results show that increasing hold time reduces LME crack density in the electrode region, with no cracks observed at hold times of 205 ms and above, due to heat extraction and Zn solidification by the water-cooled electrodes. In the weld shoulder region, crack initiation conditions were found to be independent of hold time, while crack propagation was influenced by the temperature reached after electrode lift-off. The weld periphery region showed no clear dependence on hold time, consistent with its limited contact with RSW electrodes. FEA simulations demonstrate that all temperature profiles are identical up to the onset of hold time, and diverge only after electrode lift-off, with shorter hold times producing higher temperatures across all regions. These findings demonstrate that hold time is an effective parameter for controlling LME severity and location in TWIP steel spot welds, with practical implications for RSW parameter optimization in automotive manufacturing.

7.1. Introduction

The scientific context for this study, including the properties of TWIP steel, the role of zinc coatings, and the RSW process, is described in Chapter 2. Among the RSW process parameters discussed there, hold time remains comparatively less researched in relation to LME; this chapter investigates its influence across the three distinct regions of the weld cross-section.

Welding parameters in RSW have a direct effect on liquid metal embrittlement crack formation, location, and size. LME severity is observed to increase with increasing weld current and weld time due to the higher heat input which promotes Zn penetration

along austenitic grain boundaries [1]. The larger electrode indentation also increases thermo-mechanical stresses during cooling [2]. Bhattacharya et al. reported that LME crack density and depth increased at higher weld currents and prolonged weld cycles, especially near the weld shoulder, where large thermal gradients develop [3]. FEA analyses and experimental studies showed that critical stresses for LME arise mainly during the cooling stage, and that reducing weld current and weld time lowers these stresses and thus suppresses crack formation [4]. For a given current, longer weld times have been observed to increase the number and depth of surface LME cracks, as more heat input increases the nugget size and stress concentration during cooling [5]. DiGiovanni et al. showed that a ramp down strategy for welding current reduced the severity of LME cracks by 60% [6]. While numerous studies have investigated the effects of RSW parameters like current, force, electrode geometry and weld time, there are comparatively fewer studies on the effect of RSW hold time on LME. Kim et al. studied the effect of various welding parameters on LME and found that increase in hold time reduced surface cracking. However, the study also concluded that further investigation was required to correlate LME crack depth and weld heat input [5]. Choi et al. performed RSW tests on TRIP steel, where hold times of 20 ms, 300 ms and 1000 ms were applied for different weld times (200 ms, 400 ms and 800 ms) and weld currents (6.5 kA and 8 kA). The study concluded that for a given weld time setting, an increase in the hold time reduced the number of LME cracks at the sheet-electrode interface. The study did not observe a correlation between increasing hold time and cracks at the weld shoulder region [7]. Bohne et al. performed RSW studies on a dissimilar stack of DP1200 steel and mild steel at hold times of 10 ms, 200 ms and 800 ms at a current of 9.3 kA, force of 4.5 kN and weld time of 1520 ms. The study found that LME crack formation could be controlled by the selection of specific hold times. LME was observed at a lower hold time of 10 ms but not at 200 ms or 800 ms for a double stack weld. The study also performed FEA simulations where the temperature and stress were calculated at locations corresponding to LME cracks from RSW [8]. While this study shows a clear comparison between experimental RSW results and finite element simulations, the range of hold times investigated is limited. Only three hold times were examined, with large intervals between them, which limits understanding of how gradual changes in hold time influence LME behaviour. In addition, FEA focuses on temperature and stress evolution only at locations where cracks were experimentally observed. Extending the analysis to include all regions of the weld would provide a more complete picture of temperature distribution that directly affects the availability of liquid Zn to penetrate the steel. Although the effect of hold time on LME during RSW has been previously studied, the number of such studies remains limited. In addition, these studies only look at a small number (3 or fewer) of different hold time values. The hold times also differ by hundreds of milliseconds, which makes it difficult to clearly observe the evolution of LME behaviour with changing hold time. In this study, hold time is varied from 5 ms to 355 ms in steps of 50 ms while all other welding parameters are kept constant. The resulting welds are evaluated to characterize the number, location, and size of LME cracks across the weld cross section. FEA simulations are also performed to characterize temperature evolution at multiple locations within the weld region.

7.2. Materials and Methods

The materials and methods for the RSW process, characterization and FEA setup is elaborated in Chapter 3.

7.3. Results

7.3.1. Optical microscopy of RSW cross-sections

This section presents the experimental results obtained from RSW of TWIP steel at different hold times, and these are described individually for each hold time. A comparative overview of the crack location and crack depth data is consolidated in Section 7.3.2. To support the discussion of crack location, the weld cross section is divided into three regions, as shown in Figure 7.1. Region 1 extends from the weld centre to 1.5 mm from the centre line and corresponds to the area directly beneath the RSW electrode, henceforth referred to as the “electrode region”. This region is shown in blue. Region 2, henceforth referred to as the ”weld shoulder region” is in contact with the curved portion of the electrode, and is shown in orange. Region 3, henceforth referred to as the “weld periphery region” is more than 3 mm from the weld centre. This region is not in direct contact with the electrode, and is shown in green. These regions were chosen because the temperature evolution profiles (discussed later in the section) are distinct, which result in different LME crack morphologies.

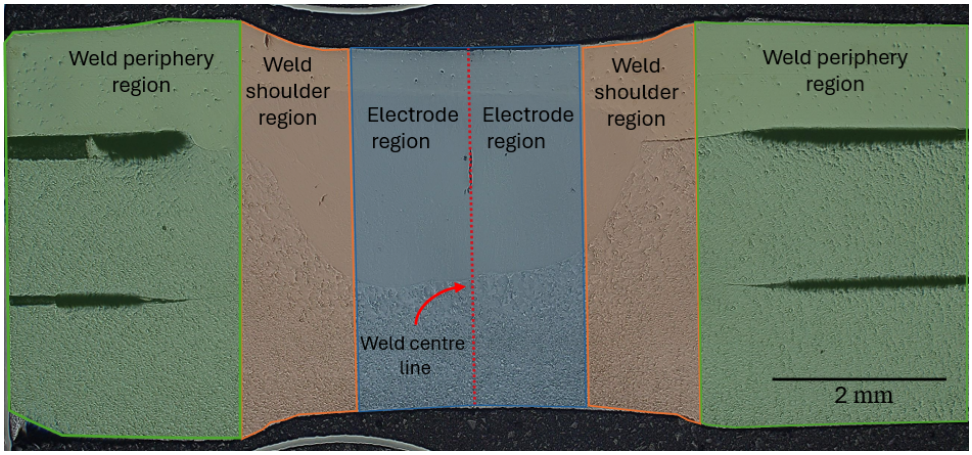


Figure 7.1: Schematic RSW cross-section showing the different regions of the weld - the electrode-pressed region (blue), the weld shoulder region (orange), and the weld periphery region (green)

Hold time = 5 ms

Figure 7.2 shows one of the RSW cross-sections for hold time = 5 ms. LME cracks were observed across all regions of the weld. The highest number of cracks was found in the electrode region, with an average of 13.5 ± 4 cracks. LME cracks in this region had an

average depth of 64.3 ± 36.7 µm. In the weld shoulder region, the average number of cracks was 7.5 ± 1.44, with an average crack depth of 80 ± 57.1 µm. Fewer cracks were observed in the weld periphery region, with an average of 0.75 cracks. Of the four samples studied, three contained a single crack in this region. The average crack depth in the weld periphery region was 175 ± 7.3 µm.

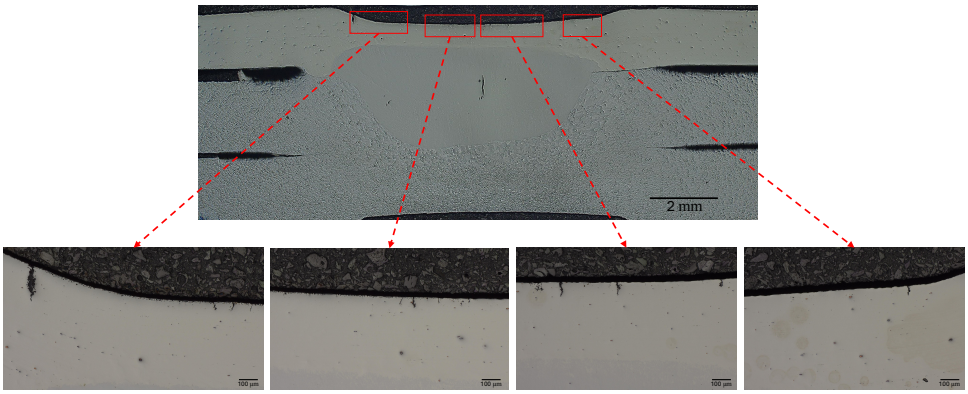


Figure 7.2: RSW cross-section at hold time = 5 ms, showing LME cracks at different locations of the weld

Hold time = 55 ms

Figure 7.3 shows one of the RSW cross-sections for a hold time of 55 ms. The spatial distribution of LME cracks was similar to that observed at 5 ms, with cracks present in the electrode region, weld shoulder region, and weld periphery region. However, the number of cracks at 55 ms was lower than at 5 ms, but the cracks were deeper on average. In the electrode region, the average number of cracks was 8.5 ± 2.5, with an average crack depth of 160.2 ± 47.6 µm. In the weld shoulder region, the average number of cracks was 5.5 ± 1.19, with an average depth of 142.6 ± 54.7 µm. Fewer cracks were observed in the weld periphery region, with an average of 0.5 ± 0.5 cracks. Of the four samples examined, two contained a single crack in this region, while no cracks were observed in the remaining two samples. The average crack depth in the weld periphery region was 89.6 µm.

Hold time = 105 ms

Figure 7.4 shows one of the RSW cross-sections for hold time = 105 ms. LME cracks were observed in all regions of the weld, although the overall number of cracks was lower compared to shorter hold times. In the electrode region, an average of 3 ± 2 cracks was observed, with an average crack depth of 104.6 ± 23.8 µm. The weld shoulder region showed an average of 3.25 ± 1.4 cracks, with an average depth of 153.6 ± 31 µm. In the weld periphery region, two of the four samples contained a single crack, while no cracks were observed in the remaining samples. The average crack depth in this region was 105.1 ± 12.6 µm.

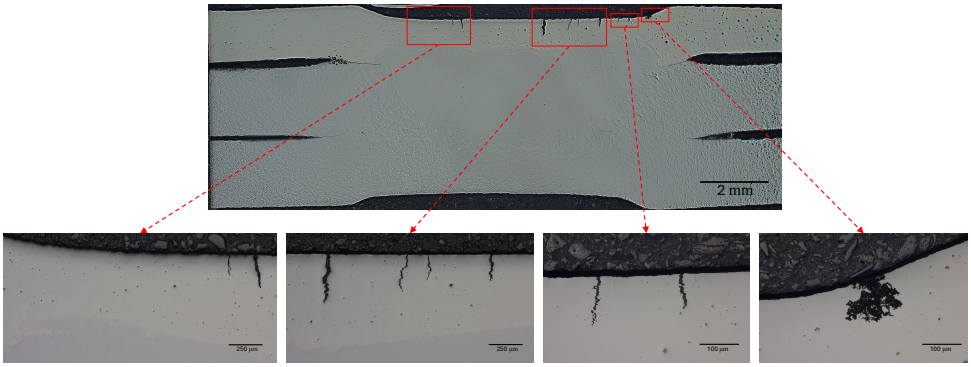


Figure 7.3: RSW cross-section at hold time = 55 ms, showing LME cracks at different locations of the weld

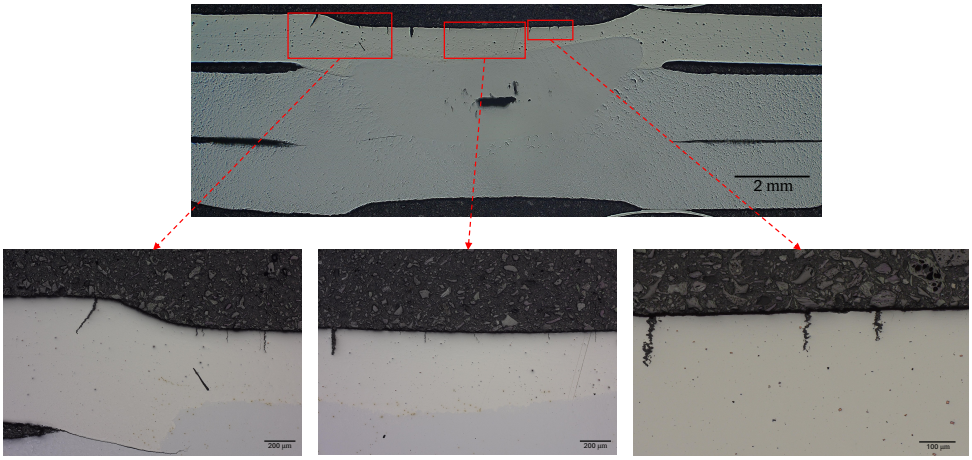


Figure 7.4: RSW cross-section at hold time = 105 ms, showing LME cracks at different locations of the weld

Hold time = 155 ms

Figure 7.5 shows one of the RSW cross-sections at hold time = 155 ms. Among the four analysed samples, only one sample exhibited LME cracks in the electrode-pressed region, with four cracks observed and an average depth of 76.1 ± 9.9 µm. The remaining three samples did not show any LME cracks in this region.

In the weld shoulder region, three out of the four samples contained one LME crack each, with an average crack depth of 334.6 ± 52.8 µm. As shown in Figure 7.6 (a different RSW cross-section compared to Figure 7.5), crack growth in this region was limited by the formation of the weld fusion zone, with cracks terminating at the interface between the austenitic TWIP matrix and the fusion zone. The crack tip appears to be blunt at the interface between the weld fusion zone and the TWIP layer. This suggests

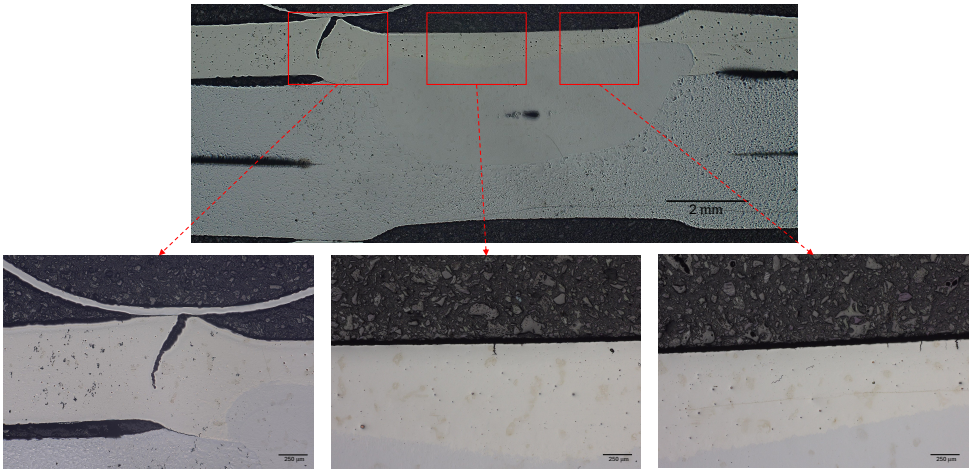


Figure 7.5: RSW cross-section at hold time = 155 ms, showing LME cracks at different locations of the weld

that differences in phase constitution may influence crack growth in this region. Only one of the four samples (Figure 7.5) showed an LME crack in the weld periphery region, with a depth of 820 µm.



Figure 7.6: LME crack in the weld shoulder region at hold time = 155 ms

Hold time = 205 ms

Figure 7.7 shows one of the RSW cross-sections at a hold time of 205 ms. At this hold time, none of the samples exhibited LME cracks in the electrode region. In the weld shoulder region, three out of the four samples showed one LME crack each, with an average crack depth of 305 µm. Similar to the behaviour observed at a hold time of 155 ms, crack growth in this region was influenced by the formation of the weld fusion zone. As shown in Figure 7.7, a change in crack morphology is observed at the fusion zone interface, where the crack thickness decreases. In the weld periphery region, two of the four samples contained one LME crack each, with an average crack depth of 219 µm.

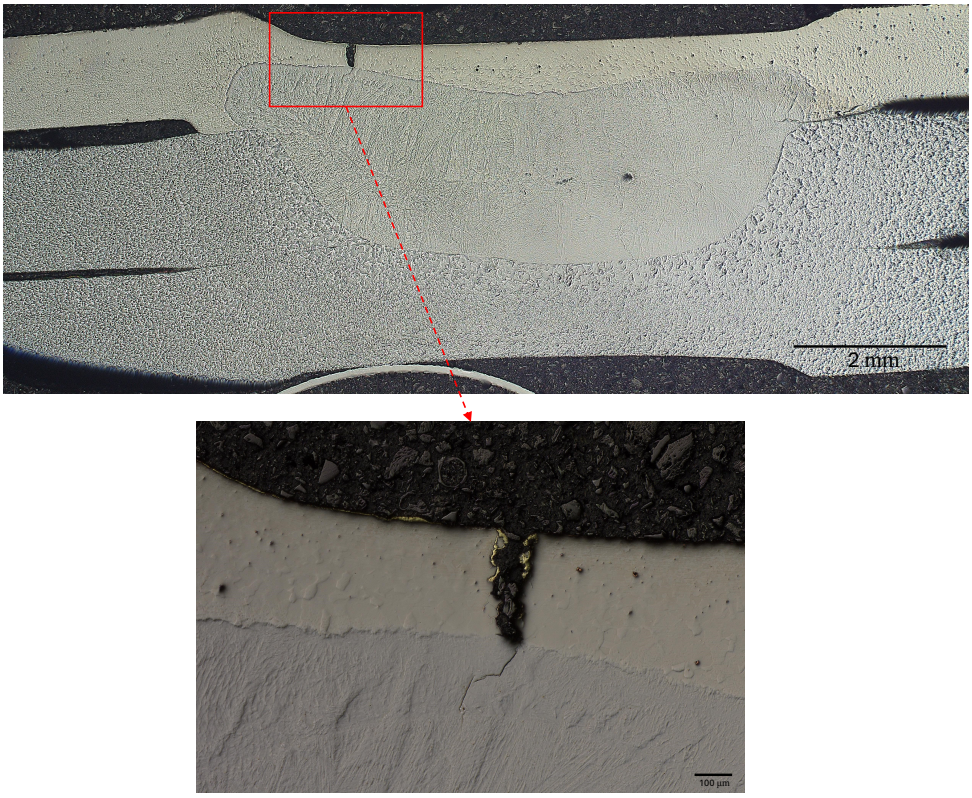


Figure 7.7: RSW cross-section at hold time = 205 ms, showing LME cracks at different locations of the weld

Hold time = 255 ms

Figure 7.8 shows an RSW cross-section at a hold time of 255 ms. At this hold time, no LME cracks were observed in either the electrode region or the weld periphery region across all samples. All samples showed one LME crack each in the weld shoulder region, with an average crack depth of 200 ± 74.5 µm. Similar to the behaviour observed

at hold times of 155 ms and 205 ms, crack propagation in this region was influenced by the formation of the weld fusion zone. The crack tips terminate at the interface between the TWIP base material and the weld fusion zone, as shown in Figure .7.8

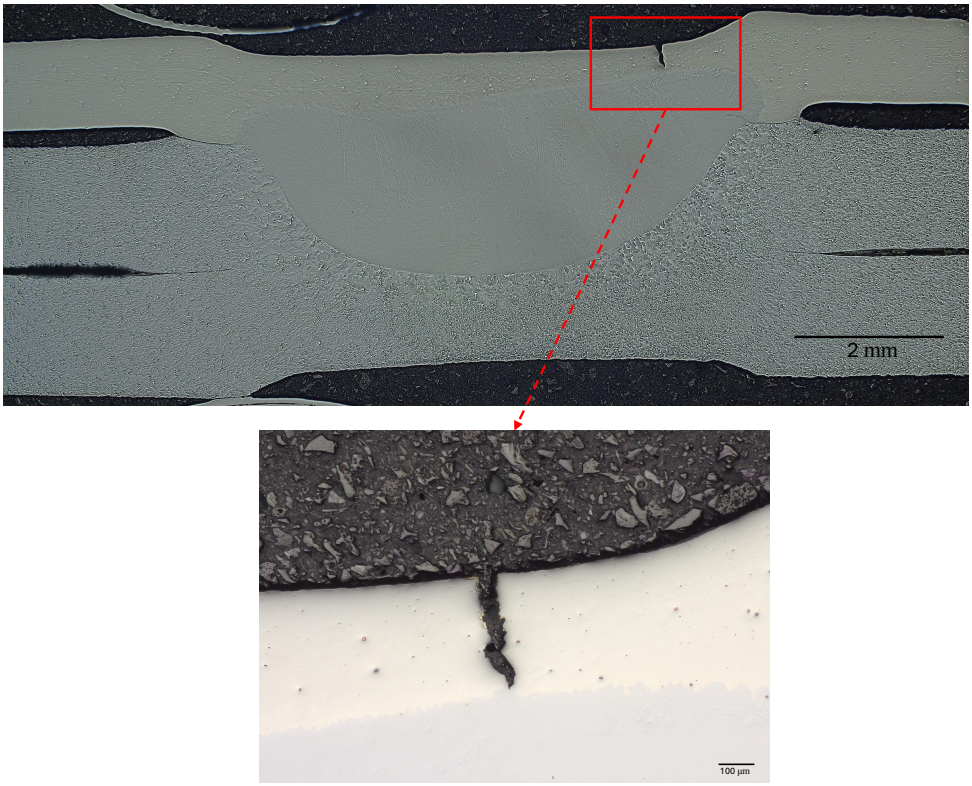


Figure 7.8: RSW cross-section at hold time = 255 ms, showing LME cracks at different locations of the weld

Hold time = 305 ms

Figure 7.9 shows an RSW cross-section at a hold time of 305 ms. At this hold time, no LME cracks were observed in the electrode region. In the weld shoulder region, three out of the four samples showed one LME crack each, with an average crack depth of 111 ± 15 µm. LME cracks were also observed in the weld periphery region. Two of the four samples contained cracks in this region, with one sample showing two cracks and the other showing a single crack. The average crack depth in the weld periphery region was 128 ± 21 µm.

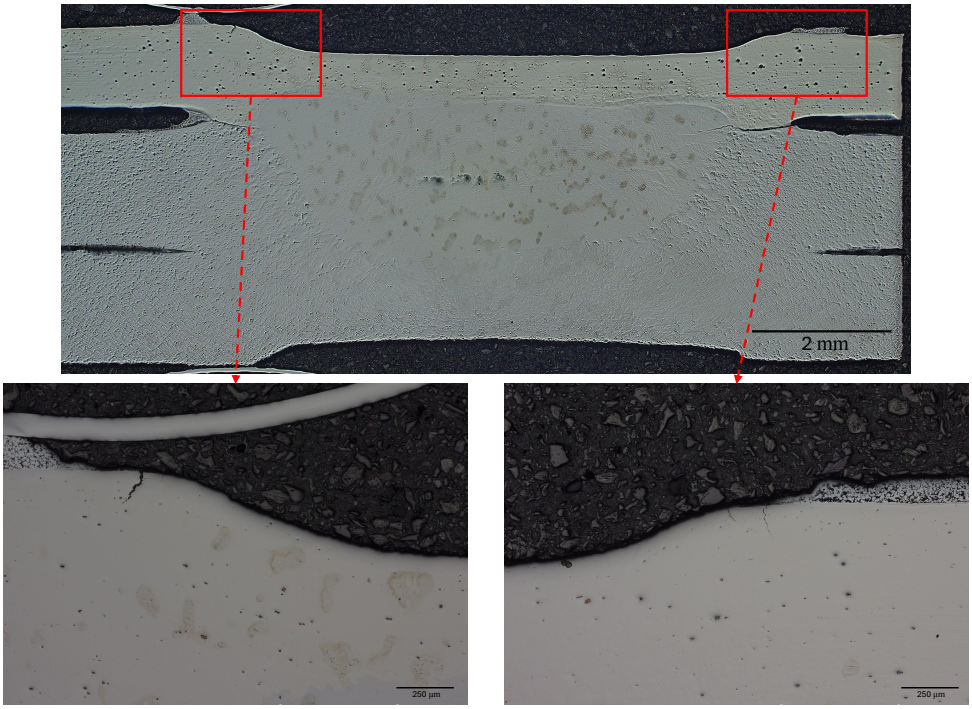


Figure 7.9: RSW cross-section at hold time = 305 ms, showing LME cracks at different locations of the weld

Hold time = 355 ms

Figure 7.10 shows an RSW cross-section at a hold time of 355 ms. At this hold time, none of the analysed samples showed any LME cracks in the electrode region, weld shoulder region, or weld periphery region.

7.3.2. Comparing hold times

Figure 7.11 shows consolidated crack location and geometry data for all hold times. In the electrode region, the number of LME cracks decreases with increasing hold time. The lowest hold time of 5 ms shows the highest number of cracks, with an average of 13.5 cracks per cross-section. This number decreases progressively with increasing hold time up to 155 ms. At hold times of 205 ms and above, no LME cracks are observed in this region. The average crack depth in this region increases from 5 ms (64 µm) to 55 ms (160 µm). Beyond 55 ms, no clear trend in crack depth is observed up to 155 ms. At higher hold times, no LME cracks are observed in this region. In the weld shoulder region, the average number of LME cracks decreases from approximately 7 cracks at a hold time of 5 ms and continues to reduce with increasing hold time, reaching an average of 0.75 cracks per cross-section at 155 ms. At higher hold times, no clear trend in crack number is observed. Most hold times between 155 ms and 305



Figure 7.10: RSW cross-section at hold time = 355 ms, showing No LME cracks

ms show approximately one LME crack per cross-section, while no LME cracks are observed at 355 ms. The average crack depth in this region increases with increasing hold time from approximately 80 µm at 5 ms to a maximum average depth of 334 µm at 155 ms. Above 155 ms, the average crack depth shows a decreasing trend up to a hold time of 305 ms. However, at higher hold times, the number of cracks is low, and the measured crack depths show a large spread. As a result, any apparent trend in crack depth is less statistically significant and should be interpreted with caution. In the weld periphery region, no clear relationship between hold time and either the number of cracks or crack depth is observed. The average crack depths measured at hold times of 155 ms (820 µm) and 205 ms (219 µm) are higher than those measured at lower hold times. However, the number of cracks at these hold times is low. Only one out of four samples at 155 ms and two out of four samples at 205 ms showed LME cracks in this region. Given the limited number of cracks observed, any trend between hold time and crack behaviour in the weld periphery region remains inconclusive.

7.3.3. FEA of RSW

Finite element simulations were used to calculate the temperature evolution at three locations in the weld cross-section, corresponding to the electrode region, weld shoulder region, and weld periphery region. All points were selected within the top TWIP sheet, just below the Zn coating. Temperature-time profiles were plotted for each region at all investigated hold times. For clarity, the temperature histories for different hold times are overlaid for each region, and the results are discussed separately in the following subsections.

Data validation and model reliability

Before discussing the temperature evolution profiles, it is necessary to address the validity of the FEA results for the investigated hold times. At hold times of 5 ms, 55 ms, and 105 ms, the SORPAS FEA model predicts full melting of the top TWIP sheet, with

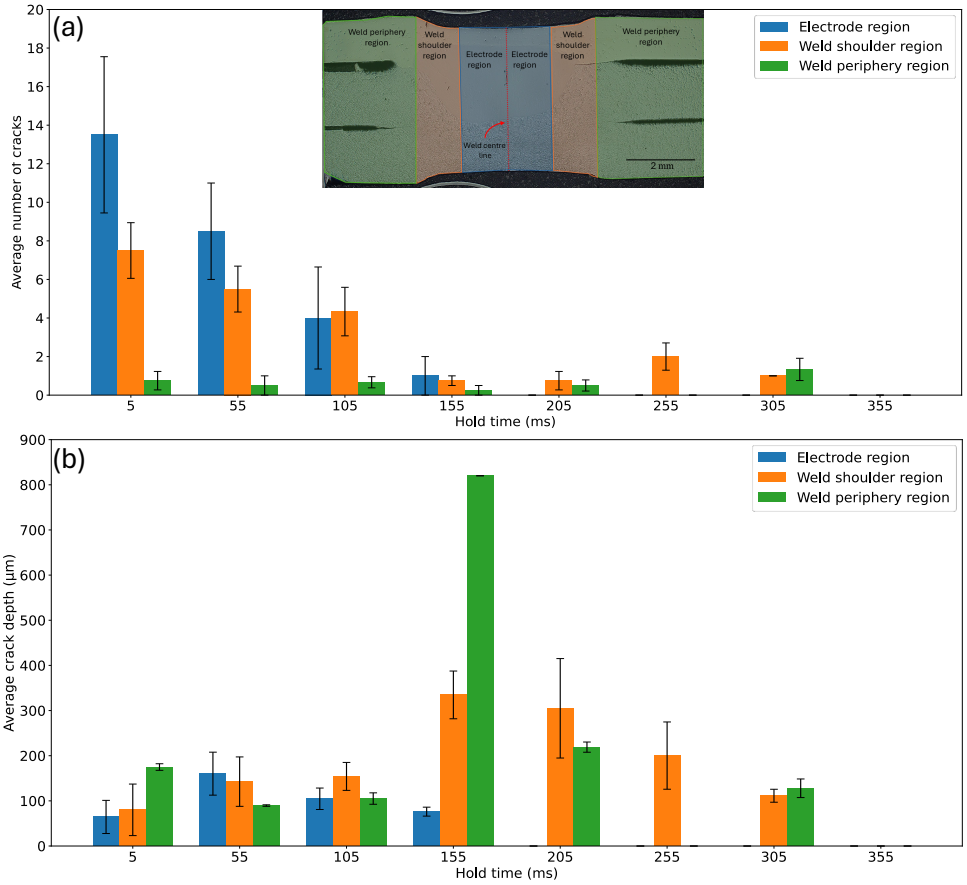


Figure 7.11: Consolidated data of (a) average number of LME cracks versus hold time, and (b) average LME crack depth versus hold time

the weld fusion zone extending through its entire thickness. This is inconsistent with experimental observations: RSW cross-sections at these welding conditions (Figure 7.2, Figure 7.3 and Figure 7.5) clearly show that the weld fusion zone does not penetrate the full thickness of the top TWIP sheet. Accurate modelling of the RSW process at these hold times is complicated by several factors: (a) the model becomes sensitive to uncertainties in temperature dependent material properties like thermal conductivity, electrical resistivity, and yield strength; (b) the behaviour of the Zn coating (melting, displacement, and vaporisation) is not fully captured by the model, leading to inaccuracies in the electrical contact resistance at the sheet interface; and (c) mesh size limitations in SORPAS constrain the spatial resolution of the temperature gradient at the coating-substrate interface. To address these inaccuracies, different modelling strategies were used, like reducing mesh size, adjusting sheet thickness, modifying Zn

coating properties, and reducing weld heat input. However, these strategies did not yield a solution that accurately reproduced the experimentally observed fusion zone geometry at hold times of 5 ms to 105 ms. For hold times of 155 ms and above, the FEA model shows good agreement with experimental observations. At these hold times, the temperature evolution in the top TWIP sheet occurs at lower peak temperatures. As a result, the simulation becomes less sensitive to uncertainties in electrical contact resistance, temperature dependent material properties, and phase transformation behaviour. In addition, by this stage of the welding cycle, the weld fusion zone geometry is already established and remains stable during subsequent cooling. These factors contribute to improved agreement between the simulated and experimentally measured weld nugget dimensions. Figure 7.12 shows the weld cross-sections at different hold times and Table 7.1 shows the comparison between the experimentally measured weld nugget area and the FEA simulations. The FEA results show a slight increase in weld nugget area with increasing hold time; however, the magnitude of this change is small, with a difference of approximately 0.6 mm² between hold times of 5 ms and 355 ms. This can be attributed to the water-cooled electrodes that vary the amount of heat extraction from the weld that causes variable weld nugget geometry. This trend is not observed in the RSW cross-section weld nugget area measurements. This discrepancy may be due to uncertainties in sample preparation and sectioning. In particular, the cross-sections may not have been taken exactly through the weld centerline, and minor material loss during polishing could affect the measured nugget area.

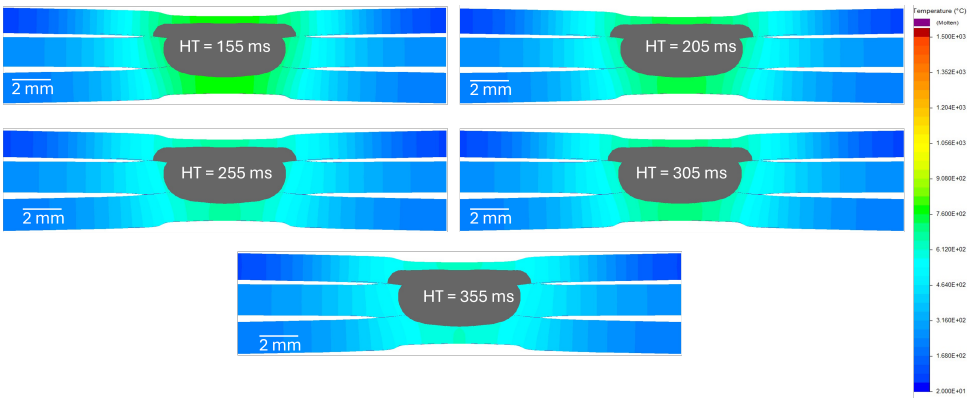


Figure 7.12: : RSW cross-sections at different hold times from FEA simulations using SORPAS

The temperature-time profiles presented in Figure 7.13 (electrode region), Figure 7.14 (weld shoulder region), and Figure 7.15 (weld periphery region) show that the temperature evolution in all three regions of the weld is identical from the start of the welding cycle up to the onset of the hold time, regardless of the hold time. The profiles diverge after the electrode is lifted, and in all cases follows the same shape: a temperature rise after removal of the electrodes, a peak, and a subsequent decrease due to air cooling. This behaviour across all hold times provides a basis for extending

Table 7.1: Comparison of weld nugget geometry between experimental measurement and FEA simulations

Hold time (ms)	Weld nugget area from optical microscopy (mm^2)	Weld nugget area from FEA simulation (mm^2)
155	13.55 ± 0.33	13.53
205	12.83 ± 0.36	13.74
255	13.23 ± 0.48	13.98
305	13.14 ± 0.31	14.06
355	13.17 ± 0.56	14.13

the temperature profiles to shorter hold times by extrapolation. Since the temperature of the weld at the end of the weld time is independent of hold time, the temperature profiles at 5 ms, 55 ms, and 105 ms are expected to follow the same trajectory up to the start of the hold period. At the end of the weld time, the same temperature rise is expected, but offset to a higher magnitude. Longer hold times allow more heat to be extracted by the water-cooled electrodes before lift-off, resulting in a lower peak temperature after the end of the hold time. This effect scales with the hold time across all conditions, and can thus be extrapolated for hold times between 5 ms and 105 ms. The extrapolated temperature profiles for these hold times are shown as dashed curves in Figure 7.13, Figure 7.14 and Figure 7.14 by projecting the temperature-time profile trend to shorter hold times. Although these extrapolated profiles carry greater uncertainty than the directly simulated results, they are used in the discussion as a qualitative guide to interpreting LME behaviour at short hold times.

7.3.4. Temperature evolution in electrode region

Figure 7.13 shows the temperature versus time plots at the electrode region for hold times ranging from 155 ms to 355 ms, plotted together for comparison. The red 'X' indicates the point in the region where the temperature plot is calculated. The red dashed region represents the extrapolated temperature profiles for hold times of 5 ms, 55 ms and 105 ms that were not calculated by SORPAS due to modelling limitations. The justification for this extrapolation is presented in Section 7.3.3. From the start of the welding cycle up to start of the hold time, the temperature profiles for all hold times overlap completely, indicating that the temperature evolution in this region is identical during the squeeze and weld stages. The peak temperature reached before the start of the hold time is approximately 750 °C for all cases. After the end of the hold time, corresponding to electrode lift-off, the temperature profiles begin to diverge. For all investigated hold times, the temperature increases after electrode lift-off, reaches a maximum value, and then decreases with time. The peak temperature reached after the hold time is higher for shorter hold times and decreases progressively as the hold time is increased. The peak temperature reaches 1150 °C for a hold time of 155 ms and reduces to 780 °C for a hold time of 355 ms. Despite this difference in peak temperature, the overall shape and trend of the temperature versus time profiles remain

the same for all hold times.

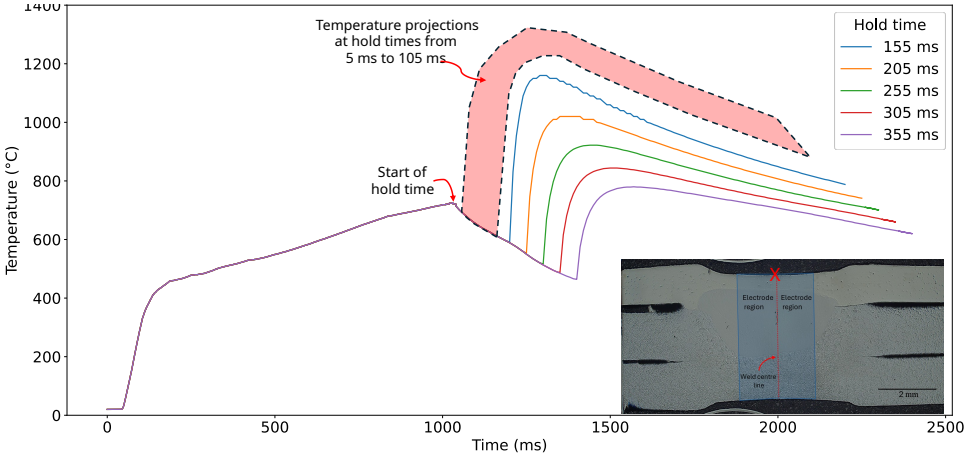


Figure 7.13: Temperature versus time plot in the electrode region for different hold times, where the red 'X' marks the location of the plot

7.3.5. Temperature evolution in weld shoulder region

Figure 7.14 shows the temperature versus time plot at the weld shoulder region. The red "X" in the figure marks the location within the weld shoulder region at which the temperature history was calculated. The red dashed region represents the extrapolated temperature profiles for hold times of 5 ms, 55 ms and 105 ms that were not calculated by SORPAS due to modelling limitations. The justification for this extrapolation is presented in Section 7.3.3. Similar to the electrode region, the temperature profiles for all hold times overlap perfectly from the start of the welding cycle up to the beginning of the hold time, indicating identical thermal histories during the squeeze and weld stages. During the weld time stage of the RSW process, the temperature in this region rises rapidly and reaches a peak of approximately 1000 °C within the first 250 ms. This is followed by a decrease to 430 °C at 400 ms, after which the temperature increases again and reaches approximately 650 °C at the start of the hold time period. After the onset of the hold time, the temperature profiles corresponding to different hold times begin to diverge. For each hold time, removal of the water-cooled electrodes at the end of the hold period leads to a further increase in temperature, followed by a gradual decrease due to air cooling. As observed in the electrode region, the peak temperature reached after electrode lift-off is highest for shorter hold times and decreases as the hold time is increased.

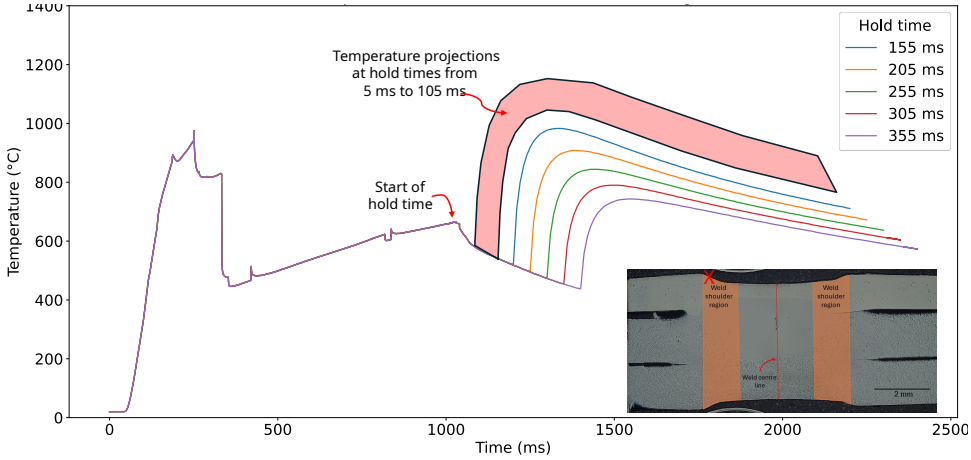


Figure 7.14: Temperature versus time plot in the weld shoulder region for different hold times, where the red 'X' marks the location of the plot

7.3.6. Temperature evolution in weld periphery region

Figure 7.15 shows the temperature versus time plot at the weld periphery region for all simulated hold times. The red "X" in the figure indicates the location within the weld periphery region at which the temperature plot was calculated. The red dashed region represents the extrapolated temperature profiles for hold times of 5 ms, 55 ms and 105 ms that were not calculated by SORPAS due to modelling limitations. The justification for this extrapolation is presented in Section 7.3.3. As observed in the electrode and weld shoulder regions, the temperature profiles for all hold times overlap perfectly from the start of the welding cycle up to the onset of the hold time phase. In this region, the temperature increases from room temperature to approximately 1030 °C by the start of the hold time phase. This temperature is reached during the weld time stage of the RSW process, and is the highest temperature in the weld periphery region throughout the entire welding cycle. Following the electrode lift-off at the end of the hold time, the temperature increases again; however, the magnitude of this temperature rise is lower than the peak temperature during the weld stage. Consistent with the trends observed in the other weld regions, the peak temperature reached after the hold time is higher for shorter hold times and decreases systematically with increasing hold time. The overall shape of the temperature vs. time profiles remains similar across all hold times.

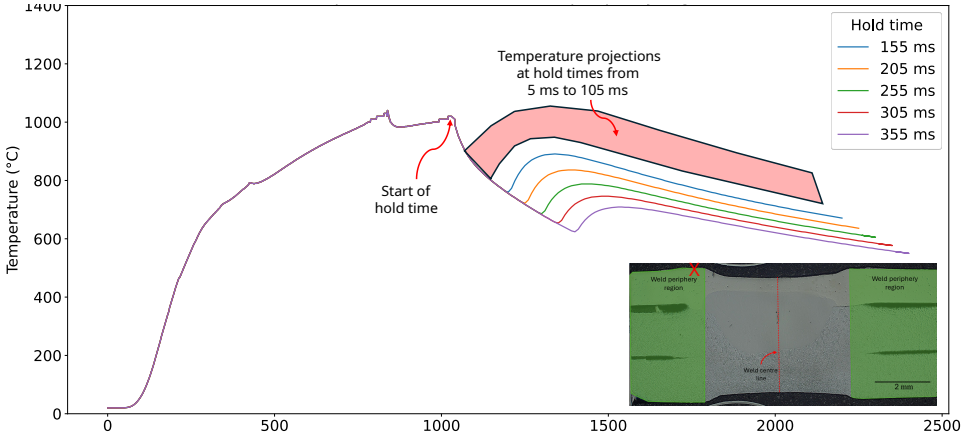


Figure 7.15: Temperature versus time plot in the weld periphery region for different hold times, where the red 'X' marks the location of the plot

7.4. Discussion

The results show that LME crack formation during RSW varies across different regions of the weld cross-section. This is reflected in both the experimentally obtained RSW cross-sections and the FEA results, which indicate distinct temperature vs. time profiles in the electrode region, weld shoulder region, and weld periphery region of the TWIP sheet. These differences in thermal history influence the availability of liquid Zn at the Fe-Zn interface, the stage of the RSW process at which LME cracks initiate, and the depth of the LME cracks. In particular, variations in peak temperature, cooling behaviour, and the effect of the water-cooled electrodes determine how Zn diffuses into the steel. The following subsections discuss each weld region and the effect of hold time on LME behaviour.

7.4.1. Electrode region

A relatively large number of LME cracks were observed at lower hold times (5 ms, 55 ms and 105 ms) compared to other regions of the weld. With increasing hold time, the average number of cracks in this region decreases progressively, and no LME cracks are observed at hold times of 205 ms and higher. This result is also corroborated by Choi et al, who observed a decreasing number of cracks in this region with increasing hold time [7]. During the RSW process, the Zn coating melts and this liquid Zn is displaced to the sides of the electrode due to the applied electrode force [2]. At shorter hold times (5 ms to 105 ms), the duration of electrode contact is insufficient for the water-cooled electrodes to fully solidify the molten Zn in the electrode-pressed region. As a result, liquid Zn can flow back from the sides of the weld into the electrode region after electrode lift-off [9]. This increases the availability of liquid Zn at the steel surface during the cooling stage, promoting LME crack initiation. With increasing hold time, longer electrode contact enhances heat extraction and accelerates Zn solidification,

thereby reducing the amount of liquid Zn available to penetrate grain boundaries and resulting in fewer LME cracks [7]. At hold times of 205 ms and above, the lack of observable LME cracks in this region suggests that the liquid Zn accumulated in the sides of the electrode fully solidifies, and thus there is insufficient Zn available to form LME cracks in this region. The flow of heat from the nugget towards the electrode interface is more pronounced for shorter hold times as less heat is removed by the electrode.

7.4.2. Weld shoulder region

FEA results from Figure 7.14 show that for all investigated hold times, the weld shoulder region experiences a rapid temperature increase during the early stages of welding between 300-500 ms, followed by a sharp decrease to approximately 430 °C and a subsequent temperature rise prior to the start of the hold time phase. Ashiri et al. attributed this thermal behaviour to non-uniform electrode contact in the shoulder region during the initial stages of RSW, which leads to localized current concentration and elevated temperature and stresses [10]. Jung et al. and Bhattacharya et al. proposed that LME crack formation occurs during the cooling stage of the welding cycle, when tensile stresses can exceed the yield strength of the steel. As the weld cools and contracts under mechanical constraints, the release of heat during cooling promotes the development of stresses, increasing the likelihood of observing LME [3, 11]. Based on the combined experimental observations and FEA results of the present study, LME cracks in the weld shoulder region are proposed to initiate during the cooling phase between approximately 300 and 500 ms from the start of the welding cycle. Since the temperature vs. time profiles in this region are identical for all conditions up to the start of the hold time period, the thermomechanical conditions for crack initiation are not changed when the hold time is increased. The observed decrease in the number of cracks with increasing hold time is therefore attributed primarily to differences in crack propagation during and after the hold time. Longer hold times increase heat removal by the water-cooled electrodes, lowering the temperature after the end of the hold time and reducing the amount of liquid Zn available for further crack growth. The increase in average crack depth from 5 ms to 205 ms suggests that, although fewer cracks are present at longer hold times, these cracks are exposed to sufficiently high temperatures after electrode lift-off (approximately 700 °C to 900 °C) to propagate further into the material. At hold times beyond 205 ms, the peak temperature reached after electrode lift-off decreases, and interaction with the weld fusion zone further constrains crack growth. As a result, the average crack depth in the weld shoulder region decreases at higher hold times.

7.4.3. Weld periphery region

The weld periphery region is not in direct contact with the RSW electrode and therefore experiences a thermal profile that is less influenced by electrode cooling compared to the electrode or weld shoulder region. FEA results in Figure 7.15 indicate that this region reaches the ductility trough temperature for TWIP steel (700 □) at approximately 500 ms for all investigated hold times [3]. In addition, Zn displaced from the electrode region

is likely to accumulate toward the weld periphery, which may result in a comparable availability of liquid Zn across the different hold times. These factors explain the absence of a clear dependence of the number of LME cracks on hold time in this region. As shown in Figure 7.11, the average crack depth in the weld periphery region is higher at hold times between 155 ms and 305 ms compared to shorter hold times. One possible explanation is that at higher hold times, the overall number of LME cracks across the weld cross-section is reduced. Thus, the available thermal energy and driving force for crack propagation may be concentrated on a smaller number of cracks, allowing those present in the periphery region to propagate more deeply. However, trends observed in the weld periphery region must be interpreted with caution. On average, only one to two LME cracks are observed per sample in this region, which limits the confidence with which any trends can be interpreted. The low number of cracks makes it difficult to draw definitive conclusions regarding the influence of hold time on crack depth or propagation behaviour in this region.

7.5. Conclusions

This study investigated the effect of RSW hold time on LME in TWIP steel using a combination of cross-section microscopy of experimental RSW tests and finite element simulations. Hold time was varied from 5 ms to 355 ms to capture the evolution of LME cracks. The following conclusions can be drawn:

- LME crack formation was found to be strongly dependent on weld location. The electrode region showed the highest number of cracks at short hold times, with many shallow cracks observed from 5 ms to 105 ms. As hold time increased, the number of cracks in this region decreased steadily, and no LME cracks were observed for hold times of 205 ms and above.
- In the weld shoulder region, cracks were observed over a broader range of hold times. Although crack initiation conditions were similar for all hold times, the number of cracks decreased and crack depth increased up to intermediate hold times (155 ms and 205 ms), before decreasing at longer hold times (255 ms to 355 ms). This indicates that hold time primarily affects crack propagation rather than initiation, through its influence on temperature after electrode lift-off and interaction with the weld fusion zone.
- The weld periphery region showed fewer cracks overall, with no clear dependence of LME on hold time. Crack depths in this region were generally higher at intermediate hold times (155 ms), although the low number of cracks limits robust conclusions. The lack of direct electrode contact and the accumulation of Zn in this region likely reduce the sensitivity of LME behaviour to hold time compared to regions closer to the electrode.
- FEA simulations showed that temperature evolution is identical across all hold times until the start of the hold period, after which the temperature profiles diverge. Shorter hold times resulted in higher temperatures after electrode lift-off across all regions, while longer hold times led to lower peak temperatures following

electrode lift-off. For hold times of 155 ms and above, the simulations showed good agreement with experimental weld nugget geometry, supporting their use in interpreting LME behaviour.

Overall, this work demonstrates that RSW hold time plays a critical role in controlling both the severity and location of LME cracks in TWIP steel. Increasing hold time reduces crack density near the electrode and alters crack growth behaviour in other regions of the weld. These findings show that hold time can be used as an effective parameter to mitigate LME.

References

[1] D. Bhattacharya, L. Cho, E. van der Aa, A. Pichler, N. Pottore, H. Ghassemi-Armaki, K. O. Findley and J. G. Speer. 'Influence of the starting microstructure of an advanced high strength steel on the characteristics of Zn-Assisted liquid metal embrittlement'. In: *Materials Science and Engineering: A* 804 (15th Feb. 2021), p. 140391. ISSN: 0921-5093. DOI: 10.1016/j.msea.2020.140391.

[2] H. Zhang and J. Senkara. *Resistance Welding: Fundamentals and Applications*. Boca Raton: CRC Press, 20th Dec. 2005. 444 pp. ISBN: 978-0-429-10159-5. DOI: 10.1201/b12507.

[3] D. Bhattacharya. 'Liquid metal embrittlement during resistance spot welding of Zn-coated high-strength steels'. In: *Materials Science and Technology* 34.15 (13th Oct. 2018). _eprint: https://doi.org/10.1080/02670836.2018.1461595, pp. 1809–1829. ISSN: 0267-0836. DOI: 10.1080/02670836.2018.1461595.

[4] F. Okigami, N. Avedissian, H. Ghassemi-Armaki, X. Gao and W. Zhang. 'Numerical modeling of liquid metal embrittlement initiation during resistance spot welding of third generation advanced high strength steel – Effect of welding schedule and electrode alignment'. In: *Journal of Manufacturing Processes* 110 (31st Jan. 2024), pp. 173–191. ISSN: 1526-6125. DOI: 10.1016/j.jmapro.2023.12.065.

[5] Y. G. Kim, I. J. Kim, J. S. Kim, Y. I. Chung and D. Y. Choi. 'Evaluation of Surface Crack in Resistance Spot Welds of Zn-Coated Steel'. In: *MATERIALS TRANSACTIONS* 55.1 (2014), pp. 171–175. DOI: 10.2320/matertrans.M2013244.

[6] C. DiGiovanni, X. Han, A. Powell, E. Biro and N. Y. Zhou. 'Experimental and Numerical Analysis of Liquid Metal Embrittlement Crack Location'. In: *Journal of Materials Engineering and Performance* 28.4 (1st Apr. 2019), pp. 2045–2052. ISSN: 1544-1024. DOI: 10.1007/s11665-019-04005-2.

[7] D. Choi, S. Uhm, C. M. Enloe, H. Lee and G. Kim. 'Liquid Metal Embrittlement of Resistance Spot Welded 1180TRIP Steel - Effects of Crack Geometry on Weld Mechanical Performance'. In: 1st Jan. 2017, pp. 454–462. DOI: 10.7449/2017/mst_2017_454_462.

[8] C. Böhne, G. Meschut, M. Biegler and M. Rethmeier. ‘Avoidance of liquid metal embrittlement during resistance spot welding by heat input dependent hold time adaption’. In: *Science and Technology of Welding and Joining* 25.7 (1st Oct. 2020), pp. 617–624. ISSN: 1362-1718. DOI: 10.1080/13621718.2020.1795585.

[9] D. Sigler, J. Schroth and W. Yang. ‘Observations of liquid metal-assisted cracking in resistance spot welds of zinc-coated advanced high-strength steels’. In: *Sheet metal welding conference XIII. Proceedings*. Sheet metal welding conference XIII. Livonia, MI, USA, 14th May 2008.

[10] R. Ashiri, M. Shamanian, H. R. Salimijazi, M. A. Haque, J.-H. Bae, C.-W. Ji, K.-G. Chin and Y.-D. Park. ‘Liquid metal embrittlement-free welds of Zn-coated twinning induced plasticity steels’. In: *Scripta Materialia* 114 (15th Mar. 2016), pp. 41–47. ISSN: 1359-6462. DOI: 10.1016/j.scriptamat.2015.11.027.

[11] G. Jung, I. S. Woo, D. W. Suh and S.-J. Kim. ‘Liquid Zn assisted embrittlement of advanced high strength steels with different microstructures’. In: *Metals and Materials International* 22.2 (1st Mar. 2016), pp. 187–195. ISSN: 2005-4149. DOI: 10.1007/s12540-016-5579-7.

8

General discussion, limitations and recommendations

8.1. General discussion

Resistance spot welding is a complex thermo-mechanical process in which temperature, stress, and microstructure evolve simultaneously and non uniformly across the weld, and in which several distinct factors must coincide for liquid metal embrittlement to occur. During RSW of galvanised TWIP steel, the combined action of Joule heating and electrode force melts the Zn coating and generates temperature gradients and residual stresses across the weld, creating the conditions under which LME becomes possible. Whether cracking actually initiates and how far it propagates depends on a sequence of interdependent factors, each of which was discussed in the preceding chapters of this thesis. At the Fe-Zn interface, the formation and subsequent breakdown of intermetallic (IM) phases governs whether liquid Zn is available to diffuse into the steel. Continuous IM layers act as a barrier to Zn penetration, and once they break down, liquid Zn penetrates the austenitic grain boundaries and initiate cracking (Chapter 4). Once initiated, the path the crack follows is governed by the character of the grain boundary network, influenced by GB misorientation and the orientation of the boundary with respect to the loading axis shifting as the weld heat input increases (Chapter 5). The rate at which the crack propagates is controlled by stress-assisted diffusion of Zn ahead of the crack tip, which increases with weld time and is faster along grain boundaries than through the bulk (Chapter 6). Finally, the availability of liquid Zn itself can be modified after welding through the hold time, which determines whether displaced Zn solidifies before it can fuel further cracking, with distinct effects across the electrode, shoulder, and periphery regions of the weld (Chapter 7).

8.1.1. Evolution of LME in RSW

The four studies collectively show that LME during RSW of electrogalvanised TWIP steel is governed by local temperature and stress during the RSW cycle. This sequence, reconstructed from Chapters 4 is outlined below. At WT ≤ 300 ms, the weld shoulder

temperature remains below 419 °C and the Zn coating remains intact. No Fe-Zn IM phases form and no LME is observed. The interface consists only of the Al-rich inhibiting layer formed during galvanising. Between 300 ms and 500 ms, shoulder temperatures reach approximately 470-650 °C. In this range, continuous IM layers form, including δ, Γ/Γ_1, and α-Fe(Zn). The α-Fe(Zn) phase observed at WT = 500 ms is enriched in Al (5.91 wt.%) and depleted in Mn (2.11 wt.%) relative to the bulk, consistent with Al stabilising ferrite and Mn stabilising austenite. Disruption of the Al-oxide inhibiting layer provides a local Al source that promotes α-Fe(Zn) formation. No LME occurs at this stage, as the continuous IM layer prevents direct liquid Zn-GB contact. At WT = 700 ms, shoulder temperatures exceed the Zn boiling point, while the weld periphery reaches 771 °C. The IM layer becomes discontinuous and begins to break down. LME cracks first appear at the weld shoulder, with an average depth of 21 µm and width of 2 µm. Once cracking begins, liquid Zn can escape from the shoulder region, preventing re-formation of a stable IM layer. For WT ≥ 900 ms, all shoulder locations exceed 800 °C, above the stability range of all Fe-Zn IM phases. EBSD confirms the absence of IM phases across all higher WTs (900-1700 ms). LME severity increases with WT: average crack depth increases from 32 µm (900 ms) to 490 µm (1700 ms), and crack width increases from 4 µm to 57 µm. This trend reflects increasing peak temperatures, longer exposure to liquid Zn, and faster Zn GB diffusion kinetics at higher temperatures.

The grain boundary (GB) crack path data from Chapter 5 provide further support for this diffusion-controlled interpretation. The Klinger-Rabkin model predicts that GB diffusion flux depends on both GB diffusivity (D_{GB} and the normal stress component acting on the boundary. D_{GB} increases with GB energy, which in HAGBs is related to excess free volume and misorientation. At WT = 700 ms, FEA predicts peak shoulder temperatures of 771 °C - 930 °C. Under these conditions, differences in diffusivity between high (45-55°) and moderate-misorientation (25-35°) HAGBs are still significant. As a result, 73% of triple junctions show cracks following the higher-misorientation GB, even when it is less favourably aligned with the loading axis. In comparison, only 58% favoured the GB with the higher stress normalisation factor, showing that stress alignment is not yet the dominant factor. At WT = 1700 ms, FEA predicts shoulder temperatures around 980 °C and above. Here, Zn diffusion increases for all GB types, and the difference between HAGBs becomes small. Both competing GBs therefore allow Zn penetration, and diffusivity is no longer the controlling factor. This is reflected in the crack path data: the preference for higher-misorientation GBs drops from 73% to 56%, while the preference for higher stress alignment increases from 58% to 91%. When only random HAGBs are considered, removing CSL effects, the preference for higher stress alignment rises from 63% at 700 ms to 86% at higher WT. This shows that at high WT, crack paths are mainly controlled by the stress term in the Klinger-Rabkin model rather than GB diffusivity. Σ3 coherent twin boundaries were LME-free at all weld times, despite making up 30-33% of all GBs and occurring at stress normalisation factors up to 0.8-1.0. This indicates that the wetting condition is never satisfied for Σ3 GBs under the RSW conditions studied. In contrast, non-Σ3 CSL GBs were mostly LME-free at 700 ms but increasingly appeared in the crack path at higher weld times. However, they were only selected when their stress normalisation factor exceeded that of the competing GB at the same triple junction. This shows that CSL character alone is

not sufficient for crack resistance: GBs can be embrittled if the local stress driving force is less favourable in the competing boundary.

The Zn diffusion results from Chapter 5 further support this interpretation by quantifying the extent of Zn transport ahead of LME crack tips. EDS line scans show that the bulk Zn diffusion distance increases with WT in both directions: in ND from 0.55 ± 0.01 µm at 700 ms to 3.09 ± 0.11 µm at 1700 ms, and in RD from 0.42 ± 0.02 µm to 2.51 ± 0.14 µm over the same range. In all cases, the ND diffusion distance is higher than the RD distance, with an average ratio of 1.29 ± 0.09, which is captured by the FEA diffusion model (1.42 ± 0.08). This anisotropy is consistent with the triangular crack geometry in ND, which effectively increases the diffusion path length in that direction. Using the Fisher-Klinger-Rabkin framework and literature values for Zn diffusion, the corresponding GB diffusion distance is estimated to be 30 times higher than the measured bulk diffusion distance at all WTs.

The hold time study shows a second, distinct control parameter for LME that acts after crack initiation. FEA confirms that the temperature history is identical across HT = 5-355 ms up to the start of the holding stage; differences only arise after electrode lift-off. HT therefore does not influence crack initiation during the weld stage, which is governed by WT, but instead controls cooling, and thus the availability of liquid Zn and the thermal driving force for crack growth. This effect is most pronounced in the electrode region where crack density drops from 13.5 cracks per cross-section at 5 ms to zero at ≥205 ms. This is because longer HT allows displaced liquid Zn to solidify under electrode pressure before lift-off, preventing crack formation once tensile stresses develop. At the weld shoulder, crack depth increases from 80 µm at 5 ms to a maximum of 334 µm at 155 ms, where fewer cracks form but post-lift-off temperatures remain >700 °C. With further increases in HT, increased cooling during reduces both Zn diffusivity and available liquid Zn. In contrast, the weld periphery shows no HT dependence, as it is not in direct contact with the electrodes and reaches its peak temperature (1030 °C) during the weld stage regardless of HT.

8.2. Limitations

All experimental results in this thesis were obtained from a single material system: a 1.23 mm electrogalvanised TWIP steel, welded in a triple-stack configuration with DX54 backing sheets. The triple-stack geometry increases heat input and promotes LME relative to the two-sheet configuration used in automotive production. Quantitative results like crack dimensions, diffusion distances, hold time thresholds should not be transferred directly to two-sheet welds or to TWIP steels of different composition without validation.

EDS line scans measure Zn diffusion in the grain bulk and cannot resolve Zn along individual GBs. As a result, the GB diffusion distance (30× the bulk diffusion distance, Chapter 5) is obtained indirectly by combining measured bulk diffusion data with the Fisher-Klinger-Rabkin framework and GB diffusion constants for Zn from literature. This estimate is subject to two main uncertainties. First, the diffusion constants are derived for a binary Fe-Zn system, whereas the TWIP steel used here contains 17.3 wt.% Mn and 1.49 wt.% Al, both of which are expected to modify GB structure and diffusivity, but

by an amount that is not quantified for this composition. Second, the applied stress factor of 2.5 is taken from literature for a different RSW stress configuration, introducing additional geometric uncertainty. For these reasons, the 30× factor between GB and bulk diffusion should be interpreted as an order-of-magnitude estimate.

The 2D FEA diffusion model in Chapter 5 assumes a constant Zn concentration at the crack interface, fixed crack geometry, and equilibrium thermodynamic parameters from ThermoCalc and DICTRA. These assumptions introduce three main sources of systematic error. First, the infinite reservoir assumption neglects depletion of liquid Zn as it is consumed by diffusion, leading to an overestimation of diffusion distances. Second, fixed crack dimensions ignore the coupling between crack growth and the evolving geometry of the Zn source. Third, equilibrium diffusivity values do not capture non-equilibrium segregation of Mn and Al at GBs during the rapid RSW thermal cycle, which can alter local diffusion behaviour. Together, these effects explain why the model overpredicts absolute diffusion distances compared to EDS measurements.

The stress normalisation factor used in Chapter 4 is based on the macroscopic stress field at the weld shoulder from FEA. It does not capture local stress concentrations at triple junctions, elastic-plastic anisotropy between neighbouring grains with different crystallographic orientations, or the evolution of stress during the RSW cycle. In this work, it is used as a relative metric to compare two competing GBs at the same triple junction, where both experience the same macroscopic stress field. For this purpose, the approximation is considered valid. However, it cannot be interpreted as an absolute stress value for an individual GB, and its predictive capability at the single-triple-junction scale is therefore limited.

8.3. Future work and recommendations

The following recommendations are derived from specific limitations and open questions identified in this thesis.

- Direct measurement of Zn concentration along individual GBs ahead of LME crack tips using Atom Probe Tomography (APT) is recommended to validate the GB-to-bulk diffusion ratio (30) derived in Chapter 5. The current estimate is based on GB diffusion constants for Zn obtained for a binary Fe-Zn system. This would enable direct measurement of GB diffusion profiles under RSW conditions
- The LME GB susceptibility index proposed in Chapter 4 combines GB energy, temperature-dependent Zn diffusivity, and a stress normalisation factor, but remains qualitative because GB energy for the TWIP steel HAZ microstructure has not been experimentally determined. To address this, five-parameter GB characterisation is recommended using EBSD combined with stereological reconstruction to resolve GB plane orientation. This should be performed on a statistically representative dataset of LME and LME-free GBs, and would enable quantitative evaluation of the susceptibility index and allow direct prediction of crack path selection at individual triple junctions.
- Chapter 4 shows that Σ3 twin boundaries are resistant to Zn-induced LME under all RSW conditions studied, and that non-twin CSL boundaries provide partial

resistance at lower WT. This suggests that grain boundary engineering (GBE) could be a potential route to improve LME resistance by increasing the fraction of structurally resistant GBs and disrupting the connectivity of susceptible HAGB networks. However, while GBE has been proposed as a mitigation strategy, its effectiveness in the context of LME during RSW is not yet understood in sufficient detail. Further work is therefore required to establish how GBE can be used to increase the fraction of LME-resistant GBs and reduce overall LME susceptibility under industrial welding conditions.

- The hold time results identify a critical role for post-weld thermal conditions in suppressing LME. However, the observed behaviour is specific to a limited set of welding conditions and is expected to depend on overall heat input. A more complete understanding would require mapping HT effects across a wider range of welding conditions to establish a process window for LME suppression. This should be supported by modelling of Zn solidification and thermal evolution to provide a predictive framework linking HT, heat input, and LME susceptibility

- The phase identification carried out in this work relied on EBSD indexing based on the Hough transform [1], supported by EDS, STEM-EDS, and XRD to resolve Fe-Zn intermetallic phases that share similar crystal structures. A promising direction for future work is the application of Spherical Indexing (SI) EBSD to more accurately determine the crystallographic structure of these intermetallic phases [2]. Compared to traditional Hough indexing, SI offers a significantly improved indexing rate and angular precision, which would allow phases such as δ, Γ, Γ_1, and α-Fe(Zn) to be distinguished more reliably, particularly where their crystal structures or orientations are closely related.

  The results of this thesis provide the basis for a multi-scale model of LME during RSW, combining temperature and stress fields from FEA, experimentally characterized Zn diffusion behaviour, and a crack path selection framework that accounts for both GB character and stress alignment. In principle, these elements can be integrated into a coupled modelling framework in which FEA provides the thermal and mechanical boundary conditions, a diffusion model predicts Zn transport at the microstructural scale, and EBSD-derived GB information is used to evaluate local susceptibility and crack path selection at individual triple junctions. Such a model would enable spatially resolved prediction of both LME initiation and propagation during RSW.

References

[1] D. N. Leonard, G. W. Chandler and S. Seraphin. 'Scanning Electron Microscopy'. en. In: *Characterization of Materials*. _eprint: https://onlinelibrary.wiley.com/doi/pdf/10.1002/0471266965.com081.pub2. John Wiley & Sons, Ltd, 2012, pp. 1–16. ISBN: 978-0-471-26696-9. DOI: 10.1002/0471266965.com081.pub2. URL: https://onlinelibrary.wiley.com/doi/abs/10.1002/0471266965.com081.pub2.

[2] W. C. Lenthe, S. Singh and M. D. Graef. 'A spherical harmonic transform approach to the indexing of electron back-scattered diffraction patterns'. In: *Ultramicroscopy* 207 (Dec. 2019), p. 112841. ISSN: 0304-3991. DOI: 10.1016/j.ultramic.2019.112841. URL: https://www.sciencedirect.com/science/article/pii/S0304399119301585.

Acknowledgements

My academic journey has been exciting and enriching, and I can say with confidence that it would not have been possible without the help, support, guidance, and advice of many people who have had my best interests at heart. I am deeply grateful for the opportunity to acknowledge everyone who has played a part in it.

I would like to thank my promoter and daily supervisor Marcel Hermans. You have a very relaxed and approachable supervision style, which made it easy and enjoyable to work with you. I'm glad I had the opportunity to learn from you, and I am very proud to be your final PhD candidate. I would also like to thank Leo Kestens for being an invaluable mentor and co-promoter. I have barely scratched the surface of the vastness of your expertise, and I feel lucky to have been your student from my MSc days. I would like to thank Vera Popovich for her support, guidance and feedback throughout my project. I would also like to acknowledge the Joining and Additive Manufacturing research group, who have been a very important part of my PhD journey. I'd like to thank all the technicians, MSc and PhD researchers who have been a part of the group for your critical feedback - it has immeasurably improved the quality of my research. I have also had the privilege of learning from you and your work over the last few years.

I'd like to thank the MUSCLES consortium for a wonderful collaboration. I'd like to thank Florian and Francesco in Groningen and Lotte from NWO. I'd like to thank the Welding and Joining Knowledge group at Tata Steel in IJmuiden for providing the facilities for performing welding tests. I'd like to thank He Gao for the modelling expertise, and I'd like to thank Soheil for the timely feedback and fruitful collaboration.

I would like to acknowledge all the lab technicians at MSE I've had the privilege of working with and learning from – Ton, Elise, Raymond, Durga, Jurriaan, Hans, Sean, Ruud and Richard. I'd especially like to thank Kees for his input and expertise, which underpinned a big part of my characterization work. I'd also like to thank Remko for all the help and collaboration.

I want to thank the FNV union for their continuous effort to secure fair working conditions and work-life balance for university employees. Their work allowed me and my colleagues to enjoy a life relatively free of stress while pursuing a PhD - something that is easy to overlook but far from universal in academia.

I'd like to thank my MSc friends Ide, Jesper, Jelmer, Rohan, Kelsey, Stratos, Luis and Ines for the wonderful times we have shared together. You were my first friends in the Netherlands and made me feel home in a new country. I'd like to specially thank Can for the encouragement before I started this PhD.

I'd like to thank my PhD colleagues and the lunch table for the laughs and discussions. You all have shown me the importance of a supportive community and the value of having a little whimsy in our stressful days. Academia can be a lonely place without a support group bonded by shared experiences. Thank you Soroush, Vitoria, Arash,

Aravind, Eszter, Luis, Daniel, Yeli, Aswin, Harsh, Arjun, Chryssa, Ana, Khatareh, Jasper, Alessandra, Mohammed, Hannah, Jithin, Luis, Naveen, Gowtham, Maria, Joep, Jose, Aravind, Camilla, Radhey, Jungwan, Joost, Amin, Timo, Robbert, Gyumin, Teresa, Tobia, Jose, Adnan, Ishank, Iftikhar, Milou, Marco and everyone else I had the privilege of knowing. I'd like to thank Virginia for being a valuable mentor to me. Observing you and your attention to detail has taught me to be a better researcher. I'd like to thank Tim for always giving me time to stress-test my ideas. I'd like to thank Amir for always indulging my unserious curiosities. I'd like to thank Elsa for conceptualizing the cake schedule. I'd like to thank Alice for the invaluable discussions and for representing PhDs with empathy. I'd like to thank the CoffeeStar gang for the A-tier memories despite the B-tier coffee. I'd like to thank my paranymphs Julia and Fabian for the wonderful memories and conversations. My life is a lot richer with your love and friendship. I'd like to thank Philipp – for the countless hours of conversation in our neighbouring offices and labs. The worst days are brighter after a conversation with you.

I would like to acknowledge some incredible teachers I have had the privilege of learning from. I'd like to thank my high school chemistry teacher Ms. Malini for making difficult ideas easy to process. I'd like to thank Dr KS Balaji and Dr Balaji Sampath for teaching me to ask the right questions. I'd like to thank Dr Raman for his guidance and support.

I'd like to thank my parents for everything they have done for me. They have gone through many struggles and made many sacrifices to give me the best chance to succeed in life. Their emphasis on giving me a good education is a big reason I am here today, and for that I am truly grateful.

I'd like to thank my brother Barath for kindling the fire of my early curiosity. Lengthy conversations with you throughout our childhood were foundational to my understanding of the world and my interest in pursuing science.

I'd like to thank my cat Chutney for being a constant companion through my most stressful times. You have shown me the true meaning of unconditional love, and your presence has made this journey a little easier to go through.

I'd finally like to thank my partner Archana. For supporting me, for proofreading my drafts and presentations, for listening to me incessantly complain about journal reviews and train delays, but most importantly for giving me your unwavering love and support every single day. Building our life together has been my greatest privilege. I do not take this for granted and I hope I made you proud.

Curriculum Vitæ

Gautham Mahadevan

05-05-1996 Born in Chennai, India.

Education

2014–2018 B.Tech in Metallurgical and Materials Engineering
National Institute of Technology, Trichy, India

2018–2020 M.Sc in Materials Science and Engineering
Delft University of Technology

2018–2020 PhD in Materials Science and Engineering
Delft University of Technology
Thesis: Liquid Metal Embrittlement of Automotive Steels
Promotors: dr. ir. M.J.M Hermans and Prof. dr. ir. L.A.I. Kestens

Professional experience

2020–2022 R&D Engineer at RAMLAB, Rotterdam

List of Publications

1. **Mahadevan, G.**, Bertolo, V., Sabooni, S. et al. Characterizing the influence of weld time on the Fe-Zn interface during liquid metal embrittlement of resistance spot welded TWIP steel, Materials Science and Engineering: A 972 (2026)

2. **Mahadevan, G.**, Bertolo, V., Sabooni, S. et al. Characterizing the effect of GB misorientation on liquid metal embrittlement crack path of resistance spot welded TWIP steel, Materialia 48 (2026)

3. **Mahadevan, G.**, Bertolo, V., Sabooni, S. et al. Characterizing zinc diffusion during liquid metal embrittlement of resistance spot welded TWIP steel. Weld World 70, 3043–3056 (2026)

4. Bertolo, V., **Mahadevan, G.**, Petrov, R, Popovich, V. et al. The role of microstructure in crack growth during liquid metal embrittlement of Zn-galvanised TWIP steel, Journal of Materials Research and Technology 38 (2025)

5. Bertolo, V., **Mahadevan, G.**, Petrov, R, Popovich, V. et al. Decoupling early-stage cracking and propagation mechanisms in liquid metal embrittlement of Zn-galvanised TWIP steel, Journal of Materials Research and Technology 38 (2025)

6. Romano, T., **Mahadevan, G.**, Petrov, R, Popovich, V. et al. Microstructural, mechanical, and thermal characterization of constitutive layers in copper-steel functionally graded material manufactured via laser directed energy deposition, Materials and Design 256 (2025)